UNIVERSITÀ DEGLI STUDI DI MILANO BICOCCA

SCUOLA DI DOTTORATO

UNIVERSITÀ DEGLI STUDI DI MILANO-BICOCCA

Department of Material Science

PhD program Material Science and Nanotechnology Cycle XXXIII

Droplet Epitaxy Quantum Dots on GaAs(111)A Substrates for Quantum Information Applications

Surname: Tuktamyshev Name: Artur

Registration number: 835462

Tutor: prof. Stefano Sanguinetti

Coordinator: prof. Marco Bernasconi

ACADEMIC YEAR 2017 – 2020

Abstract

The unique properties of the self-assembled quantum dots, such as the discrete energy levels and a precise control of additional features, like an entangled photon emission, by the dot shape and size, have a great potential in the optoelectronic device fabrication for quantum network applications. For this reason, one of the main challenges in the self-assembled quantum dot fabrication is the reproducibility of the dots in terms of shape and size. Droplet epitaxy is well-established for the fabrication of III-V compound semiconductor nanostructures and allows to control the quantum dot density and size in a wide range. The size distribution of the self-assembled droplet epitaxial dots is strictly determined by the original size distribution of the droplets. Droplet epitaxy allows to fabricate the quantum dots on (111) surfaces, thus exploiting a C_{3v} symmetry of the surface, to obtain highly symmetric dots, which is desirable for a generation of entangled photon pairs.

The thesis is devoted to the fabrication of GaAs and InAs quantum dots on GaAs (111)A-oriented substrates, in particular on the vicinal one. The use of the vicinal substrates is caused by the possibility to grow thick layers of Bragg reflectors, which are necessary to increase an extraction efficiency from the quantum dots. Firstly, we carried out the study of the fabrication of GaAs dots on exact GaAs(111)A substates. The conditions to fabricate highly symmetric dots are shown. It was demonstrated that these dots have fine structure splitting as low as 4.5 μeV. Then, an extensive fundamental study on the nucleation of Ga and In droplets on miscut substrates, highlighting the role of the Ehrlich-Schwöbel barriers at the step edges controlling the adatom diffusion and the strain relaxation was performed. The interest to InAs dots is motivated by the possibility to fabricate telecom band quantum emitters for long-distance quantum communications. We found conditions to grow InAs quantum dots on vicinal GaAs(111)A substates emitting at telecom wavelengths using a very flat and smooth InAlAs metamorphic layer. The metamorphic layer is necessary to reduce the strain between dots and a barrier layer and to shift an emission to telecom range. The photoluminescence characterization of the dots shows the fine structures splitting as low as 16±6 μeV at telecom O-band. Finally, these InAs quantum dots were embedded in a cavity, using GaAs/AlGaAs distributed Bragg reflectors, which boosted the brightness of these emitters.

Keywords: droplet epitaxy, quantum dots, GaAs(111)A, vicinal surface, telecommunication range, fine structure splitting, entangled-photon emission

Contents

Introduction ... 1

Part I. Background ... 3

Chapter 1. QD as an ideal source for polarization entangled photon pair generation ... 3

- **1.1. QDs with the low FSS** ... 7
- **1.2. Energy and FSS tunable sources of entangled photons** ... 10
- **1.3. QD as a single photon emitter** ... 15
- **1.4. Increasing the brightness** ... 19

Chapter 2. Molecular Beam Epitaxy ... 23

- **2.1. Historical excursion into the MBE technology** ... 23
- **2.2. Atomic processes in crystal growth** ... 25
- **2.3. Thin film growth modes** ... 27
- **2.4. Reflection High Energy Electron Diffraction** ... 29

Chapter 3. Droplet epitaxy ... 35

- **3.1. Droplet deposition process** ... 35
- **3.2. Droplet density dependence on a deposition temperature and a flux rate** ... 37
- **3.3. Classical nucleation theory** ... 37
- **3.4. Capture zone approach** ... 40
- **3.5. The surface reconstruction influence** ... 42
- **3.6. Crystallization process** ... 44
- **3.7. Local droplet etching technique** ... 49

Chapter 4. Experimental setup ... 51

- **4.1. MBE system** ... 51
- **4.2. Morphological characterization** ... 54
- **4.3. Photoluminescence setup** ... 57

Part II. Results ... 59

Chapter 5. Droplet epitaxy on singular GaAs(111)A ... 59

- **5.1. Ga droplet nucleation** ... 59
  - *Buffer layer growth* ... 59
  - *Droplet density dependence on the deposition temperature* ... 60
  - *Capture zone distribution* ... 63
  - *Diffusion of Ga adatoms* ... 65
  - *QD size distribution* ... 66
- **5.2. QD shape control** ... 68
- **5.3. High-temperature symmetrical QDs** ... 71
- **Conclusions** ... 75

Chapter 6. Droplet epitaxy on vicinal GaAs(111)A 76

6.1. GaAs QDs on vicinal GaAs(111)A 76

Buffer layer growth 76

Ga droplet nucleation 77

Influence of miscut substrate on diffusion behavior 82

Capture zone distribution 84

6.2. In droplets on vicinal GaAs(111)A 85

The temperature dependence of In island density 85

RHEED analysis of In solid island formation 88

Strain-induced reentrant behavior of In island density dependence 90

Conclusions 93

Chapter 7. Telecom InAs QDs on GaAs(111)A vicinal substrates 94

7.1. Metamorphic growth of InAlAs buffer layer 94

Quantum mechanical calculation of InAs/InAlAs(111)A QDs 97

Smoothing the barrier layer surface 98

Threading dislocation density 99

7.2. μ-PL characterization of single InAs QDs 103

FSS measurements 105

7.3. Increasing the brightness 106

DBR fabrication on vicinal GaAs(111)A 107

InAs QDs embedded in the cavity 110

PL characterization 111

Atomistic Pseudopotential Theory calculation 114

Conclusions and Outlook 117

Bibliography 119

List of publications 129

Acknowledgements 130

List of acronyms

2D	two-dimensional
3D	three-dimensional
AFM	atomic force microscopy
BCT	body-centered tetragonal
BEP	beam equivalent pressure
BS	beam splitter
CZ	capture zone
CZD	capture zone distribution
DBR	distributed Bragg reflector
DE	droplet epitaxy
EPD	etch pit density
ES	Ehrlich-Schwöbel
FCC	face-centered cubic
FCT	face-centered tetragonal
FSS	fine structure splitting
FWHM	full width at half maximum
GWD	generalized Wigner distribution
HWP	half-wave plate
LDE	local droplet etching
MBE	molecular beam epitaxy
MEE	migration enhanced epitaxy
ML	monolayer
MMBL	metamorphic buffer layer
NW	nanowire
NWQD	nanowire quantum dot
PL	photoluminescence
QD	quantum dot
QIP	quantum information processing
QKD	quantum key distribution
QWP	quarter-wave plate
RHEED	reflection high energy electron diffraction
RMS	root-mean-square
SE	spontaneous emission
SK	Stranski-Krastanov
SPS	single photon source
TDD	threading dislocation density
UHV	ultra-high vacuum
VLS	vapor-liquid-solid
WL	wetting layer
X	exciton
XX	biexciton
XRD	X-ray diffraction

Introduction

Among different research areas, connected to widespread use of quantum technology, Quantum Information and Communication are one of the most advanced[1]. The term “Quantum Information” is used for any physical information that is encoded in quantum systems. Quantum Information Processing (QIP) deals with the manipulation of quantum information, to perform tasks, which are unachievable in a classical context, for instance, an absolute secure transmission of information, known as quantum cryptography[2].

Nowadays, widely developed optical fiber networks provided an availability of commercial quantum cryptographic systems, where secure keys are encoded by quantum bits (qubits) – the basic unit of Quantum Information, which refers to the state space of a two-level quantum system[1–3]. So, the long-term goal of the QIP is a creation of a large quantum network (the Quantum Internet), over which photons will transport quantum information to specific quantum nodes (Quantum Computers), where it would be processed and stored[1,4].

Coming back to a simpler task of QIP, that is quantum cryptography, there are two main approaches for a quantum key distribution (QKD). The first based on the coding of the quantum state of a single particle and on the principle of the impossibility to distinguish reliably two non-orthogonal quantum states. Thus, security of this approach is based on the theorem prohibiting the cloning of an unknown quantum state. Due to the unitarity and linearity of quantum mechanics, it is impossible to create an exact copy of an unknown quantum state without affecting an initial state. There are many QKD protocols based on the approach, and the general one is BB84 (developed by Charles Bennet and Gilles Brassard in 1984)[5], exploiting quantum states of single photons (for instance, polarization of photons).

The second approach is based on the quantum entanglement. Two particles (including those separated in the space) can be in a correlation state, so the measurement of the selected value carried out on one of the particles will determine the result of the measurement of the value on the second particle. Basic QKD protocol exploiting, for instance, pair of polarization-entangled photons is E91 (developed by Artur Konrad Ekert in 1991)[6]. For example, spherically symmetrical atom emits two photons in opposite directions. These photons have an indefinite circular polarization, but due to the symmetry their polarizations are opposite. The polarizations became known only after the measurement. An interception of one photon of an entangled pair (the measurement of the photon polarization) leads to the instant termination of the entanglement, so the presence of an interference with the cryptographic system can be understood by measuring Bell inequality.

At the present time, there are several solid-state sources for generation of single and/or entangled photons. For instance, entangled photon pair sources can be achieved by spontaneous parametric down-conversion (SPDC) in nonlinear crystals[7,8], intracavity atomic ensembles[9], and biexciton (XX) – exciton (X) cascade emission of quantum dots (QDs)[1,3,8].

Among all these sources, QDs are considered as an ideal one and can be used for both QKD protocols. As a source of single photons, QDs emit highly indistinguishable photons with gigahertz repletion rate on demand[1,10].

The present work is aimed for the fabrication of QDs on GaAs(111)A substrates. The main focus lies on the popular InAs/InAl(Ga)As QDs obtained by Droplet Epitaxy (DE) technique on vicinal GaAs(111)A, exploiting C_{3v} symmetry of the surface to obtain highly symmetric QDs and using step-flow growth mode of the vicinal surface to have possibility to grow thick buffer layers, especially thick layers of distributed Bragg reflectors (DBRs), for entangled photon emission at telecom band (1.31 – 1.55 µm).

Chapter 1 describes the concept of QD as a source of entangled photons. Also, there is a review of epitaxial fabrication of semiconductor QDs for single and entangle photon generation.

Chapter 2 gives an overview of the history of molecular beam epitaxy (MBE) as a basic epitaxial growth technique, the processes during the epitaxial growth, and the main *in situ* monitor technique – Reflection High Energy Electron Diffraction (RHEED).

Chapter 3 discusses in detail the method for QD fabrication, used in this work – DE technique.

Chapter 4 describes the experimental setups used in the work. There is an overview of MBE machine, the morphology characterization technique – Atomic Force Microscopy (AFM) and the low temperature confocal microscopy setup to analyze optical properties of telecom DE InAs QDs.

Chapter 5 discusses DE QD fabrication on (111) surfaces and presents results on GaAs QD self-assembly on singular GaAs(111)A substrates.

Chapter 6 demonstrates the study of the fabrication of GaAs QDs and In droplets on vicinal GaAs(111)A substrates.

Chapter 7 presents first experimental results on the fabrication of telecom DE InAs QDs on vicinal GaAs(111)A substrates for entangled photon pair generation.

Part I. Background

Chapter 1. QD as an ideal source for polarization entangled photon pair generation

What is making QDs so attractive for this purpose?

There are many advantages of QD as an entangled photon emitter. A wide range of semiconductor materials can cover all desired wavelengths. For instance, GaAs/AlGaAs QDs emit about 700 – 800 nm, which is compatible with quantum memory and quantum repeater technology based on Rb atoms[11–13]. If we want QD emission at telecom band for optical fiber networks, we can choose InAs/InGa(Al)As QDs[14,15]. Blue and ultraviolet wavelengths can be achieved with QDs based on Nitrides[16,17]. III-Nitrides QDs also can emit at room temperature due to high exciton binding energy.

There are different techniques for epitaxial QD fabrication such as Stranski-Krastanov (SK) growth mode[3,8,14,16], DE[1,3,8,13], and nanowire quantum dots (NWQDs)[17].

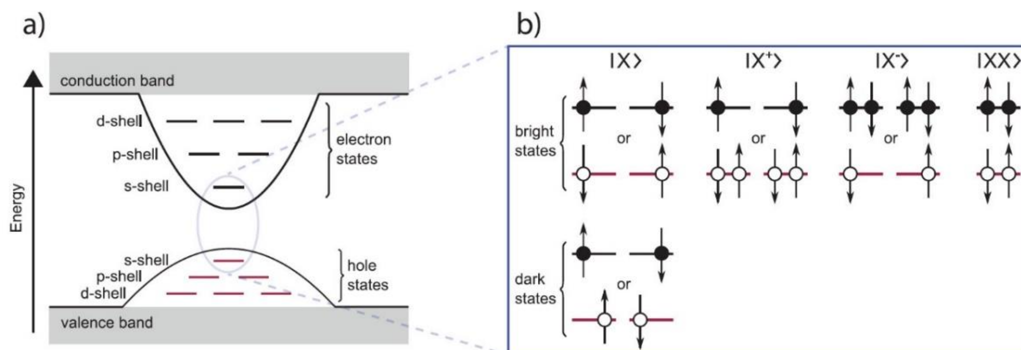

Figure 1.1. (a) Schematic energy potential of a quantum dot. The quantum dot potential can be approximated by a two-dimensional (2D) harmonic oscillator model with different effective masses for electron and holes. The first three quantized electronic (black) and hole (red) levels are illustrated. (b) Illustration of the nine s-shell states' charge carrier configurations. The resulting quantum states are defined by the number of electrons (filled circles) and holes (empty circles) and their respective spin configuration (direction of arrows). The dark exciton state has a parallel spin configuration, resulting in an optically inactive state with a long lifetime[8].

But the main advantage of QDs is the generation of entangled photons on demand. Let us consider only the lowest energetic level for electrons and holes in the conduction and valence bands of QD, so called s-shell (see Figure 1.1.a). The s-shell conduction band can be maximally occupied by two electrons with different spin configuration, due to the Pauli exclusion principle. Same the s-shell valence band can be occupied by two holes. Therefore, there are only 9 possible electron-hole configurations in the s-shell of QD (see Figure 1.1.b). Due to the optical selection rules, two configurations in the s-shell, where both the electron and hole have the same spin configuration are optically inactive and are called dark excitons[1,3,8].

An important excitation state in the QD s-shell, to obtain entangled photon pair, is a fully occupied s-shell with two electrons and two holes, forming two excitons. This is called a biexciton (XX) state. One electron hole pair (first bright exciton) can recombine, emitting first single photon and leaving QD in the second bright exciton state. Then, the remaining exciton also recombines, emitting second single photon. This is called the biexciton (XX) – exciton (X) cascade (see Figure 1.2). The direct transition from XX state to the ground (G) state only with one photon is impossible.

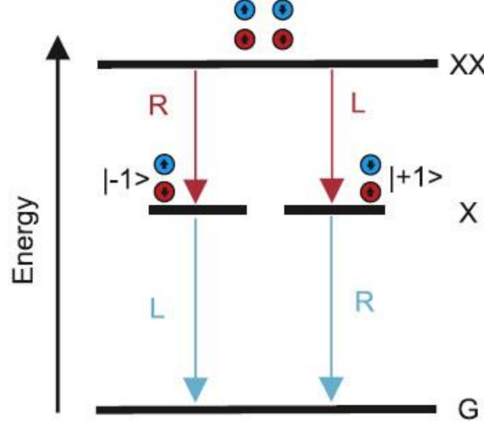

Figure 1.2. The XX-X cascade. The XX state decays under the emission of a right circular (R) (left (L)) polarized photon to a single X state, which subsequently decays to the G state under the emission of an orthogonal-circular polarized photon. The polarization of the emitted photons is governed by the electron and hole spin configuration of the recombining electron-hole pair[3].

The cascade follows either the left or right decay channel – in ideal case degenerated in energy – leading to a sequence of circular right (R) biexciton and circular left (L) exciton photons, or vice versa. The probability to decay by the left or right channel is 50% and without measuring we cannot distinguish the polarization of photons. But when we measure the polarization of the first photon, we immediately know the polarization of the second. Therefore, the polarization of these two photons is entangled and the resulting two-photon state can be written as:

$$|\psi\rangle = \frac{1}{\sqrt{2}}\left(|R_{XX}\rangle|L_X\rangle + |L_{XX}\rangle|R_X\rangle\right), \tag{1.1}$$

where R_{XX} (L_{XX}) and R_X (L_X) are biexciton and exciton photons in the circular right (left) polarization base, respectively. The two-photon state can be rewritten in terms of horizontal (H) and vertical (V) polarization, by using $|H\rangle = \frac{1}{\sqrt{2}}\left(|R\rangle + |L\rangle\right)$ and $|V\rangle = \frac{i}{\sqrt{2}}\left(|R\rangle - |L\rangle\right)$ [3]:

$$|\psi\rangle = \frac{1}{\sqrt{2}}\left(|H_{XX}\rangle|H_X\rangle + |V_{XX}\rangle|V_X\rangle\right). \tag{1.2}$$

Since only one XX can occupy the s-shell of a QD at a time as well as the finite and short lifetimes of XX and X, the QD is the polarization entangled photon pair source on demand.

QDs suffer from different entanglement degrading effects such as recapture processes, valence band mixing or spin-flip processes[3,8]. However, the main requirement for QDs to be an ideal entangled photon emitter is a low fine structure splitting (FSS) of X state, induced generally by an asymmetry of QD shape or the composition[1,3,8,13]. The presence of the FSS destroys polarization entanglement because the energy of photons of left or right decay channels are different and we can distinguish the polarization by measuring the photon energy (see Figure 1.3).

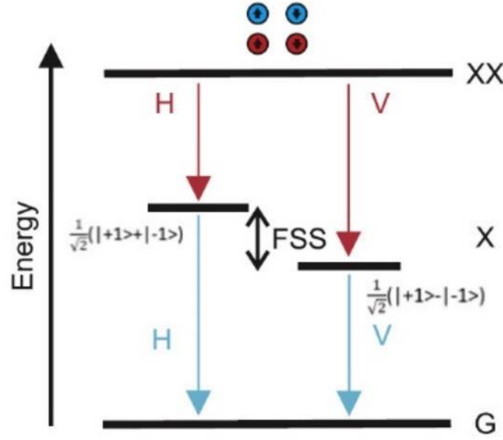

Figure 1.3. The effect of the fine structure splitting (FSS) on the XX-X cascade. The anisotropic exchange interaction causes the intermediate exciton state to be energetically split by the FSS. Consequently, a mixing of the exciton states appears, leading to the emission of two horizontally polarized photons (H) (vertically polarized photons (V))[3].

The origin of the splitting can be described by the electron-hole exchange interaction[3,8]:

$$\hat{\mathrm{H}}_{FS} = -\sum_{i=x,y,z} \left(a_i \hat{S}_{h,i} \cdot \hat{S}_{e,i} + b_i \hat{S}^3_{h,i} \cdot \hat{S}_{e,i} \right), \tag{1.3}$$

where $\hat{S}_{h,i}$ ($\hat{S}_{e,i}$) stand for the hole (electron) spin operator and a_i and b_i are the spin-spin coupling constants in the three spatial axes ($i = x, y, z$). In the basis of initially degenerate bright and dark exciton states, denoted according to their spin projections $|+1\rangle$, $|-1\rangle$, $|+2\rangle$, and $|-2\rangle$, the matrix representations of $\hat{\mathrm{H}}_{FS}$ yields[18]

$$\hat{\mathrm{H}}_{FS} = \frac{1}{2}\begin{pmatrix} +\delta_0 & \delta_1 & 0 & 0 \\ \delta_1 & +\delta_0 & 0 & 0 \\ 0 & 0 & -\delta_0 & \delta_2 \\ 0 & 0 & \delta_2 & -\delta_0 \end{pmatrix}, \tag{1.4}$$

with the abbreviations $\delta_0 = \frac{3}{2}\left(a_z + \frac{9}{4}b_z\right)$, $\delta_1 = \frac{3}{4}\left(b_x - b_y\right)$, and $\delta_2 = \frac{3}{4}\left(b_x + b_y\right)$. As illustrated by the block-diagonal form of $\hat{H}_{FS}$, the bright ($|\pm1\rangle$) and dark ($|\pm2\rangle$) excitons do not mix and are split according to δ_0. The off-diagonal elements δ_1 and δ_2, however, lead to a splitting of both, bright and dark excitons, forming new eigenstates as symmetric and antisymmetric combinations[18]. In case of symmetrical QD, $\delta_1 = 0$ ($b_x = b_y$), and there is no FSS.

The FSS of the bright exciton can be observed via the splitting of the X transition line. In the case of the XX state, both electron and hole spins are in a singlet state, resulting in no fine structure for the XX state. However, one will still observe the FSS in the emitted biexciton photons' energy since the XX state recombines into the intermediate X state. Therefore, the excitonic FSS can also be measured in the spectrum of the biexciton photons, as shown in Figure 1.4.

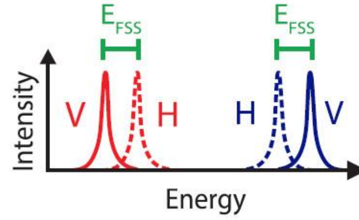

Figure 1.4. The emission spectra of XX-X cascade with non-zero FSS[8].

The FSS leads to an exciton-spin precession , which directly affects the polarization state (the two-photon state is no more time-independent)[3,8]:

$$|\psi\rangle = \frac{1}{\sqrt{2}}\left(|H_{XX}\rangle|H_X\rangle + e^{\frac{i\tau_x E_{FS}}{\hbar}}|V_{XX}\rangle|V_X\rangle\right), \tag{1.5}$$

where τ_x is the time interval between the XX and X photon emission. In practice, this leads to an oscillation between two possible eigenstates. The photons of QD with FSS are still maximally entangled, but the resolution of the experimental setup should be good enough to resolve the oscillations with the time $t = \frac{2\pi\hbar}{E_{FS}}$. Therefore, only a narrow subset of the decay events can be used as well-defined entanglement sources[3].

High value of the FSS makes unpractical the use of QDs for entangled photon pairs generation. However, employing different filtering schemes (spectral or temporal), it is possible to increase the range of an acceptable FSS value and still generate a substantially strong entanglement[3,19,20]. But, of course, the lowering the FSS is the main goal of QD fabrication for entangled photon generation.

1.1. QDs with the low FSS

As mentioned above, the FSS is generally induced by anisotropy of QD shape or composition[1,3,8]. Thereby, it is reasonable to fabricate symmetrical QDs to eliminate the FSS.

Over the decades only a strain-induced SK growth technique was known for an epitaxial QD fabrication. Thereby, a photon entanglement has been studied on SK In(Ga)As QDs grown on GaAs(001) substrates[21,22]. But QD fabrication with the low FSS on (001) surface of zinc-blend crystals is a challenge due to the strain and surface diffusion anisotropy in the $[110]$ and $[1\bar{1}0]$ directions. The probability to find a good In(Ga)As QD with the low FSS value below 1 μeV (a "hero" QD) is in the order of few percent[22]. Nevertheless, successful attempts of SK dot fabrication with the low FSS were done. For instance, large low-strain $In_{0.3}Ga_{0.7}As$ QDs show the FSS below 10 μeV on average due to the fact that the shallow confinement potential lowers the sensitivity of the wavefunction with respect to structural asymmetries of the QD[23].

Also, In(Ga)As materials has In-related large nuclear Overhauser field (an effective magnetic field, generated collectively by nuclear spins, decreasing the spectral diffusion of the electron spin)[24], which leads to a fluctuations of the FSS over time[25]. Therefore, GaAs/AlGaAs semiconductor system became more promising for entangled photon generation due to smaller nuclear spin of Ga (3/2) compare to In nuclear spin (9/2), thus minimizing the perturbation of the FSS by Overhauser effect[26].

However, GaAs and AlAs crystals have a very small lattice mismatch. On the one hand, it should decrease the influence of strain and piezoelectricity on the FSS value, but on the other, SK GaAs/AlGaAs QDs fabrication is impossible due to no strain in the epilayers.

There are several approaches permitting the fabrication of epitaxial GaAs/AlGaAs QDs. The first is the DE technique[1,3,13], which is described in Chapter 3. DE relies, for QD fabrication, on the kinetically controlled crystallization, via annealing in group V atmosphere, of previously formed nanodroplets of group III metals[1]. DE allows to control the size and density of QDs in wide range and more significant the shape of self-assembled nanostructures. Another approach, which originated from DE, is local droplet etching (LDE) technique[1,3,27] (also described in Chapter 3). This method is the fabrication of QDs by etching of nanoholes after droplet nucleation (instead of the crystallization step in DE)[27]. The nanoholes are subsequently filled with a semiconductor material different from the etched surface, and capped, after annealing, with barrier material. LDE allows to fabricate highly symmetric GaAs QDs on AlGaAs(001) surface with a very low FSS value (see Figure 1.5). So far, the highest level of entanglement fidelity of 0.94 without either the temporal post-selection or the external tuning has been measured from GaAs QDs with a finite

FSS value of 1.2 μeV fabricated by LDE method[28]. The fidelity is the measure of "closeness" of two quantum states. The fidelity is equal to 1 if the states are perfectly identical, it is equal to zero if they are orthogonal. The fidelity between the reconstructed state and a Bell state is an entanglement witness: if the fidelity is larger than 1/2 then two states are entangled[29].

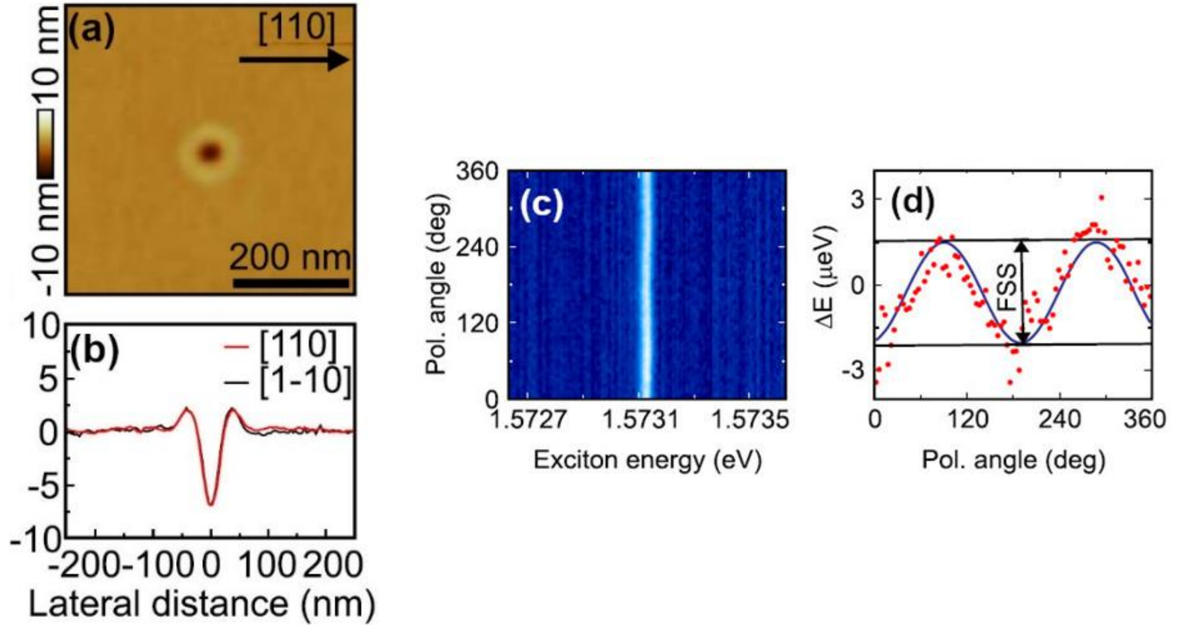

Figure 1.5. (a) AFM image and (b) corresponding linescans along $[110]$ and $[1\bar{1}0]$ crystal directions of AlGaAs surface prior to GaAs filling. Nanoholes are obtained by Al-droplet etching. (c) Polarization-resolved μ-photoluminescence (μ-PL) spectra of neutral exciton emission from representative GaAs QDs, obtained by filling nanoholes. (d) The emission energy obtained by Lorentzian fits of the spectra as a function of polarization angles. The linear-polarization angles of 0º and 90º correspond to the $[110]$ and $[1\bar{1}0]$ crystal directions[30].

Another way how to decrease the FSS value is the use of (111) growth surfaces with natural C_{3v} symmetry instead of (001) surfaces with D_{2d} symmetry. It has been predicted theoretically (see Figure 1.6) that QD structures fabricated on (111) surfaces feature a vanishing the FSS[31]. Then, a great suppression of the FSS[32] and high entanglement fidelity of 0.86 without post-selection[33] have been demonstrated experimentally in self-assembled GaAs QDs grown on AlGaAs(111)A surface.

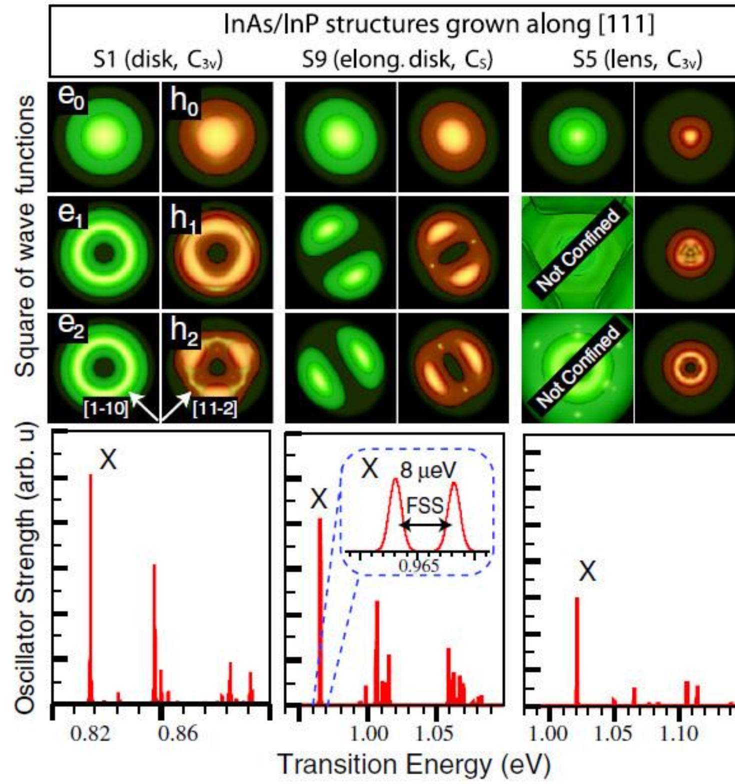

Figure 1.6. Square of the wave functions for the first three electron (e_0, e_1, e_2) and hole (h_0, h_1, h_2) states of the structures S1 (disk-shaped QD), S5 (lens-shaped QD), and S9 (elongated disk-shaped QD) grown along [111] direction. The isosurfaces enclose 75% of the probability densities. Corresponding absorption spectra in arbitrary units. The inset for structure S9 is a blowup of the excitonic line separated by the FSS (lower part)[31].

For the fabrication of any QD systems (with or without strain) on (111) surfaces, it is necessary to use DE. SK growth technique is almost impossible on (111) surfaces due to the low threshold energy for compressive strain relaxation in epitaxial layers by the insertion of misfit dislocations at the substrate–epilayer interface[34,35]. Recently self-assembly SK GaAs QDs on InAl(Ga)As(111)A surface were demonstrated[36–38] by turning from compressive to tensile strain. And even these tensile strained SK GaAs QDs grown on InAlAs/InP(111)A show low FSS value below 10 μeV[36].

Using DE technique, highly symmetrical GaAs/AlGaAs(111)A QDs with a triangular and hexagonal shape have been demonstrated[39,40] to improve the yield of entanglement–ready photon sources up to 95%[13]. Additional advantage of last works on DE GaAs QD fabrication on (111) surfaces[13,40] compare to pioneering studies[32,33] and DE QD fabrication on (001) substrates is the use of much higher temperature for droplet crystallization. It improves the crystal quality of grown materials and subsequently optical properties and brightness of QDs without any post annealing steps, but also shift their wavelength emission.

1.2. Energy and FSS tunable sources of entangled photons

Still to produce high number of QDs with zero FSS on one chip is a complicated task. Moreover, it is necessary for future application in quantum communication to entangle photons from different sources, and these photons should be indistinguishable. Therefore, it requires that different QDs should emit identical entangled photon pairs, the emission wavelength of photons from different QDs should be matched.

To control emission wavelength of QDs, it is possible to use external perturbations, which is also can affect on an anisotropy induced FSS. The first approach is to use an external electric field. The electric field causes the Stark effect, shifting spectral lines of QDs and consequently the emission wavelength. Such devices consist of an intrinsic layer of QDs, embedded in a p-i-n doped planar microcavity[41,42]. Applying an electric field, it is possible to tune energy levels of QDs and, therefore, to change the emission energy of XX-X cascade (see Figure 1.7). Also, for practical applications, such as an optical quantum computing, it is important to have an electrically driven entanglement source.

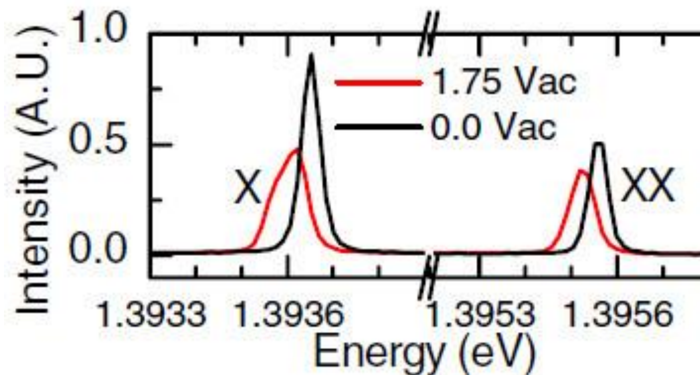

Figure 1.7. Spectrum of emission from entangled-light-emitting diode under direct current (DC) and alternating (AC) excitation. A sinusoidal AC voltage was applied together with a DC bias[41].

An interesting concept of tunable entangled light emitting diode is presented in the work of Toshiba's Cambridge Research Laboratory[43]. The concept combines electrically tunable and optically pumped QD device (see Figure 1.8a). This device is optically excited by light emitted from the so-called 'pumping diode' surrounding it, when applying a forward bias to the top contact on the left. A reverse bias applied to the top contact from the inner diode is used to apply static fields for tuning the QD emission, making this the so-called 'tuning diode'. The device is fully electrically operated with wavelength tuneability of more than 25 nm (see Figure 1.8b) and with the tuning of the FSS below 10 μeV (see Figure 1.8c), resulting in electrically triggered entangled photon pair generation.

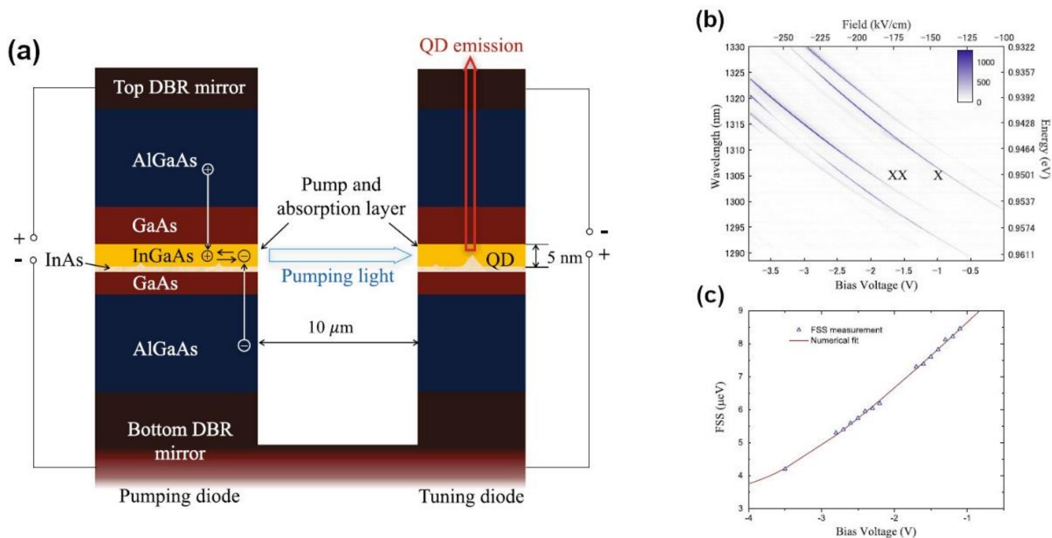

Figure 1.8. (a) Concept of device. The central 5 nm InGaAs layer serves as pump and absorption layer for the on-chip optically excited device. It generates light at 950 – 1000 nm in the pumping diode (left) which is absorbed in the tuning diode (right), exciting QDs. The shown layer thicknesses are not to scale. DBR represents the distributed Bragg reflector. (b) Emission spectrum of on-chip optically excited single quantum dot (QD) as a function of applied bias voltage to the tuning diode. A wavelength shift of around 30 nm is observed for XX and X emission. (c) Corresponding change of the FSS of the QD as a function of the applied bias. The values were extracted via a numerical fit to measured polarization-filtered time-resolved photon-pair correlations. Error bars determined by the standard error from the numerical fit are negligible. The red curve is a numerical fit based on the theoretical model for dependence of the splitting due to the quantum confined Stark effect[43].

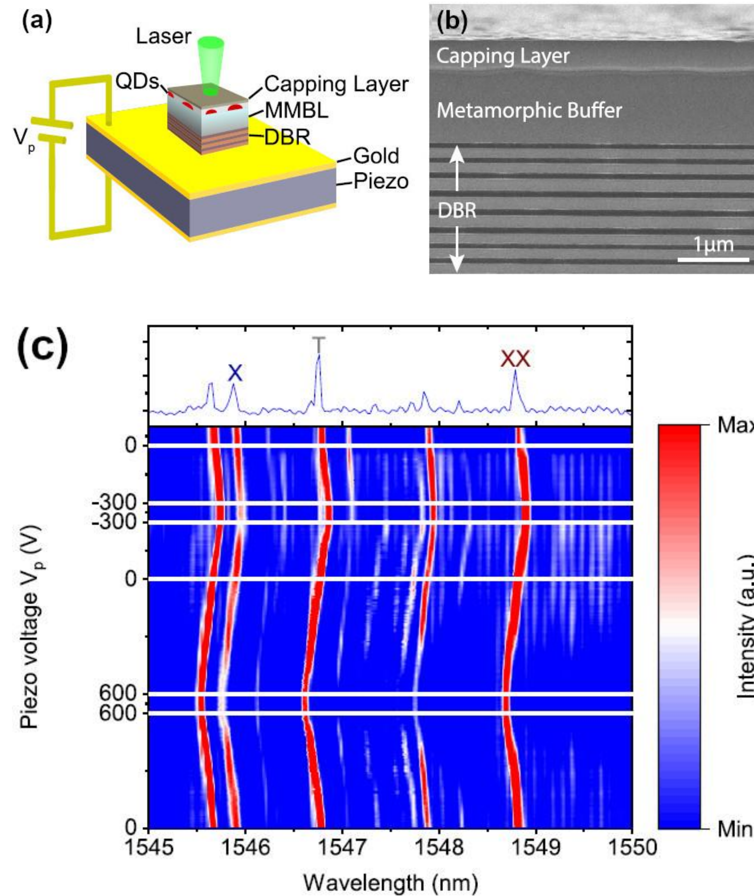

Figure 1.9. (a) Sample schematic: the mechanically thinned sample glued to a piezoelectric element. (b) SEM image of a cleaved facet of the non-thinned sample. From bottom to top: DBR layers, metamorphic buffer layer, QDs, and capping layer. (c) Top image: PL spectrum of QD at 0 V, denoted are exciton (X), trion (T), and biexciton (XX) states, and the intensity is plotted in arbitrary units. Bottom image: QD emission as a function of applied voltage to the piezo in an overall range of 900 V[44].

Even applying an electric field, we can tune the FSS, but it is a not optimal option to eliminate the FSS. Another approach is the use of an external strain field. Applying a strain field, it is possible to compensate an anisotropy induced FSS (in simple way – make the QD more symmetrical). The simplest device is an optically excited QD structure on a piezoelectric substrate, allowing to tune the QD emission (see Figure 1.9).

Also, piezoelectric substrate can be combined with the p-i-n diode QD structure (see Figure 1.10a). Such device can tune both, the QD emission wavelength and the FSS value (see Figure 1.10b, c).

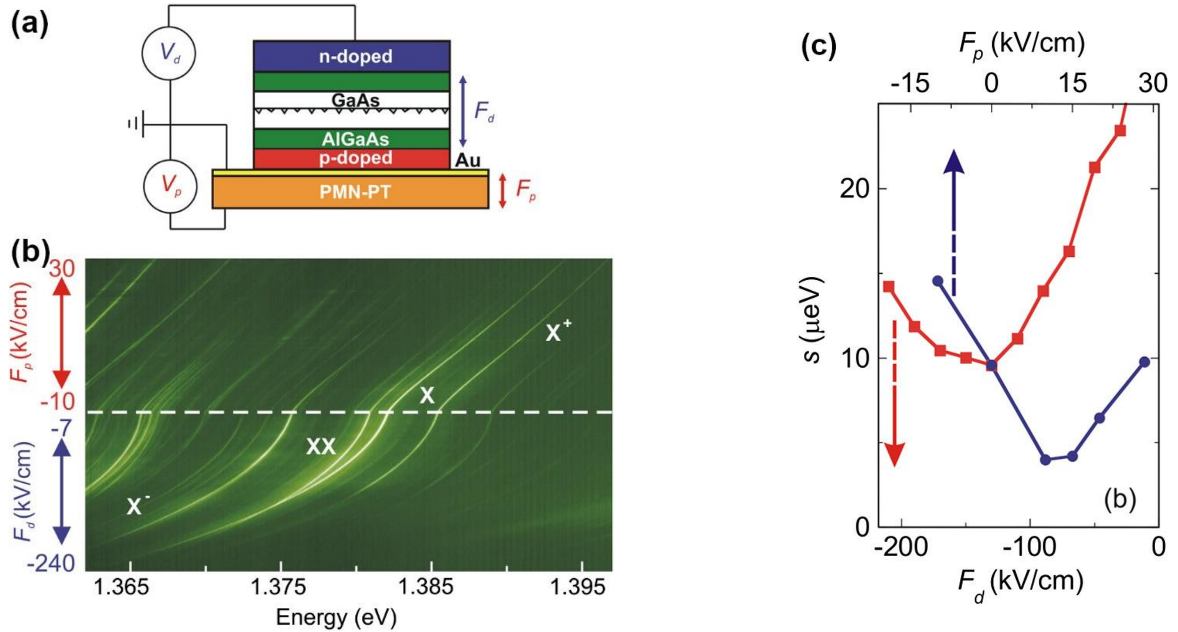

Figure 1.10. (a) Sketch of the device. An n-i-p nanomembrane is integrated on top of a piezoelectric actuator allowing the in-situ application of anisotropic biaxial strains [in the (001) plane of the GaAs nanomembranes] by tuning the voltage (electric field) V_p (F_p). Independently, a voltage applied to the nanomembrane (V_d) allows the electric field (F_d) along the [001] direction to be controlled. (b) μ-PL map of a single QD as a function of F_p and F_d. The two fields were varied one after the other, i.e., F_p = -10 kV/cm when F_d is ramped up (bottom), whereas F_d = -7 kV/cm when F_p is ramped up (top). The abscissa indicates the energy of the emitted photons. The ordinate indicates the value of F_p and F_d used in the experiment. The exciton (X), biexciton (XX), and charged exciton (X^+ and X^-) transitions from the same QD were identified by polarization-resolved μ-PL spectroscopy[45].

The next generation improvement was done by applying several in-plane piezoelectric distortions. J. Wang *et al.* demonstrated the full suppresion of FSS by applying two independent in-plane strain components[46,47]. But for energy tuning, a second independent stressor is placed on top of the sample. The extraction of the photons, however, requires the technologically challenging use of a transparent strain transmitter between the sample and the top stressor.

R. Trotta *et al.* proposed to use the six-legged semiconductor-piezoelectric device for quantum optics with three independent in-plane stressors[3,12]. Two pairs of legs of the device can be used to fully erase the FSS, while the third leg enables energy tuning at a fixed FSS. As the membrane is open to the top, the emitted photons can be easily collected by microscope objectives. Furthermore, the structure enables the possibility of using QDs embedded in a diode structure to electrically pump the entangled photon source[41–43].

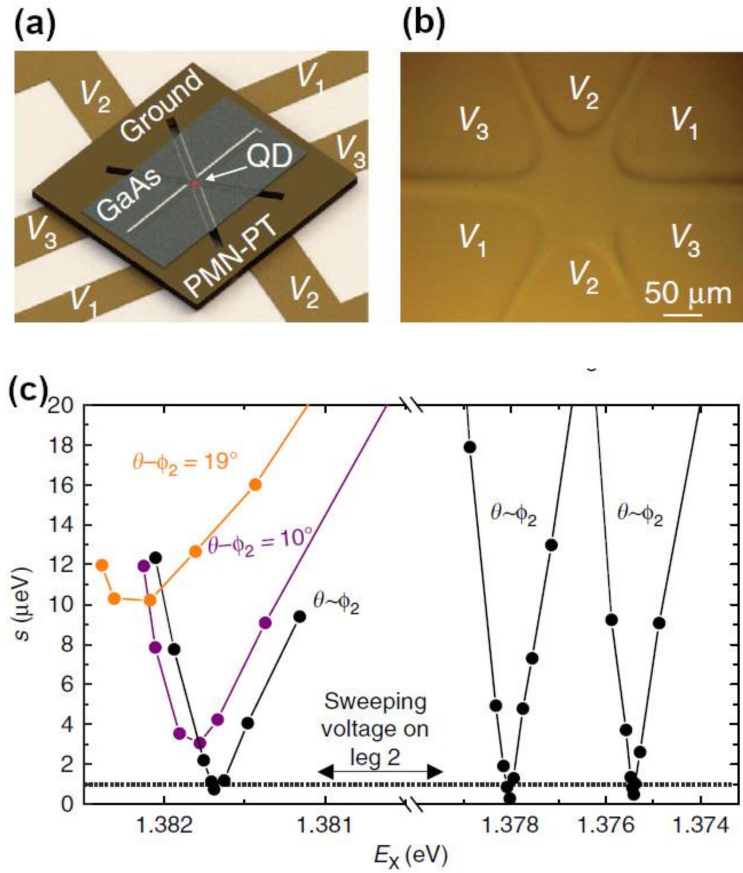

Figure 1.11. (a) Sketch of the six-legged semiconductor-piezoelectric device for quantum optics used to engineer the strain status of a nanomembrane (grey region) containing QDs. (b) Microscope picture of the central part of the final device. (c) Tuning the exciton energy at zero fine structure splitting. Behavior of the FSS as a function of E_X. The dashed line shows the threshold of 1 μeV[12].

Finally, such piezoelectric structure was combined with the highly entangled photon pair QD source without any temporal post-selection – GaAs/AlGaAs QDs, fabricated by LDE approach[48]. An entanglement fidelity is achieved up to 0.978 after taking into account setup-related entanglement deteriorating effects (phase shifts induced by the optical elements and laser background). It is indicated the presence of almost negligible, albeit nonzero, decoherence mechanisms, likely related to spin-scattering. And authors suggest that this imperfection may be overcome using a Purcell enhancement to achieve fidelities > 0.99, thus making quantum dots evenly matched with the best probabilistic entangled photon sources.

1.3. QD as a single photon emitter

Another limitation of QDs in QIP applications is a low extracting efficiency of entangled photons or the brightness of the QD source. Since the brightness is mainly addressed to the perspective of the single photon source (SPS), it is necessary to introduce the idea of using QDs as the SPS.

The SPS emits only one photon at a time. QDs can act as the single photon emitters and produce single photons on demand via the decay of a single exciton, as mentioned above. The verification of nonclassical light (single photon behavior) by measuring the photon number distribution is experimentally hard to obtain, since the occurrence of random sampling due to optical losses or imperfect detectors causes the photon numbers to attain Poissonian character as a classical light source. But the verification of single photon behavior can be done via the degree of anti-bunching reflecting the occurrence of multi-photon generation. It is measured by the equal-time intensity auto-correlation function $g^{(2)}$ (0), which is related to the photon number (n) statistics according to:

$$g^{(2)}(0)=\frac{\langle n(n-1)\rangle}{\langle n\rangle^{2}}=1-\frac{1}{n}. \tag{1.6}$$

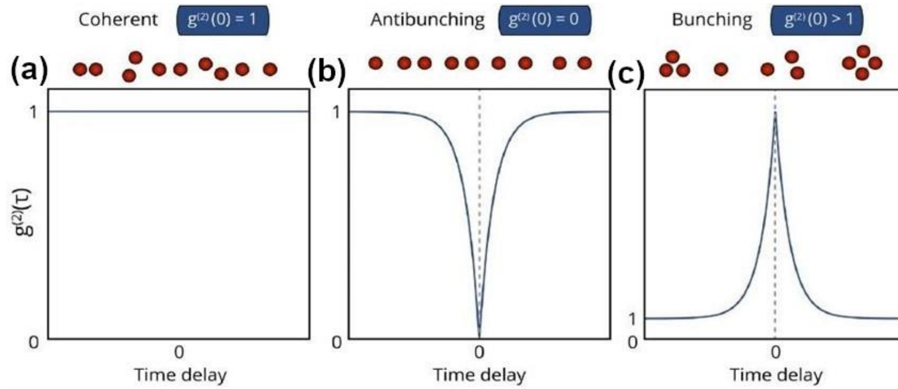

Figure 1.12. Examples for the intensity auto-correlation function of (a) a coherent light source (laser), (b) a single photon emitter, and (c) a classical light source – thermal radiation.

For a classical light $g^{(2)}$ (0) > 1 and $g^{(2)}$ (0) = 1 for coherent light (laser). For a true SPS $g^{(2)}$ (0) = 0 and in case of two photon generation $g^{(2)}$ (0) = 0.5. Therefore, $g^{(2)}$ (0) should be less that 0.5 and it is an upper limit for the light source to be considered as a single photon emitter.

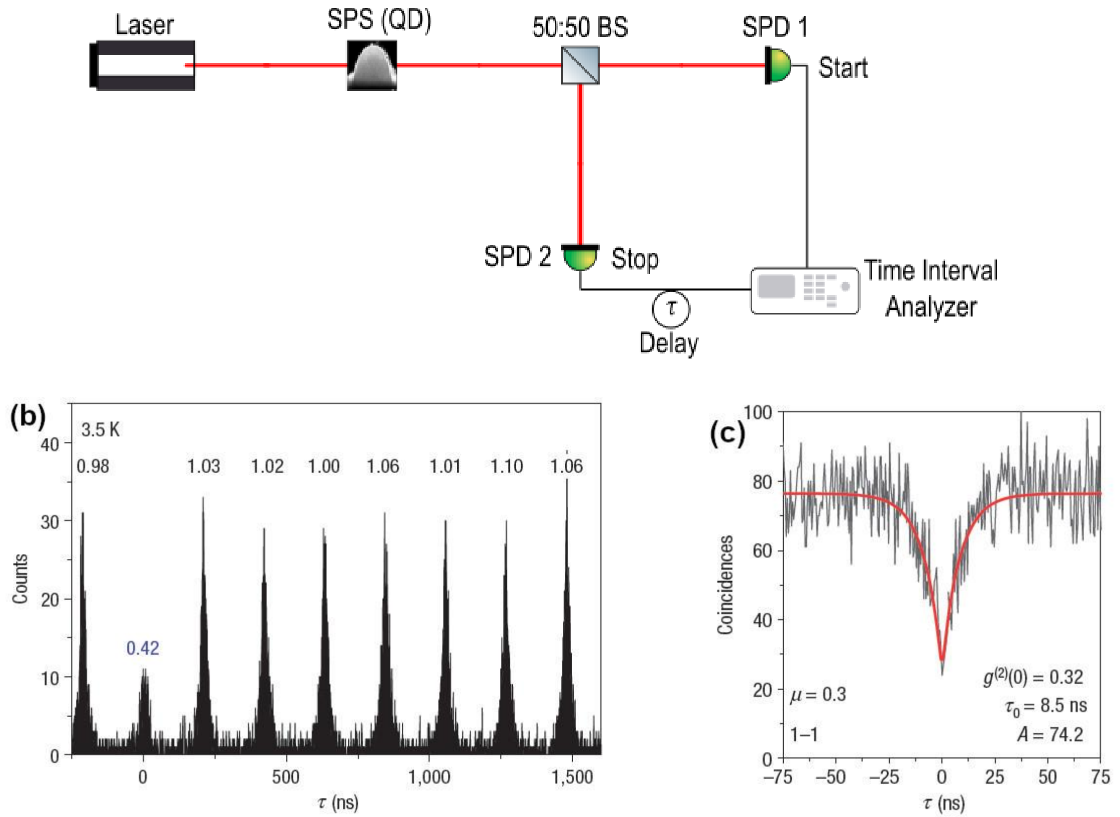

Figure 1.13. (a) Scheme of the HBT type setup for the intensity autocorrelation function $g^{(2)}(\tau)$ measurement. (b) Photon-correlation measurement under pulsed excitation of GaN/AlN self-assembled QD at 3.5 K. The numbers printed above the peaks give the normalized peak areas after correcting for the detector dark counts[16]. (c) Photon-correlation measurement under continuous-wave excitation of GaN/AlN self-assembled QD. Histograms under continuous-wave excitation as a function of the relative delay τ between photons detected by the 'start' and 'stop' at the time-interval counter. The solid red line and numbers show the fitting curve and fitting parameters, respectively[16].

In practice, the intensity auto-correlation function $g^{(2)}(\tau)$ can be measured in a Hanbury Brown and Twiss (HBT) type setup, presented in Figure 1.13a, which was originally applied in astronomy to monitor spatial coherence of a classical light[49]. The photon correlation measurement can be caried out under pulsed or continuous laser excitation. The light signal from SPS is split in a 50:50 beam-splitter (BS), photons of the same transition (auto-correlation) or different transition (cross-correlation) are selected to trigger the start and stop inputs by single photon detectors (SPDs). In case of pulsed laser excitation, it gives a correlation histogram of coincidence counts versus time difference, as shown in Figure 1.13b taken from[16]. In the second case, a histogram of delay times between two arbitrary photons detection events are created (see Figure 1.13c). And the recorder histogram is proportional to the second-order auto-correlation function $g^{(2)}(\tau)$ of detected signal.

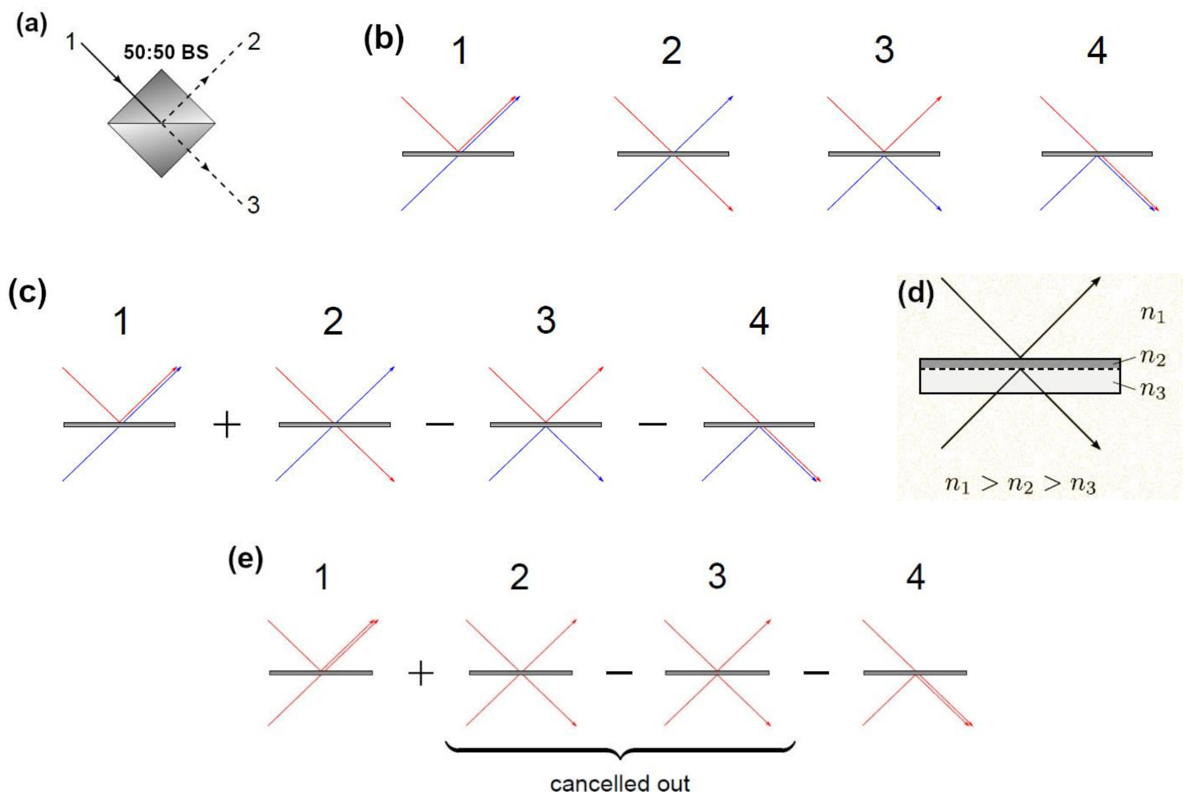

Figure 1.14. Physical description of the two-photon interference. (a) A single photon entering a 50:50 BS can be transmitted or reflected. (b) Four possibilities for two photons entering a 50:50 BS one in each input mode. (c) Superposition of all possibilities for two photons to pass through the BS. (d) Explanation of an appearance of the phase shift for photons reflect off different sides of BS. (e) Superposition and cancellation of two possibilities for two identical photons passing through the BS. Red and blue arrows represent not identical photons.

Apart from the purity SPS should also generate indistinguishable photons[1,10], which is also a necessary property of entangled photon sources. Ideally, not only the photons subsequently emitted by a single QD but also photons emitted by different emitters should be indistinguishable for the implementation of a quantum network, which is largely more demanding[1]. How we can measure indistinguishability of photons coming from SPS? Let us consider a single photon, which enters a 50:50 BS. There are two possibilities: it will either be transmitted or reflected (see Figure 1.14a). In case of two photons, one in each input mode of the BS, there are four possibilities of two-photon reflection and transmission (see Figure 1.14b). The state of the system of two photons after interference is given by a superposition of all possibilities for the photons to pass through the BS as presented in Figure 1.14c. The minus sign comes from considering the reflection of a photons coming from different sides of the BS. Reflection from the bottom side leads to a relative phase shift of π (the light reflects off the higher index medium). Reflection from the top side leads to no phase shift (reflection from the lower index medium) (see Figure 1.14d). And finally, if two photons are identical in their physical properties (polarization, spatio-temporal mode profile, frequency etc.), it is impossible to distinguish between the output states of possibilities 2 and 3, and their relative minus sign ensures that these two terms cancel (see Figure 1.14c). This can be

interpreted as destructive interference. Thus, the photons will always exit the same (but random) output port of BS. This is a two-photon interference.

The two-photon interference was discovered by Hong, Ou and Mandel[50], therefore, it is known as the Hong-Ou-Mandel (HOM) effect. HOM effect was originally used to measure the time intervals between two photons, and the length of the photon wave packet, produced in the process of parametric down-conversion[50].

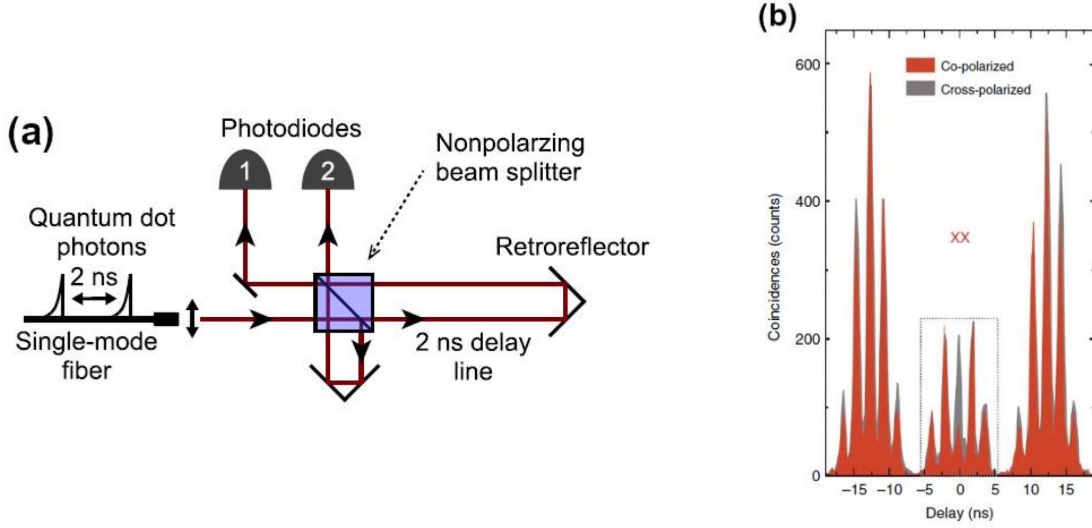

Figure 1.15. Measurement of indistinguishability. (a) Schematic of a HOM type setup to measure the indistinguishability of two photons emitted from a QD that is excited 2 ns apart. They are sent to an unbalanced Michelson interferometer and then to detectors[51]. (b) Two-photon interference with co-polarized (red) and cross-polarized (grey) XX photons[28].

HOM type setup for indistinguishability measurements of photons is shown in Figure 1.15a. An unbalanced Mach-Zehnder interferometer can be used to compensate a respective excitation time gap of two single photons, generated in a SPS by two delayed laser pulses[51]. Also, it could be two photons generated by different quantum emitters. These two photons enter the BS at the same time, after the photons can be detected by SPD connected to a time-to-digital converter. If the two photons are indistinguishable in all degrees of freedom, they will always leave the beam splitter through the same output port as shown above. Hence, a measured histogram will show no coincidence counts between the detectors at zero-time delay. The result of such a measurement is shown in Figure 1.15b. The co-polarized (indistinguishable in polarization) photons show a drop in the central peak with respect to the cross-polarized photons (fully distinguishable). The visibility (the degree of indistinguishability) is given by[3]:

$$V = 1 - \frac{g_{\parallel}}{g_{\perp}}, \tag{1.7}$$

where $g_{||}$ and $g_{\perp}$ are the integrated peak areas around the zero-time delay for co-polarized and cross-polarized photons, respectively. A visibility equal to 1 indicates perfect indistinguishability, while $V = 0$ denotes fully distinguishable photons.

As for entangled photon emitters QDs grown by the LDE technique show also good performance for single photon generation. It was demonstrated that LDE GaAs/AlGaAs QDs have the lowest value of $g^{(2)}(0)$ reported for any SPS[52]. Authors presented a solid-state source of on-demand single photons yielding a raw second-order coherence of $g^{(2)}(0) = (7.5\pm1.6)\times10^{-5}$ without any background subtraction or data processing. Also, such dots show the high degree of indistinguishability for both X and XX photons. The measured visibilities of two-photon interference are 0.86±0.09 and 0.93±0.07 for X and XX photons, respectively[28].

1.4. Increasing the brightness

Already mentioned, another important parameter of single and entangled photon emitters is the brightness. The low brightness of QD-based sources arises mainly from a small extraction efficiency. The extraction efficiency η of microstructures, designed around the quantum dot, is given by[51]

$$\eta = \beta\times(1-\alpha) \text{ with } \beta = \frac{\Gamma}{\Gamma+\Gamma_{other}}, \tag{1.8}$$

The term (1 – α) describes the fraction of the emitted light collectible via the objective lens (with a given numerical aperture of the collection optics). The β factor accounts for the spontaneous emission (SE) rates in a specific target mode. Γ and Γ_{other} are the SE rates of the QD transition, respectively, into the microstructure mode and into all the other modes. Thus, increasing Γ or reducing Γ_{other} improves the β factor and hence the source brightness[3,51].

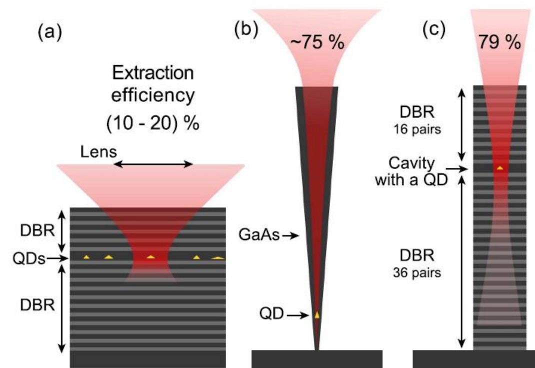

Figure 1.16. Extracting quantum dot photons. (a) A quantum dot sandwiched between two asymmetric DBR mirrors allows for up to ≈ 10 – 20% collection efficiency. (b) Brightness of ≈ 75% has been seen with a quantum dot inserted in the bottom of an inverted trumpet structure. (c) Ultrabright sources (79% collection efficiency) of single and indistinguishability photons have been made by coupling a quantum dot to a micropillar cavity[51].

There are several approaches to increase the brightness of QD-based single photon and entangled photon devices.

1. *Enhancement of the SE rate Γ into a cavity target mode exploiting the Purcell effect (cavity approach)*

The engineered photonic environment boosts both the brightness of the sources and the indistinguishability of the emitted photons due to the Purcell effect[53], which accelerates the SE rate and mitigates the effects associated to charge noise and—in narrowband cavities—also of phonons.

The SE rate $\Gamma = 1/T_1$ can be approximated by the Fermi Golden rule for an electric dipole transition[51,54]:

$$\Gamma = \frac{2\pi}{\hbar^2}\rho\left(\omega_{QD}\right)\cdot\left|\left\langle \vec{d}\cdot\hat{\vec{E}}\left(\vec{r}_{QD}\right)\right\rangle\right|^2, \tag{1.9}$$

where $\rho\left(\omega_{QD}\right)$ is the density of photon modes at the emitter's frequency ω_{QD}, the term $\hat{\vec{E}}$ is the electric field operator, and $\vec{r}_{QD}$ is the location of the quantum dot dipole $\vec{d}$. The most known cavity design is the QD embedded in a planar λ-cavity either defined by DBRs or metal mirrors (see Figure 1.16a). The mirrors induce a vertical confinement of the light field leading to a local change in the optical mode density. Thus, the SE rate enhancement occurs when QD is located at the maximum of the cavity electric field $\vec{r}_c$ ($\vec{r}_{QD} = \vec{r}_c$) and have the same frequency as the cavity resonance frequency ω_c ($\omega_{QD} = \omega_c$). So, the ratio of the SE rate in the cavity mode Γ, over to the coupling to free space Γ_0 is proportional to the Purcell factor F_p[51,54]:

$$\frac{\Gamma}{\Gamma_0} = F_p = \frac{3Q\left(\lambda_c / n_{eff}\right)^3}{4\pi^2 V_{eff}}, \tag{1.10}$$

where λ_c is the wavelength of the cavity and n_{eff} the effective refractive index of the cavity. Therefore, cavities with high quality factors Q, and small effective mode volumes V_{eff}, can result in regimes with high Purcell factors.

Many presented works[9,14,15,19,20,29,41–44,48,52], concerning self-assembly of SK, DE or LDE QDs for single or entangled photon generation, use the planar cavity approach to increase the light extraction efficiency from QDs or just fabrication of bottom DBR to avoid the photon emission through a bottom side of the QD-based device. Still the collection efficiency is on the level of

10 – 20%. An extraction efficiency of about 56% was achieved by using a bullseye cavity (see Figure 1.17) – a circular Bragg grating[10,55].

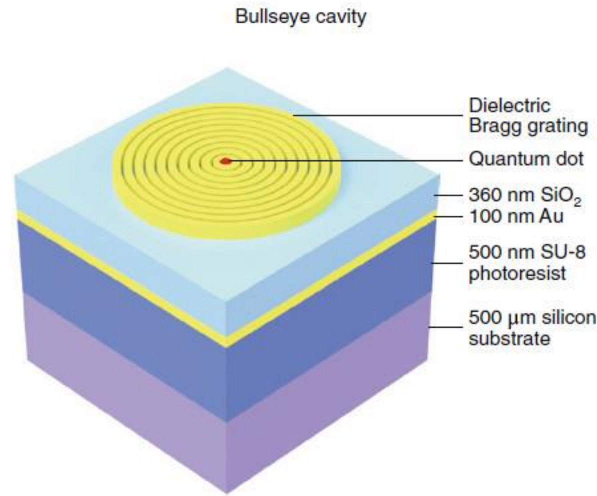

Figure 1.17. Schematic views of a bullseye cavity. QD is positioned at the antinode of the cavity with an accuracy of ~ 20 nm. For entangled photon emission a symmetric structure is desired, while an asymmetry in the structure is crucial for high-efficiency, polarized single-photon emission[10].

2. *Inhibition of the emission into modes that cannot be collected (waveguide approach)*

Instead of using the Purcell effect for enhancement of the SE into a cavity mode, the coupling over all modes of the structures using nanowires (NWs) or inverted nanotrumpets (see Figure 1.16b), except for the fundamental waveguide mode, is suppressed[3,51]. The inhibition is produced by reducing the NW diameter at the position of the quantum dot layer. Brightness values up to ≈ 75% have been measured for QD inserted in the bottom of an inverted trumpet structure[56].

The brightest QD-based source of single and entangled photons can be achieved combining both approaches – cavity approach and QD inserted in NWs (see Figure 1.16c)[3,10,17,51]. A very bright (extraction efficiency up to 80%) single-photon source based on a QD inserted in a resonant micropillar cavity has been demonstrated[10,57,58]. Also, NWs are grown using vapor-liquid-solid (VLS) mechanism on (111) substrates. As described above, additionally the use of (111) growth surface eliminates the FSS[31]. Also, selective-area growth can be used for the density and cite-controlled fabrication of NWQD[17], although this is a rather time-consuming and complicated process, compare to density controlled self-assemble DE or LDE fabrication of QDs.

3. Levering the total internal reflection (TIR) limitation (geometrical approach)

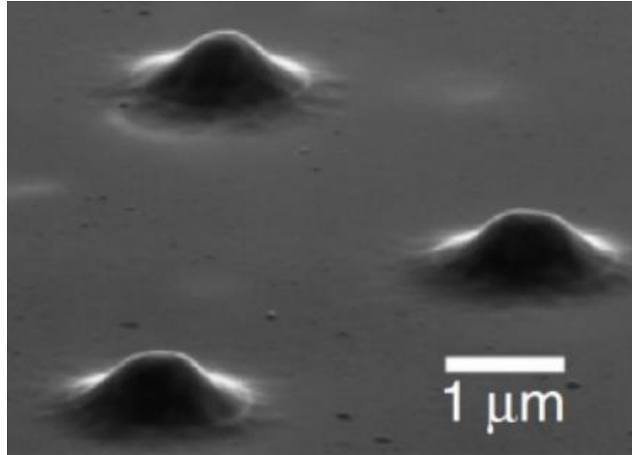

Figure 1.18. Scanning electron micrographs of etched lenses fabricated by electron-beam lithography[59].

A geometrical approach by shaping the sample surface at the emitter position can be used to increase the TIR-limited extraction efficiency[3,51]. The collection efficiency can be improved, by using different types of microlenses, placed on the sample surface under the QD position: the solid immersion lenses[60], the lenses fabricated using electron-beam lithography process[61]. Such microlenses enhance the photon-extraction efficiency to 20 – 30%. It is very difficult to combine microlenses approach with QD in cavity mode of NWs due to technological issues, but combination of microlenses with QD embedded in a planar microcavity[59] improve the photon collection efficiency of QD-based single and entangled photon sources.

There are other approaches to increase the extraction efficiency and the brightness of nanostructure-based light emitting devices like coupling with the plasmon modes of metallic microdisks[62] or coupling with dielectric resonators with very small mode volumes[63]. Nevertheless, such approaches are technologically difficult to implement together with self-assembled QDs, thus, it is not given attention to them in the given work.

From all the above, it is possible to establish that self-assembled QDs together with possibility of strain and energy tuning and approaches to increase the extraction efficiency from QDs are very promising for the fabrication of high-performance single and entangled photon emitters, which are fundamental building blocks in quantum information and in particular in quantum communication applications.

Chapter 2. Molecular Beam Epitaxy

The term "*epitaxy*" is composed of the Greek words and used for the growth of a crystalline layer upon (*ἐπί*) a crystalline substrate, where the crystalline orientation of the substrate imposes an order (*τάξις*) on the orientation of the deposited layer. When epitaxial layers are grown on the substrate or a film of the same material, it is called homoepitaxy. In the case of deposition of material different from the substrate or a film, it is called heteroepitaxy. The progress of epitaxial growth techniques has become one of the most important achievements in the production of semiconductor electronic and photonic devices. Among different epitaxial growth techniques, Molecular Beam Epitaxy (MBE) is an extremely flexible thin-film growth technology for a wide range of materials and compositions with control of thickness at atomic size level. In fact, MBE is a condensation of atoms from molecular beams directed to crystalline substrate in ultra-high vacuum (UHV) environment (vacuum level below 10^{-9} Torr before material deposition). Control of the growth conditions (substrate temperature and material fluxes) permits to obtain high-quality ultrathin epitaxial layers with sharp composition change in the interfaces. In Chapter 2 an overview of the history of molecular beam epitaxy, growth processes during epitaxial growth, and the main *in situ* monitor technique – RHEED are presented.

2.1. Historical excursion into the MBE technology

More than 60 years after the publication of pioneering work of K. G. Günther[64], his proposed "three temperature method"[65] can be considered as an origin of MBE. His great and simple idea is to use different temperatures for substrate, group III and V atom sources, permitting an independent control of their vapor pressures, in order to grow high-quality III-V semiconductor compounds. Further epitaxial technique developments have been focused in two different approaches. The first one, the so-called hot-wall technique, is related to the deposition at close to thermodynamic equilibrium conditions and allows relatively high growth rates. The second approach is cold-wall technique in UHV environment, carried out at far from thermodynamic equilibrium. This is the MBE technique, adopted and developed from "three temperature method".

One of the first work, using the above-mentioned method, was carried out by J. E. Davey and T. Pankey[66]. They studied the crystalline quality of epitaxial GaAs films deposited at different temperature on GaAs and Ge single-crystal substrates.

Nevertheless, the first who used a term "molecular beam" were J. R. Arthur in his works concerning the measurements of sticking coefficients of Ga and As_2 on GaAs{111} surfaces[67], the growth of epitaxial GaAs, GaP, and $GaAs_xP_{1-x}$ films from molecular beams of Ga, As_2 and P_2[68], and A. Y. Cho, who observed reconstructed surface structures of homoepitaxial GaAs on different

GaAs surfaces by high-energy electron diffraction system[69–71]. A few years later a lot of studies confirmed MBE as a powerful tool for the epitaxial growth of high quality III-V compound semiconductor films[72].

The further development of MBE is related to progress of vacuum technology, MBE components, MBE diagnostic and analytical facilities, and, of course, the new growth approaches within MBE technology.

In the end of 1970s the modulation doping of $GaAs/Al_xGa_{1-x}As$ heterostructures[73,74] allowed a creation of a high-electron-mobility transistor (HEMT)[75] and opened a possibility to observe the fractional quantum Hall effect[76].

Also, in the beginning of 1980s the gas-source MBE or metalorganic MBE were introduced[77,78]. It was a starting point of the development of a new epitaxial technology – chemical vapor deposition (CVD) and its varieties, which opened a production of semiconductor devices to mass-market.

As well as at this time, in my opinion, a revolution development of MBE technology happened – the first observation of RHEED intensity oscillation during the growth of GaAs epilayers[79,80]. A period of oscillations corresponds precisely to the growth of a single layer. This fact predetermined a great attention to MBE due to possibility of *in situ* epitaxial growth monitoring. A description of RHEED technique is presented below in Chapter 2.4.

In the middle of 1980s a detailed study of a nucleation of three-dimensional (3D) InAs clusters on GaAs(001) substrate, depending on the growth parameters was presented[81,82]. Now, such clusters are known as Stranski-Krastanov (SK) quantum dots (QDs), because 2D-3D transition with island formation occurs during heteroepitaxy of thin films on mismatched substrates due to elastic strain relaxation. Tremendous efforts are still being spent on the formation of QDs, studying their properties, and using them in device structures. This work is no exception.

In 1986 another useful growth approach – Migration Enhanced Epitaxy (MEE) for low temperature growth of AlGaAs layers was introduced by Y. Horikoshi[83]. The method is based on alternate supply of group III and V atoms to the growth surface and makes use of the rapid migration characteristics of atoms in an arsenic-free atmosphere, in order to grow atomically flat layers even at low temperature.

And the last thing I would like to mention in this historical background is a growth technique for the fabrication of nanosize III-V semiconductor structures based on MEE approach – Droplet Epitaxy (DE), presented by N. Koguchi in the beginning of 1990s[84]. Since this method is a main

growth technique used in this work for QD fabrication, it is worth to dedicate the whole Chapter 3 for DE.

1958	Introduction of "three temperature" method[64]
1968-1970	Sophisticated processes of MBE in UHV[67–71]
1971-1975	MBE established as a powerful technique for III-V compound semiconductor films[72]
End of 1970s	Modulation-doping of $GaAs/Al_xGa_{1-x}As$ heterostructures[73–75]
Beginning of 1980s	Introduction of gas-source MBE, MOMBE[77,78]
1983	RHEED intensity oscillation during the growth of GaAs[79,80]
Middle of 1980s	SK InAs/GaAs quantum dots[81,82]
1986	Introduction of Migration Enhanced Epitaxy (MEE)[83]
Beginning of 1990s	Introduction of Droplet Epitaxy (DE)[84]

Table 2.1. Milestones in the development of III-V MBE growth.

2.2. Atomic processes in crystal growth

Molecular beam epitaxy as a vapor deposition of thin films can be considered as the simplest case of crystal growth[85]. Atomistic theory of the crystal growth includes the following elemental processes, occurring in the growth zone and illustrated in Figure 2.1:

- an adsorption (arrival) of atoms or molecules on the growth surface;
- a migration (surface diffusion) of adsorbed atoms (adatoms) on the surface;
- an incorporation of adatoms into the crystal lattice of the surface or growing monoatomic layer;
- a thermal desorption (re-evaporation) of adatoms, which don't incorporate into the crystal lattice;
- a binding of adatoms, nucleation and further growth of two-dimensional nuclei on the surface.

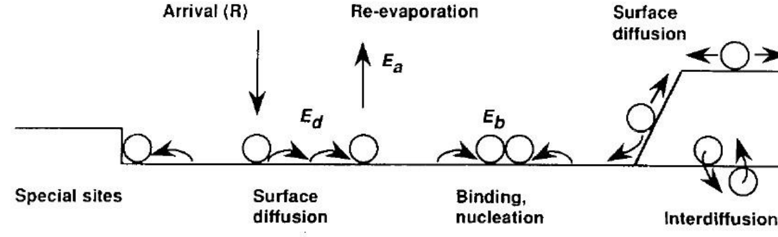

Figure 2.1. Schematic diagram of processes and characteristic energies in the nucleation and growth on surfaces[85].

Atoms arrive on the surface from the vapor at a rate *F*, or at an equivalent gas pressure *P*, such that

$$F = P / (2\pi mkT)^{1/2}, \tag{2.1}$$

where *m* is the atomic mass, *k* is a Boltzmann's constant, and *T* is the temperature of the vapor source. This creates single adsorbed atoms or molecules called adatoms or admolecules on the surface.

At high temperatures, adatoms can stay on the surface for a short time. During the time they migrate on the surface and re-evaporate. This adsorption time τ_{ad} is determined by the adsorption energy E_{ad}:

$$\tau_{ad}^{-1} = \nu_{ad} \cdot \exp\left(-E_{ad} / kT\right), \tag{2.2}$$

where ν_{ad} is an atomic vibration frequency, of the order $10^{12} - 10^{13}$ Hz, but *T* is considered now as the temperature of the surface.

At lower temperatures, as a result of adsorption and adatom migration over the surface, atoms occupy well-defined positions in the crystal lattice. The migration can be expressed as two-dimensional diffusion with diffusion coefficient *D* equals

$$D = \frac{1}{4} l^2 \nu, \tag{2.3}$$

where l^2 denotes the mean square distance covered in a single jump, ν is the jump rate. Classically, the transition path connecting the initial and final positions of the adatom single jump passes over a saddle point in energy space, and these configurations separated by the energy barrier E_D. The jump rate is then expected to follow the universal Arrhenius law for thermal activated processes,

$$\nu = \nu_0 \cdot \exp(-E_D / kT), \tag{2.4}$$

where the preexponential factor ν_0 is often referred as the attempt frequency, typically somewhat less than ν_{ad}[86]. During the growth of one monoatomic layer, which is usually one second, the

adatom can make several thousands of diffusion jumps until it reaches its final position. Thus, it is kind of self-organization of the epitaxial film.

The most preferable incorporation sites of an atomically rough surface for adatoms are kinks and edges of monoatomic steps due to presence of a larger number of dangling bonds in these sites than in other positions on the surface.

The formation of an atomic layer on a high symmetry substrate without steps or defects has to proceed through the aggregation of mobile adatoms into stable clusters, which subsequently grow by accretion. This process, described by thermodynamic nucleation theory, is presented in Chapter 3.3, because it gives a detailed account in words of nucleation of metallic droplets on the surface during droplet epitaxy.

2.3. Thin film growth modes

A formation of thin films on the substrate surface more often occurs in two stages:

- *stage of the formation of the two-dimensional nuclei*, capable of further growth,
- and *thin film growth stage*, on which nuclei grow with the formation of a continuous film.

This is how the growth process occurs according to the three classical thin film formation mechanisms, introduced by E. Bauer[87].

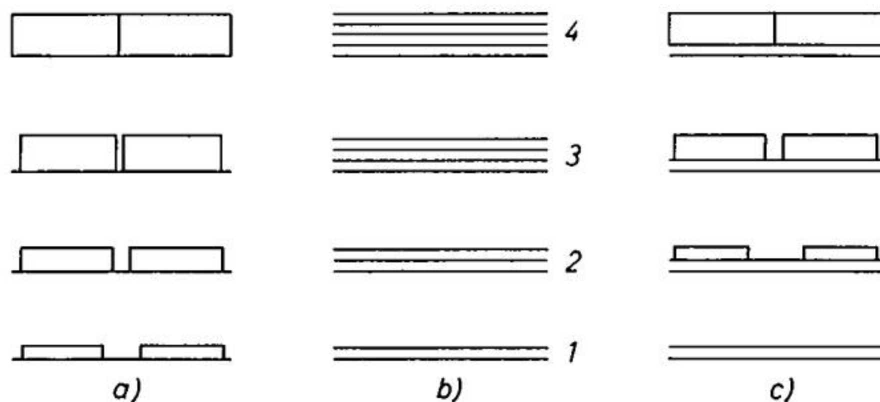

Figure 2.2. The three epitaxial growth mechanisms close to thermodynamic equilibrium: (a) Volmer–Weber growth mode, (b) Frank – van-der-Merwe growth mode and (c) Stranski – Krastanov growth mode[87].

Different growth mechanisms may be distinguished according to the balance between the surface free energy of the substrate-vacuum interface γ_S, the surface free energy of the epitaxial film-vacuum interface γ_F, and the surface free energy of the substrate-film interface γ_{SF}.

For the first case, when

$$\gamma_S < \gamma_F + \gamma_{SF} \tag{2.5}$$

the atoms of deposited material are more strongly bounded to each other, than to substrate. The energy balance requires the formation of three-dimensional nuclei isolated from each other and further growth of these nuclei into continuous film. This mechanism is named *Volmer–Weber* growth mode (see Figure 2.2a). Nuclei appear and grow when the surface coverage is much less than necessary for the formation of a single monolayer. Such films become continuous at a certain thickness and have usually granular structure.

On the other hand, when

$$\gamma_S \geq \gamma_F + \gamma_{SF} \tag{2.6}$$

the energy balance requires absence of substrate surface (complete wetting of the surface). In the process of diffusion, adatoms form two-dimensional nuclei. At a certain moment, a formation of new nuclei ceases, and two-dimensional nuclei grow up to formation of a continuous monolayer. Then, a similar situation is realized on the newly grown layer. Growth goes layer by layer and the layer-by-layer growth mechanism is called *Frank – van-der-Merwe* growth mode (see Figure 2.2b). Usually, the mechanism occurs only in the case of homoepitaxy, when $\gamma_{SF} = 0$ and $\gamma_S = \gamma_F$.

In case of heteroepitaxy and large lattice mismatch between epitaxial film and the substrate more often the third growth mechanism – *Stranski – Krastanov* growth mode occurs (see Figure 2.2c). The inequality (2.6) takes place for this mechanism, but increasing elastic energy change the layer-by-layer growth mode to island growth mode after few monolayers. A spontaneous formation of three-dimensional nano-sized islands (self-assembled nanostructures) happens on the surface of a preliminary formed thin film, which called the wetting layer (WL). This growth mechanism is used as QD fabrication method for lattice-mismatched systems, for instance, Ge on Si or InAs on GaAs.

2.4. Reflection High Energy Electron Diffraction

Reflection High Energy Electron Diffraction (RHEED) is widely used, and it is very powerful *in situ* analytical tool for characterization of thin films during the MBE growth, since it is very sensitive to the surface structure and morphology.

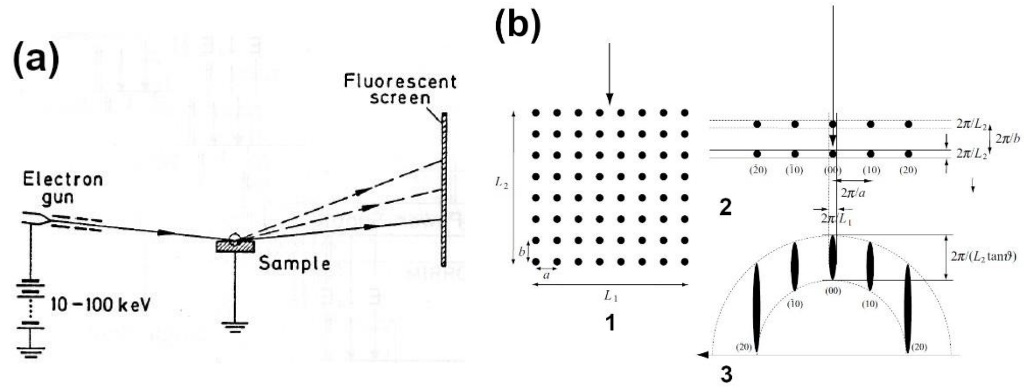

Figure 2.3. (a) Principle of RHEED system. (b) Explanation of the origin of RHEED streaks. (1) Arrangement of the two-dimensional array of lattice points. The finite sizes, L_1 and L_2, of the lattice are perpendicular and parallel to the incident direction, respectively. The incident direction is indicated by the arrow. (2) Reciprocal lattice for the arrangement in (1). (3) RHEED construction for (b); the lengths of the streaks depend on the glancing angle of incidence, ϑ[88].

RHEED systems are simple to implement into MBE chamber, requiring at the minimum only an electron gun and phosphorous fluorescent screen (see Figure 2.3a). In RHEED, an electron beam, at an energy usually between 10 and 20 keV for epitaxial growth systems (some RHEED systems are employed at electron energies as high as 100 keV), is incident on a crystal surface at a grazing angle of a few degrees. At the surface there is a scattering process in which there can be energy loss. Diffracted beams leave the crystal, also near grazing incidence, and strike a detector. This special geometry provides a small penetration depth, owing to the interaction between incident electrons and atoms, RHEED is primarily sensitive to the atomic structure of the first few planes of a crystal lattice.

The typical RHEED pattern is a streak pattern of well-ordered two-dimensional surface (see Figure 2.3b). Due to the high energy of electron beam, the origin of diffraction patterns, especially RHEED streaks, is easy to understand using approximation of kinematic diffraction theory and Ewald sphere construction.

From kinematic diffraction theory, energy and momentum conservation give the requirements:

$$\left|\vec{k}'\right| = \left|\vec{k}\right|, \tag{2.7}$$

$$\vec{k}' - \vec{k} = \vec{G}, \tag{2.8}$$

where $\vec{k}$ and $\vec{k}'$ are the incident and scattering electron wave vectors, respectively, and $\vec{G}$ is a vector of reciprocal lattice. The energy conservation requires that the magnitude of the final scattering wave vector of electron is constant and equals to the magnitude of the incident electron wave vector. Therefore, all final scattering wave vector construct a sphere, called the Ewald sphere (see Figure 2.4a). The momentum conservation determines Bragg spots, where the Ewald sphere intersects the reciprocal lattice points, which means that diffraction conditions are allowed[88] (see Figure 2.4b).

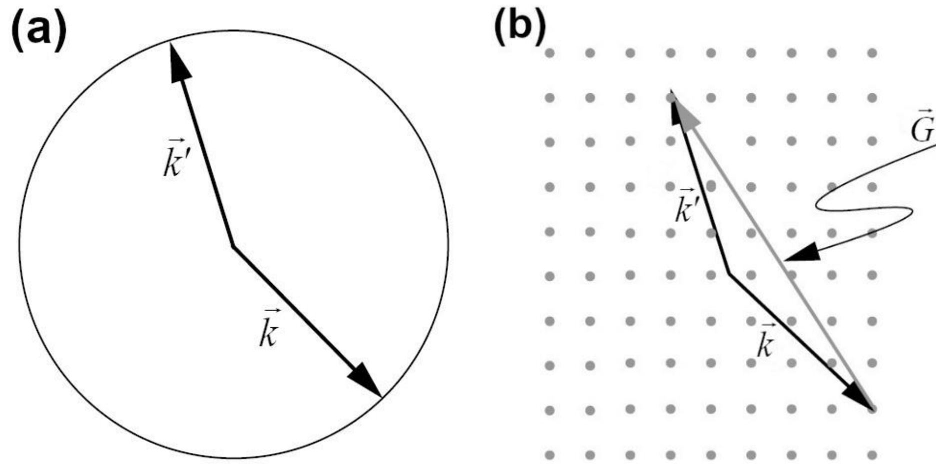

Figure 2.4. (a) The Ewald sphere is determined by the conservation of energy. (b) Conservation of momentum to within a reciprocal lattice vector[88].

In case of two-dimensional lattice, the diffraction condition for the Ewald sphere construction becomes

$$\vec{k}'_{\parallel} - \vec{k}_{\parallel} = \vec{G}_{\parallel}, \tag{2.9}$$

i.e. the difference in the parallel components of the wave vectors must equal a surface reciprocal lattice vector, $\vec{G}_{\parallel}$, and energy must be conserved. Is it possible to construct a set of parallel rods, which are normal to the surface and intersect the surface at coordinates that, with respect to an origin, correspond to the two-dimensional reciprocal lattice vectors $\vec{G}_{\parallel}$. Therefore, points, where the Ewald sphere intersects the rods, satisfy the diffraction condition (2.9)[88] (see Figure 2.5).

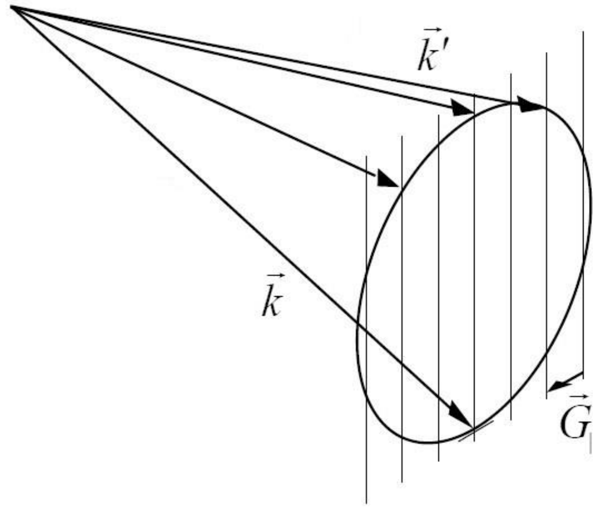

Figure 2.5. Example of the Ewald construction for a surface mesh. The reciprocal lattice for the surface is a family of parallel rods. The separation vector of the rods is $\vec{G}_{||}$. The intersection of the rods and the Ewald sphere conserves both energy and parallel momentum. The intersection of the Ewald sphere and the single plane of the rods, shown, is a circle[88].

The radius of the Ewald sphere equals the magnitude of the electron wave vector, which as de Broglie's wave vector depends on the energy as

$$\left|\vec{k}\right| = \frac{2\pi}{\lambda} = 2\pi\sqrt{\frac{2m_e E}{h}} \ . \tag{2.10}$$

Since, the electron energy exploiting in RHEED is 10 – 20 keV, the Ewald sphere radius is larger than separation distance $\vec{G}_{||}$ between the rods. Also, the finite size of two-dimensional lattice, thermal vibrations and lattice imperfections give the rods a finite non-zero thickness in reciprocal space. Finally, these facts lead to the intersection of the Ewald sphere with the rods not in separate points, but in streaks (see Figure 2.6).

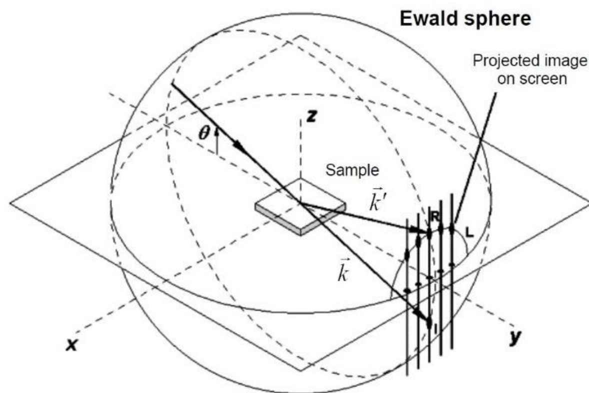

Figure 2.6. The origin of RHEED streak pattern of two-dimensional crystalline surface.

Among different applications of the RHEED technique, the first one, I would like to mention, is the possibility to measure the growth rate. It is based on the RHEED intensity oscillations of specular beam[79,80] (see Figure 2.7a). A period of oscillations corresponds precisely to the growth of a single layer. In some cases, for instance, during the epitaxial growth of $Al_xGa_{1-x}As$ layers, the period of oscillations can be used to determine the composition, if the growth rate of one species is known.

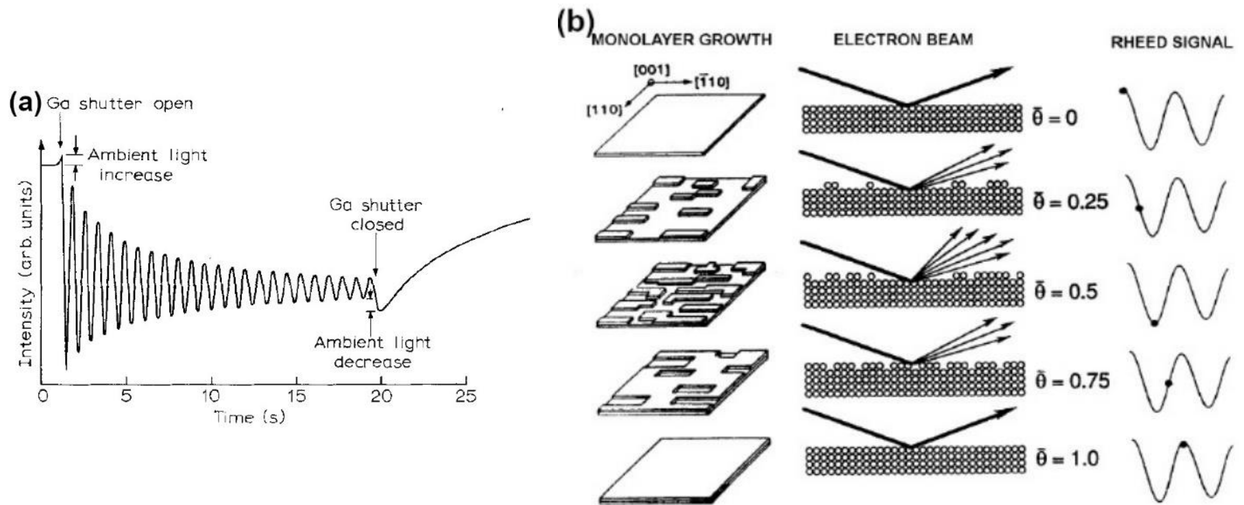

Figure 2.7. (a) Intensity oscillations of the specular beam in the RHEED pattern from a GaAs(001) – 2×4 reconstructed surface, [110] azimuth. The period exactly corresponds to the inverse of the growth rate of a single Ga+As layer and the amplitude gradually decreases. The marked inflections at the beginning and end of growth result from ambient light change as the shutters are opened and closed[79]. (b) The representation of the formation of a single complete layer and its correspondence with RHEED intensity signal.

RHEED intensity oscillations are realized only at layer-by-layer growth mode. For instance, an absence of oscillations can be related to "step-flow" growth mode on vicinal surfaces, which was used for surface diffusion measurements[89].

At layer-by-layer growth, RHEED intensity oscillations correspond to a periodic change in surface roughness. A qualitive picture of the origin of oscillations is illustrated in Figure 2.7b. A maximum intensity of specular beam is observed from an atomically smooth surface. As a result of the formation of two-dimensional islands, the intensity decreases, due to the scattering of electron beam by atomic steps. The intensity decreases until the surface coverage reaches half monolayer ($\Theta = 0.5$), then the intensity begins to increase again. The increase in the intensity is associated with the increase in surface smoothness due to coalescence of two-dimensional islands. The intensity is close to maximum (initial) value, when the surface again becomes atomically smooth ($\Theta = 1$). Such periodic cycle of the intensity is repeating many times during the epitaxial film growth. That's why no oscillations are observed in case of "step-flow" growth mode, since there is not a periodic change in the film surface roughness. The intensity damping is related to the

surface roughness evolution and the start of the growth of subsequent epitaxial layers before a completion of previous ones.

Another application of the RHEED technique is the possibility to distinguish between different crystalline states of the surface. The RHEED pattern of a single-crystalline surface is circular array of elongated spots or streaks, as described above. From polycrystalline structure the Debye-Scherrer rings are observed, corresponding to different crystallographic planes, present in a polycrystalline material. RHEED of an amorphous surface (for instance, an oxide layer) or liquid materials, in which, like in the amorphous solids, there is not a long-term crystalline order (for instance, Ga liquid droplets on GaAs surface), is diffuse background or halo pattern. It can be used for a substrate temperature calibration. For instance, a good reproducibility of the temperature for thermal oxide desorption of GaAs substrates and appearance of RHEED pattern from single-crystalline surface is observed at 580 °C during the heating with constant rate (~ 30 °C/min)[90].

Also, RHEED is useful for Stranski-Krastanov growth mode analysis. As mentioned above in Chapter 2.3, during the heteroepitaxial growth of a film with large lattice mismatch compare to substrate material, SK growth mechanism occurs. After a certain thickness, 3D islands self-assembly on the surface of the WL. A two-dimensional growth of the WL is characterized by the RHEED streak pattern. And an appearance of 3D islands is determined by the bright diffraction reflexes in the form of spots, which appear due to the diffraction through the volume of the islands[91]. Of course, RHEED spotty pattern is observed not only at SK island formation, but at any 3D formation, for instance, a quantum dot fabrication by the droplet epitaxy. Nevertheless, using RHEED it is possible to determine the WL thickness, or it is more correct to say the determination of the critical thickness of the transition from two-dimensional to three-dimensional (2D-3D) growth by a sharp change in the intensity of spotty reflexes[92,93].

RHEED analysis of spotty pattern from 3D islands can help in understanding the shape of the islands. An appearance of the so-called “chevrons” suggests a presence of the specific facets of the islands[94]. By the measuring the “chevron” angle, it is possible to determine the crystallographic planes corresponding to the facets.

And the last, I would like to emphasize, it is the observation of the surface reconstructions of the flat surfaces by RHEED. The periodicity and the distance between RHEED streaks give the information about an atom order at the sample surface in the direction perpendicular to electron beam. Observation of RHEED pattern in different crystallographic directions give an almost complete picture of surface reconstruction – the process by which atoms at the surface of a crystal assume a different structure than that of the bulk, in order to minimize a surface energy. Surface

reconstruction monitoring can help in the *in situ* control of the growth conditions, in order to decrease a segregation and the adsorption of atoms of complex compounds[93]. Or, in case of the droplet epitaxy, it can help in the choice of reconstructed surface for the subsequent droplet deposition. For instance, the reconstructions of GaAs(001) surface are characterized by a different ratio between Ga and As atoms on the surface[95].

Hence, considering only few applications of RHEED, it is possible to confirm that RHEED system is an essential part of MBE, which gives a necessary *in situ* control of the growth conditions, in order to produce high-quality semiconductor materials.

Chapter 3. Droplet epitaxy

Droplet epitaxy (DE) is a flexible growth method, performed in a molecular beam epitaxy (MBE) environment, which allows to self-assemble shape engineered nanostructures. The concept of DE results from the migration enhanced epitaxy (MEE) method, where alternate supply of group III and V atoms to the growth surface is used for the growth of atomically flat layers even at low temperature[83,96].

A new growth method for III-V microcrystals was firstly proposed by N. Koguchi and co-workers in the beginning of 1990s[84,97] and the term "droplet epitaxy" was introduced in 1993[98]. This technique is well established for the III-V nanostructure fabrication[99]. The fabrication process consists of two stages. Group III liquid metal droplets are grown on the surface, followed by crystallization and transformation into semiconductor nanostructures by annealing in group V atmosphere.

The main advantage of DE is the possibility to fabricate semiconductor quantum dots (QDs) in lattice-matched systems, for instance, GaAs/AlGaAs QDs[1,99], compared to common growth technique for strain-driven QD fabrication – the Stranski-Krastanov (SK) growth mode, at which 3D islands of the growth material appear on the substrate surface with different lattice constant due to elastic strain relaxation.

In this Chapter, I would like to discuss two stages of DE process and related control of nanostructure properties.

3.1. Droplet deposition process

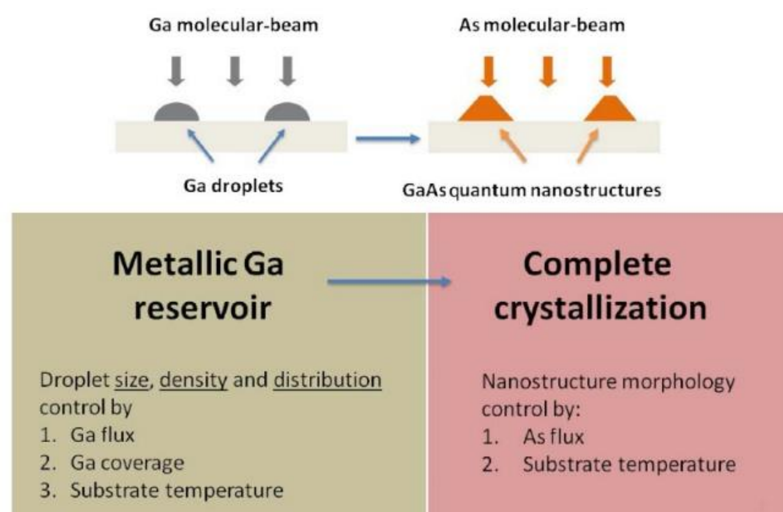

Figure 3.1. Schematics of the DE growth procedure in the case of GaAs nanostructures. Left: Ga supply step. Right: As supply step[99].

The first step of DE is the droplet nucleation. On this step it is possible to control the density, the size, and the distribution of droplets just by controlling the substrate temperature, the flux rate, and the amount of material supplied on the growth surface. The fundamental achievement of DE is the independent control of the density and the size of droplets.

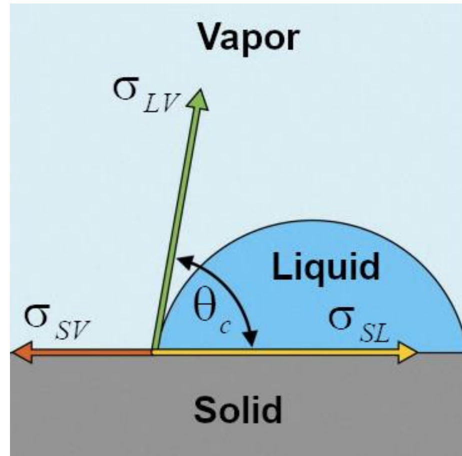

Figure 3.2. Schematic representation of the Young's equation.

The liquid phase of group III material can be obtained in a wide temperature range due to relatively low melting point of these materials (29.76 °C for gallium and 156.6 °C for indium). The liquid droplet formation on the solid surface is related to presence of surface tension σ of a liquid. Surface tension can be represented in a term of the force per unit length or in a term of the surface energy per unit area. The contact angle (the angle, conventionally measured through the liquid, where a liquid–vapor interface meets a solid surface) can be calculated using the Young's equation[100]:

$$\cos\theta_c = \frac{\sigma_{SV} - \sigma_{SL}}{\sigma_{LV}}, \tag{3.1}$$

where θ_c is the equilibrium contact angle, σ_{SV}, σ_{SL}, and σ_{LV} are surface tensions of the solid–vapor interface, the solid–liquid interface, and the liquid–vapor interface, respectively. The Young's equation arises from the consideration of a thermodynamic equilibrium between the three phases (see Figure 3.2). Therefore, the contact angle of the liquid metallic droplets on different substrates can be calculated using this simple consideration or vice versa, measuring the contact angle it is possible to estimate the surface tension[100,101].

3.2. Droplet density dependence on a deposition temperature and a flux rate

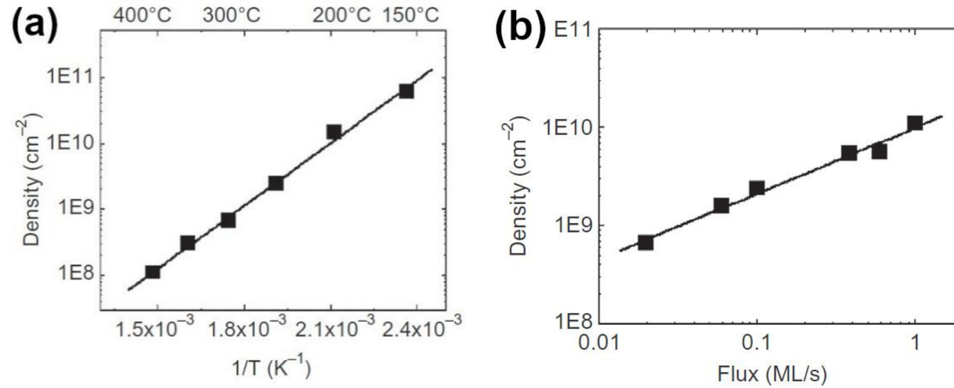

Figure 3.3. (a) Temperature dependence of the Ga droplets density at constant Ga flux (0.02 monolayer/s (ML/s)). (b) Droplet density dependence on Ga molecular beam flux at constant temperature (T = 300 °C). The density is obtained from large area AFM scans. All the experiments are carried out on a As-terminated GaAs(001)[99].

An important characteristic of DE is possibility to control droplet density over a wide range. The density is strongly dependent on the substrate temperature. In Figure 3.3a the temperature dependence of Ga droplets, nucleated on As-terminated (c(4×4) reconstruction) surface of GaAs(001), at constant Ga flux. The droplet density increases from 1×10^{8} to 1×10^{11} cm^{-2}, just decreasing the deposition temperature from 400 to 150 °C[99]. The density dependence nicely follows an Arrhenius law, suggesting the thermal activation nature of the nucleation process.

Also, the droplet density depends on the flux rate (see Figure 3.3b). The density exhibits a power law dependence on the flux and varies over a narrower range than by controlling the deposition temperature.

The droplet density dependence implies that the size of droplets depends on the amount of material deposited on the substrate at constant flux and constant deposition temperature. Therefore, DE permits an independent control of the density and the size of droplets, and subsequent nanostructures formed from the droplets.

3.3. Classical nucleation theory

As mentioned above, the droplet density dependence on the deposition temperature suggest the thermal activation nature of the nucleation process. The atomistic nucleation theory, developed by J. A. Venables[85,102], predicts such exponential dependence on the temperature, but, also, power law dependence on the flux rate.

The central object of this theory is the *critical nucleus*, which defines the free energy barrier that has to be surmounted to reach the stable phase.

The classical approach to nucleation kinetics starts from balance or rate equations for the areal concentrations n_s of clusters consisting of s atoms; n_1 is the adatom density, n_2 the density of

dimers, and so on. Only adatoms are considered as mobile species (the mobility of larger clusters is negligibly small), therefore clusters grow solely by aggregation of single adatoms. Defining Γ_s to be the net rate at which s+1-clusters form from s-clusters, we have for $s \geq 2$

$$\frac{dn_s}{dt} = \Gamma_{s-1} - \Gamma_s . \tag{3.2}$$

The net formation rates Γ_s can be written as

$$\Gamma_s = \sigma_s D n_1 n_s - \gamma_{s+1} n_{s+1} , \tag{3.3}$$

where γ_s is the rate at which adatoms detach from an s-cluster and the dimensionless capture number σ_s accounts for the propensity of an s-cluster to absorb an adatom. D is the adatom surface diffusion coefficient. If desorption from the surface can be neglected (the *complete condensation limit*), adatoms are lost only through dimer formation and capture at larger clusters, and the adatom rate equation reads

$$\frac{dn_1}{dt} = F - 2\Gamma_1 - \sum_{s\geq 2} \Gamma_s . \tag{3.4}$$

The flux rate F is defined as the number of atoms deposited per unit time and surface area.

Now, it is possible to postulate the difference between stable and unstable nucleus or clusters. Stable clusters of sizes $s \geq i+1$ are assumed not to decay, i.e. $\gamma_s = 0$ for $s > i$, while the detachment of adatoms from unstable clusters with $s \leq i$ occurs sufficiently rapidly to establish thermodynamic equilibrium between the different cluster size populations.

The total density N of stable clusters, also referred to as islands (or in our case droplets), is introduced through

$$N = \sum_{s=i+1}^{\infty} n_s . \tag{3.5}$$

The nucleation rate – the time derivative of the stable clusters total density can be obtained by summing (3.2) from $s = i+1$ to infinity:

$$\begin{aligned} \frac{dN}{dt} = \frac{d}{dt}\left(\sum_{s=i+1}^{\infty} n_s\right) = \sum_{s=i+1}^{\infty} \frac{d}{dt}(n_s) = \sum_{s=i+1}^{\infty} (\Gamma_{s-1} - \Gamma_s) = \\ \sum_{s=i+1}^{\infty} \left[\sigma_{s-1} D n_1 n_{s-1} - \gamma_s n_s - \sigma_s D n_1 n_s + \gamma_{s+1} n_{s+1}\right]. \end{aligned} \tag{3.6}$$

Taking into account that $\gamma_s = 0$ for $s > i$,

$$\frac{dN}{dt} = \sigma_i D n_1 n_i . \tag{3.7}$$

The assumption of thermal equilibrium among unstable clusters implies that the net formation rates Γ_s vanish for $1 \le s \le i-1$, and induces the detailed balance relations (also known as the Walton relation)

$$\Omega n_s = (\Omega n_1)^s \exp(E_s / k_B T) \tag{3.8}$$

between the unstable cluster concentrations and the adatom concentration. Here Ω denotes the area of an adsorption site (for instance, $\Omega = a^2$ for face-centered cubic (FCC) crystal (001) surface, where a is a lattice constant). Ωn_s is a probability that an adsorption site is occupied by an s-cluster. This is equated to the probability $(\Omega n_1)^s$ of finding s independent adatoms at adjacent sites, enhanced by the Boltzmann factor containing the cluster binding energy E_s which is gained in forming the s-cluster. Equivalently, E_s is the energy needed to disperse the cluster into single adatoms; note that $E_1 = 0$.

To complete the description, the rate equation for n_1 is simplified by introducing the average capture number for stable clusters

$$\bar{\sigma} = N^{-1} \sum_{s=i+1}^{\infty} n_s \sigma_s . \tag{3.9}$$

Finally, the equation (3.4) can be rewritten as

$$\begin{gathered}\frac{dn_1}{dt} = F - 2\Gamma_1 - \sum_{s\ge 2} \Gamma_s = F - \sum_{s=i+1}^{\infty} \Gamma_s = F - \sigma_i D n_1 n_i - \sum_{s=i+1}^{\infty} \sigma_s D n_1 n_s = \\ F - \sigma_i D n_1 n_i - \bar{\sigma} D n_1 N.\end{gathered} \tag{3.10}$$

Together (3.7), (3.8) and (3.10) form a closed set of equations from which the island (droplets) and adatom densities can be computed[86].

Considering *steady state nucleation regime*, when the first and last terms on the right hand side of (3.10) balance completely, and the adatom density is determined by the island density through

$$n_1 \approx \frac{F}{D\bar{\sigma}N} . \tag{3.11}$$

Inserting this into (3.7) and (3.8)

$$\frac{dN}{dt} = \sigma_i D n_1 n_i = \sigma_i D n_1 \left(n_1\right)^i \exp\left(E_i/_{kT}\right) = \sigma_i D \left(\frac{F}{\bar{\sigma} DN}\right)^{i+1} \exp\left(E_i/_{kT}\right). \quad (3.12)$$

Expressing flux rate F through the total coverage Θ as $F = \Theta/t$, Equation (3.12) can be reduced to an integration expression with separated variables:

$$N^{i+1} dN = \frac{\sigma_i}{\bar{\sigma}^{i+1}} \frac{\Theta^{i+1}}{D^i} \exp\left(E_i/_{kT}\right) \frac{dt}{t^{i+1}}. \quad (3.13)$$

An integration of (3.13) leads to

$$\frac{N^{i+2}}{i+2} + C_1 = \frac{\sigma_i}{\bar{\sigma}^{i+1}} \frac{\Theta}{D^i}^{i+1} \exp\left(E_i/_{kT}\right)\left(-\frac{1}{i}\right)\frac{1}{t^i} + C_2, \quad (3.14)$$

which finally gives an expression for the total density of stable clusters:

$$N \approx \left(F/_D\right)^{\frac{i}{i+2}} \exp\left[\frac{E_i}{(i+2)kT}\right] \approx F^{\frac{i}{i+2}} \cdot \exp\left[\frac{E_i + i \cdot E_d}{(i+2)kT}\right]. \quad (3.15)$$

Therefore, from classical nucleation theory[85,86,102] the droplet density depends on the deposition temperature T and a flux rate F by scaling law:

$$N(F,T) \propto F^p \exp\left(E_a/_{kT}\right), \quad (3.16)$$

where p is a function of a critical cluster size i ($p=i/(i+2)$) and E_a, the droplet density activation energy, is a combination of a diffusion activation energy E_d and a nucleation energy of the critical cluster E_i ($E_a = pE_d + pE_i/i$).

3.4. Capture zone approach

From the previous section it became known that, in order to find characteristic parameters of the droplet nucleation – the critical cluster size i and the nucleation energy of the critical cluster E_i, it is necessary to carry out both measurements, the droplet density dependence on the deposition temperature and the flux rate. Especially, to obtain the critical cluster size, it is necessary to measure the droplet density as a function of the deposition rate at given conditions (the main is the deposition temperature).

Another approach for an estimation of the critical cluster size can be gained from the analysis of the capture zone (CZ) distribution[103,104] of the droplets. CZs can be determined from Voronoi cells, a particular case of a surface tessellation where, given a set of centers (in our case the droplets),

the space is divided according to their "area of influence"[105]. Voronoi tessellation is similar to Wigner-Seitz cell construction for primitive cell of the crystal lattice (see Figure 3.4).

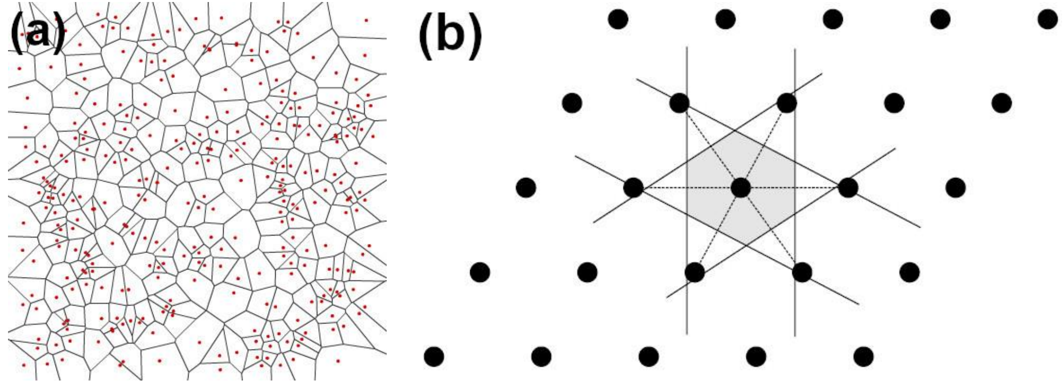

Figure 3.4. (a) An example of Voronoi tessellation. (b) Construction of a two-dimensional Wigner–Seitz cell.

The capture zone distribution (CZD) is then the statistical distribution of the sizes (areas) of the CZs. The predicted analytical form of CZD, that is the normalized area distribution of the Voronoi cells, coincides with generalized Wigner distribution (GWD), proposed by Wigner for the nearest-neighbor spacing distribution[103,104,106]:

$$P_\beta(s) = a_\beta \cdot s^\beta \cdot \exp\left(-b_\beta s^2\right), \tag{3.17}$$

where s is the CZ area divided by its average value, $a_\beta = \Gamma\left(\frac{\beta+2}{2}\right)^{\beta+1} \Big/ \Gamma\left(\frac{\beta+1}{2}\right)^{\beta+2}$ and $b_\beta = \left[\Gamma\left(\frac{\beta+2}{2}\right) \Big/ \Gamma\left(\frac{\beta+1}{2}\right)\right]^2$ are the constants that assure normalization and unit mean conditions, respectively.

The parameter β is related to the critical cluster size i by

$$\beta = \gamma i + 1 + \gamma, \tag{3.18}$$

where γ is characteristic of the limiting process (for instance, dimensionality of the diffusion): γ = 1 for isotropic two-dimensional diffusion, γ = 2 for strongly anisotropic (1D) diffusion[104].

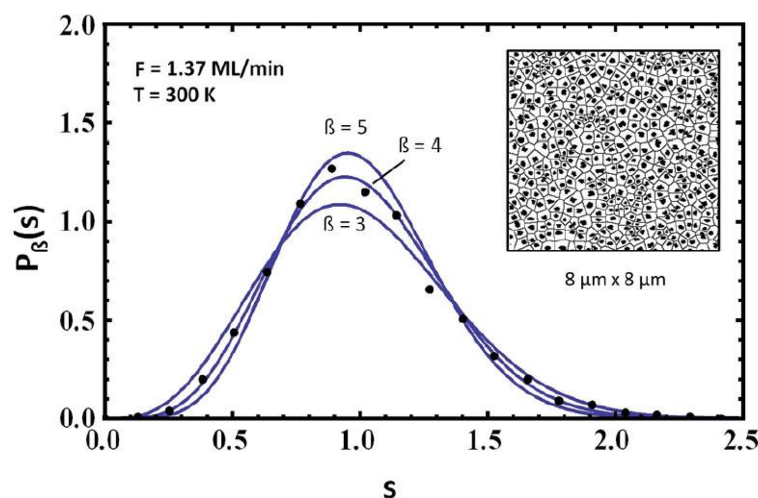

Figure 3.5. Normalized capture zone distribution (black dots) obtained by summing over 5 different AFM images of a pentacene film deposited on sputtered mica with a high deposition rate F = 1.37 ML/min at room temperature. The curves are calculated using the fit function $P_\beta(s)$. The best fit yields $\beta = 4.0 \pm 0.5$. The inset shows a representative Voronoi tessellation (8×8 μm^2)[104].

Therefore, the experimental normalized CZD can be obtained from Voronoi tessellations of AFM or scanning tunneling microscopy (STM) images and then, can be fitted by generalized Wigner distribution $P_\beta(s)$ (see Figure 3.5). Finally, the critical cluster size can be estimated by (3.18) from observed β value, taking into account the dimensionality of the diffusion.

CZD analysis provides an information about the size of the critical cluster and reflects the dimensionality of the nucleation process[103] and can be extended to any aggregation-limited process[104]. Using this approach, the critical cluster size can be directly obtained from AFM scans and compared to the value, estimated from the droplet density dependence on the flux rate.

3.5. The surface reconstruction influence

As we understood from classical nucleation theory[85,86,102], the droplet density activation energy E_a is a combination of a diffusion activation energy E_d and a nucleation energy of the critical cluster E_i. It means that the choice of a deposited material as well as the choice of the substrate material have influence on the diffusion activation energy and the binding energy, and correspondingly, on the droplet activation energy.

But not only the substrate material itself, but also the surface reconstruction affects on the abovementioned parameters, which can change the density and the size of droplets at given conditions, as well as the nucleation process.

As reported in the work, published by A. Ohtake[95], different As-rich and Ga-rich surface reconstructions are formed on the GaAs(001) surface depending on the preparation conditions. A typical surface reconstructions during DE on GaAs(001) are the As-rich c(4×4)β, (2×4), and Ga-rich (4×6)[99], which has the As coverage of 1.75 ML, 0.75 ML and 1/12 ML, respectively[95].

It means that, for instance, starting the Ga deposition on GaAs(001)-(2×4) surface, it is necessary to deposit almost 0.75 ML of gallium before the appearance of (4×6) reconstruction and subsequent formation of Ga droplets. In the other words, as long as Ga-rich surface reconstruction is not established on the surface, Ga atoms saturate the bonding to As, creating an adsorption layer of GaAs. The formation of the droplets is possible only on Ga-rich reconstruction[99]. Therefore, RHEED monitoring of surface reconstruction during droplet fabrication is very important for understanding the minimum amount of material, which should be supplied on the surface to start the droplet nucleation and the estimation of the size of droplets.

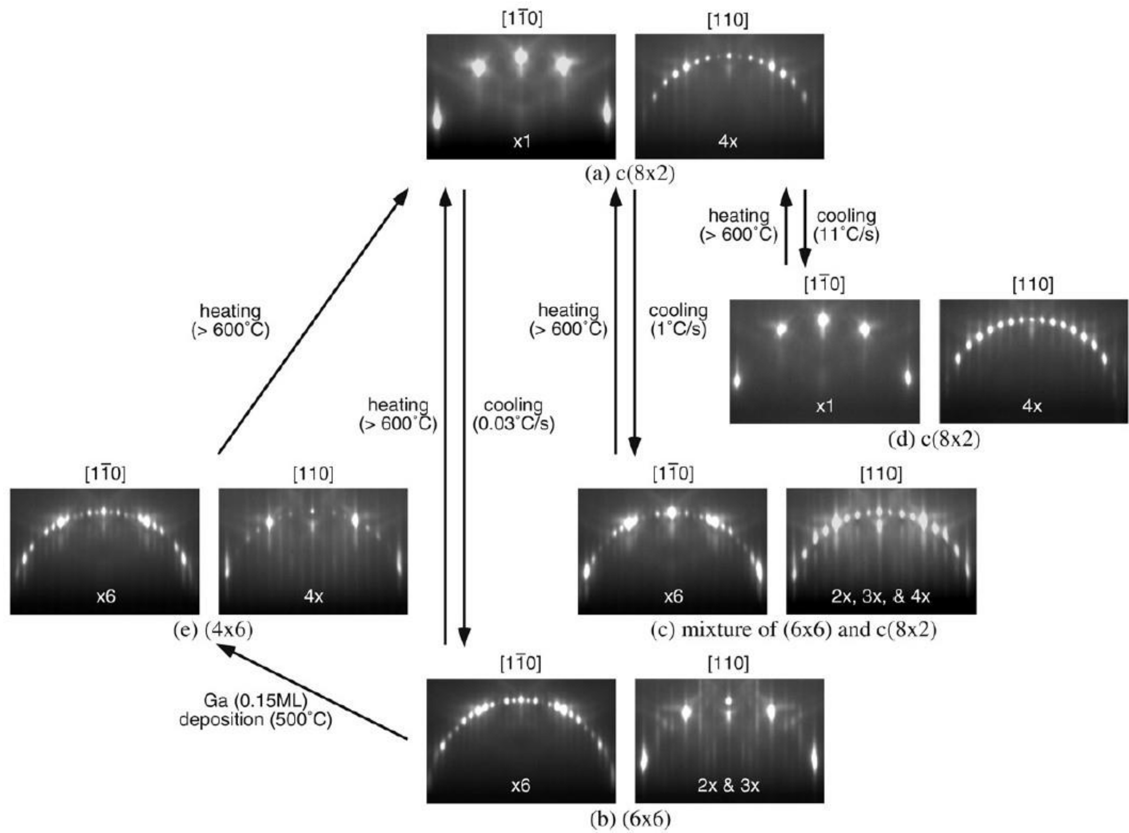

Figure 3.6. RHEED patterns observed on the Ga-rich surface reconstructions of GaAs(001)[95].

At the same time, the importance of the ultrahigh vacuum environment during droplet deposition becomes clear. The growth chamber should be depleted from the group V atoms or molecules, otherwise, a creation of the adsorption layer will continue even on Ga-rich surface reconstruction in case of Ga supply on GaAs. The typical background pressure during the droplet deposition is about 1×10^{-9} Torr.

Also, from abovementioned consideration, another advantage of DE originates. It is the possibility to control the thickness of the WL. WL is a layer of the same material as the dots, which is formed during the growth and mediates the electronic interaction between the barrier states and the localized dot states[99]. Basically, the WL configuration affects on the optical properties of QDs and the performance of QD based devices[107]. In case of SK growth mode, the WL thickness is difficult to be controlled and depends on the lattice mismatch between the epilayer and the substrate. For instance, WL is about 1.5 – 1.7 ML for InAs/GaAs heteroepitaxy[108,109]. But the DE technique allows to control the WL thickness by choosing the appropriate surface reconstruction and even gives an opportunity to grow QDs without WL formation, for instance, by starting the deposition of group III atoms on the metallic-rich surface reconstruction of AlGaAs layer.

3.6. Crystallization process

The second step of the DE is the crystallization process and transformation of liquid group III droplets into semiconductor nanostructures by annealing in group V atmosphere. On this stage, it is possible to control the shape of nanostructures by manipulation of crystallization conditions – the crystallization temperature, the flux of group V atoms or molecules and the crystallization time.

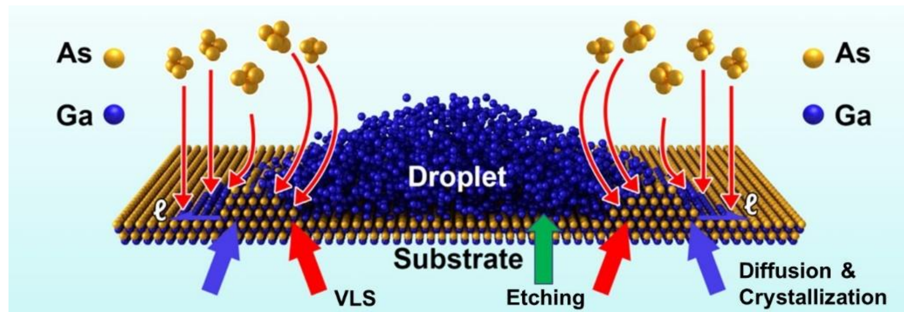

Figure 3.7. Schematic representation of three main processes during the arsenization of Ga droplet. Blue, red, and green arrows indicate places where diffusion and crystallization, VLS mechanism, the etching process, respectively, starts after irradiation of Ga droplet in As atmosphere. *l* corresponds to Ga migration length out of the original droplet size.

The final shape of nanostructures depends on the interplay between main processes during crystallization (see Figure 3.7). There are diffusion of group III atoms and their subsequent crystallization, the VLS mechanism, and the etching of the substrate underneath the droplet position. Changing the crystallization conditions, one of these processes becomes dominant.

Let us consider two extreme cases of crystallization in As atmosphere (arsenization) of Ga droplets on GaAs(001) surface. The first is the low crystallization temperature and high As flux. Both these conditions suppress the diffusion and migration of Ga adatoms from the droplets. In that case the VLS mechanism becomes dominant and the final shape of nanostructures is 3D islands. This is the origin of QD fabrication by DE. In the work of Ref.[110] the crystallization kinetics of Ga droplets

under high As flux was studied. It was shown that the crystallization starts from a ring of GaAs formed at the perimeter of the droplet and which acts as a nucleation seed for the further crystallization. During the As supply, the ring increases size at the liquid-solid interface at the expense of the metallic droplet. GaAs QD growth proceeds from the surface edge of droplets with a constant speed along ⟨111⟩ directions until the complete depletion of the Ga contained in the droplet. The schematic illustration is presented in Figure 3.8.

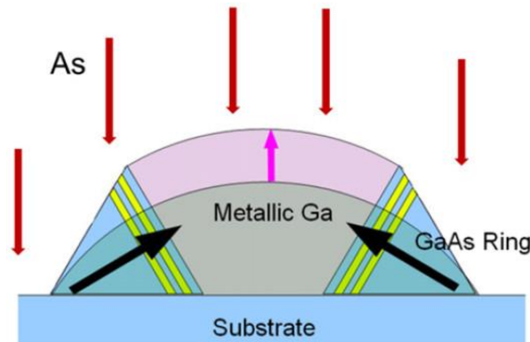

Figure 3.8. The scheme of the nanocrystal growth model during the arsenization process of Ga droplets on GaAs(001). The black arrows indicate the ⟨111⟩ directions[110].

The second opposite case is the high crystallization temperature and low As flux. The surface diffusion of Ga adatoms becomes dominant at these conditions and Ga adatoms can migrate far from the original droplet position, creating the disk- and/or the ring-shape of the GaAs nanostructures. In the work[111] a qualitative model of the DE complex nanoring structure fabrication was proposed. The triple ring structures presented in Figure 3.9a, obtained by DE growth method based on short time As supply to the Ga droplets at different substrate temperatures. Figure 3.9b shows a schematic representation of the growth model for outer ring structures. As already known, Ga droplets can nucleate only on Ga-rich surface reconstructions (Panel 1 of Figure 3.9b). Then, arsenic supply leads to a change of a surface reconstruction from Ga-rich (4×6) to As-stabilized (2×4) in the out of the droplet area. High crystallization temperature permits Ga adatoms migrate far from the droplets and from a GaAs layer on a circular area with a radius ~ $D\tau$ (Panel 2 of Figure 3.9b). D is the Ga adatom surface diffusion coefficient and τ is a characteristic migration time between arrival and adsorption of As atoms. Further arsenic supply turns the surface far from the droplet to As-rich c(4×4) reconstruction. In the border of this area Ga atoms, crystallized by excess of As, form the outer ring structure (Panel 3 of Figure 3.9b).

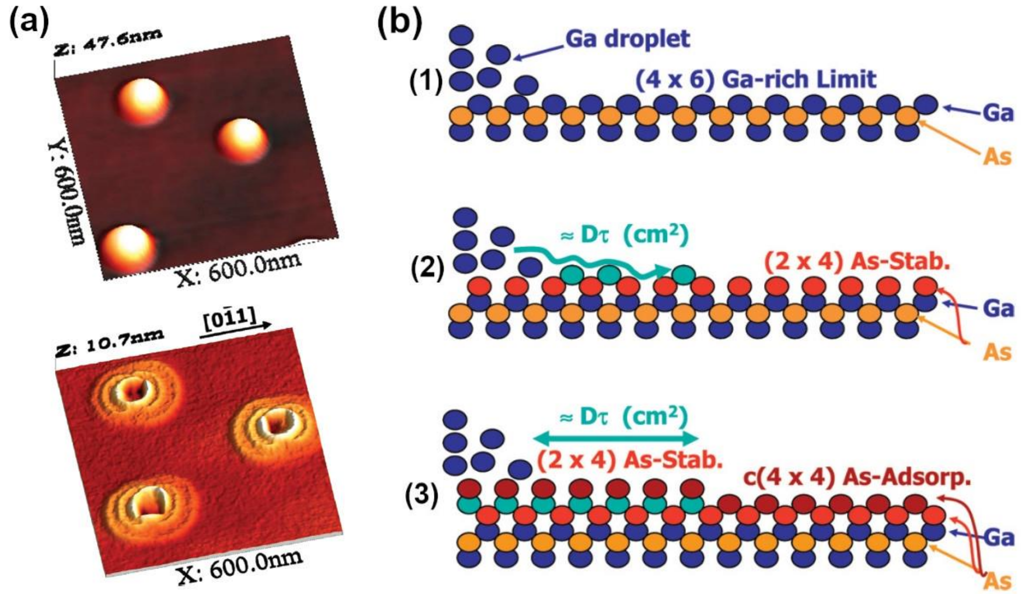

Figure 3.9. (a) Upper picture: AFM image of Ga droplets on GaAs(001); bottom picture: AFM image of multiple concentric nanoring structures after crystallization of Ga droplets on GaAs(001). (b) Schematic explanation of the proposed growth mechanism or the formation of outer rings structures. Ga droplets are formed on a Ga-rich (4×6) surface reconstruction (1). During As supply, a (2×4) surface reconstruction appears all over the substrate on the top of which the Ga atoms, coming from the droplets, can migrate covering a mean displacement area of ~Dτ (2). Far away from the droplet the surface turns to the As-rich c(4×4). The border of this area act as a pinning site for the migration of the Ga atoms (3). The detailed atomic arrangements for the different surface reconstructions are ignored for simplicity[111].

Z.Y. Zhou et al.[112] proposed a theoretical model for the ring formation. The model considers isolated droplet of radius $r_D(t)$ at time t, and writes the steady state diffusion equation for the Ga concentration outside the droplet at radial coordinate r as

$$D_{Ga}\left(\frac{1}{r}\frac{dC_{Ga}}{dr}+\frac{d^2C_{Ga}}{dr^2}\right)-k_rC_{Ga}C_{As}=0 \quad . \tag{3.19}$$

Here C_{Ga} and C_{As} are the respective Ga and As surface adatom concentrations. k_r is a reaction rate constant governing the reaction between Ga and As to form GaAs solid and D_{Ga} is the Ga diffusion coefficient. Ga evaporation was assumed negligible for the temperatures associated with DE.

The first term in (3.19) raises from consideration the diffusion from the cylinder, $\frac{d}{dr}\left(r\frac{dC}{dr}\right)=0$.

The second term is responsible for GaAs crystal formation. The same consideration can be done for As, adding additional terms related to As evaporation C_{As}/τ_{As} with the residence time τ_{As} and to As deposition flux F_{As}:

$$D_{As}\left(\frac{1}{r}\frac{dC_{As}}{dr}+\frac{d^2C_{As}}{dr^2}\right)+F_{As}-\frac{C_{As}}{\tau_{As}}-k_rC_{Ga}C_{As}=0. \tag{3.20}$$

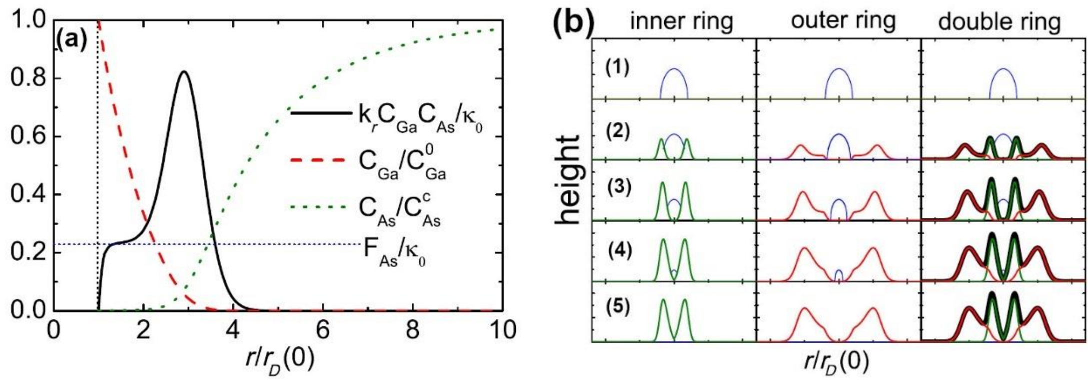

Figure 3.10. (a) Typical Ga and As adatom concentration profiles at $t = 0$ and their resulting reaction rate, which is peaked away from the droplet periphery. The vertical dashed line indicates the position of the droplet perimeter at $r = r_D(0)$. (b) Snapshots taken from a movie generated from a theoretical model of GaAs deposition during DE. The time evolution of the inner and outer ring components is shown in the first and second columns of (1) – (5), respectively. The total double ring morphology is shown in the third column as sum of these contributions. Row (1) corresponds to the initial droplet, while (5) is the final deposited GaAs height following complete disappearance of the droplet. Blue line in all panels is the droplet profile[112].

Figure 3.10a shows Ga and As concentration profiles obtained by solving (3.19) and (3.20) The Ga concentration decreases monotonically away from the droplet while the As concentration decreases towards the droplet edge. There is a peak in the GaAs deposition rate $k_r C_{Ga} C_{As}$ where the outward-diffusing Ga meets the inward-diffusing As. This reaction zone is the basic physical origin of outer quantum rings in the model. The reaction zone exhibits a structure which can be divided into four distinct regions. Starting at $C_{As} = 0$ and $k_r C_{Ga} C_{As} = 0$ at the droplet edge ($r = r_D(0)$), $k_r C_{Ga} C_{As}$ rises to a plateau. The plateau corresponds to $k_r C_{Ga} C_{As} = F_{As}$ in the Ga rich zone surrounding the droplet. Physically, all of the deposited As is reacting to form GaAs in this region and the reaction rate is limited by F_{As}. The plateau then transforms with increasing distance from the droplet into a peak where As diffusing inwards impacts the Ga-rich zone. Then outside the peak region $k_r C_{Ga} C_{As}$ falls off rapidly as we enter a Ga-free zone[112].

The model is well described the fabrication of the multiple ring structure fabrication by DE. Figure 3.10b shows the calculation of the height profiles of inner and outer ring for double-ring structure. It can be seen in the first column of Figure 3.10b that the inner ring profile gradually builds up in amplitude with time. Although GaAs deposits at a constant rate, the droplet edge spends increasingly less time at a given radial position as the droplet shrinks, producing a peak away from the droplet center. Simultaneously, GaAs deposition, of the form shown in Figure 3.10a, gradually establishes an outer ring. This is shown in the second column of Figure 3.10b. The resulting morphology is shown in the third column as a sum of inner and outer ring. It clearly exhibits the double-ring structure[112].

Additionally, this theoretical model can be used for the calculation group III adatom diffusion parameters. The measurement of Ga surface diffusion on GaAs(001)[113] and In surface diffusion on InP(001)[114] relies on the morphology determination of nano-disks that evolve, under group V supply, from nanoscale group III droplets, earlier deposited on the substrate surface. The dependence of the radius of such nano-disks on crystallization conditions gives direct access to group III adatom diffusion length[113].

Precise tuning of quantum dot size, aspect ratio, and faceting can be achieved in DE GaAs QDs self-assembly on GaAs(001) substrates[115]. DE-QDs, with volumes ranging from 10^2 to 10^5 nm^3, were obtained with a controlled aspect ratio ranging from 0.05 to 0.6 and a facet orientation angle from 10° to 55°. It is shown that the facet orientation angle depends strongly on the As flux and on the crystallization temperature. The slope of the facet increases with increasing As flux and decreasing crystallization temperature (see Figure 3.11a). An analysis of cross-sectional scanning tunneling microscopy (X-STM) images of DE GaAs/AlGaAs(001) QDs shows that the QD facets are made up of a series of steps consisting of (001) and (111) facets whose length varies depending on the facet angle (see Figure 3.11b).

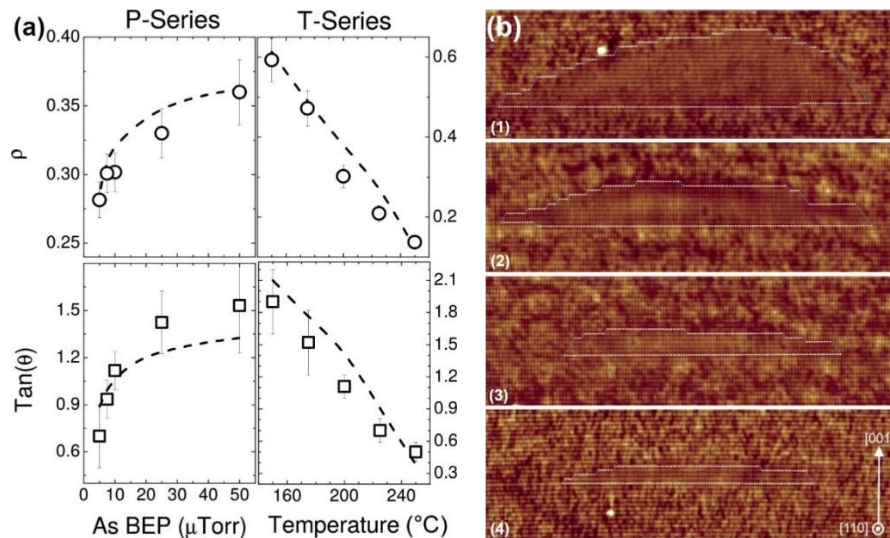

Figure 3.11. (a) Dependence, on the crystallization parameters, of the DE QD aspect ratio ρ and facet angle θ. θ is the angle between the QD facet and the substrate. Upper panels: ρ dependence on As beam equivalent pressure (BEP) and crystallization temperature. Lower panels: θ dependence on As BEP and crystallization temperature. The dashed lines indicate the theoretical prediction. (b) 53 nm×17 nm filled state topography images of DE GaAs QDs obtained by crystallization of Ga droplets after the deposition of (1) 5 ML, (2) 3 ML, (3) 2 ML, and (d) 1.5 ML of Ga. The images correspond to 2D cuts close to the center of the QDs. (001) facets are outlined in white and (111) facets are outlined in blue[115].

Therefore, an accurate selection of growth parameters and subsequent control of crystallization kinetics during DE, gives a possibility to precisely engineer the shape of nanostructures from 3D islands, 2D disks, and rings to more complex nanostructures.

3.7. Local droplet etching technique

On the domination of the etching process during the droplet crystallization is based the LDE technique. The LDE process can be divided into several stages[1,116]. The first two are the same as for DE method. There are droplet nucleation and the droplet annealing under group V flux. The difference from DE process is that the annealing step is carried out under rather low group V flux and high temperature. In case of Ga LDE on AlGaAs surface it leads to As desorption underneath the Ga droplet at high growth temperatures and Ga-rich conditions[117]. The etching occurs and nanoholes with the depth larger than 10 nm penetrate the surface. The illustration of LDE process is presented in Figure 3.12. Then, these nanoholes can be filled and capped for QD fabrication.

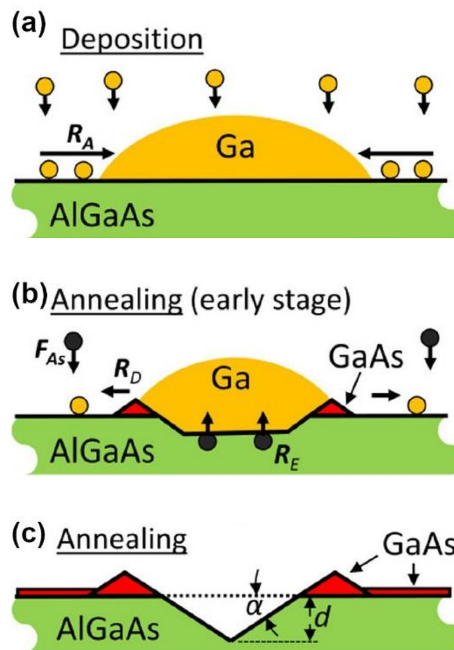

Figure 3.12. Schematic representation of the different steps of a Ga on AlGaAs droplet etching process. (a) Droplet shape establishment with increasing coverage and increase of the droplet volume by adatom attachment with rate R_A. (b) Etching and removal of substrate material by As diffusion with rate R_E and droplet material detachment with rate R_D during post-growth annealing. The detached Ga atoms crystallize a thin GaAs layer with background As of flux F_{As}. (c) Final hole with depth *d* and side-facet angle α surrounded by a GaAs wall[116].

The density of nanostructures fabricated by LDE as for DE are controlled in the droplet deposition step. But the nanohole size depends on the initial droplet size and the crystallization process. Firstly, it was established that a small As background flux (BEP is about 10^{-7} Torr) is essential for etching process[116]. If the As BEP is higher (10^{-6} – 10^{-5} Torr), no etching occurs, and droplets are crystallized into nanostructures fabricated by DE method. Also, if the As BEP is rather smaller (10^{-8} Torr), the detached adatoms will re-attach to the droplet and conserve it. Thus, the etching process is very sensitive to crystallization parameters.

The second observation is related to the crystallization of adatoms detached from the droplet. Adatoms detaching from the droplets crystallize as uniform layer surrounding the droplet

rim[116,117]. This process is very similar to quantum disk/ring formation by DE[118]. However, the depth of nanohole in the center of that ring structure can be controlled by the initial amount of droplet material and the crystallization temperature[116,119] (see Figure 3.13).

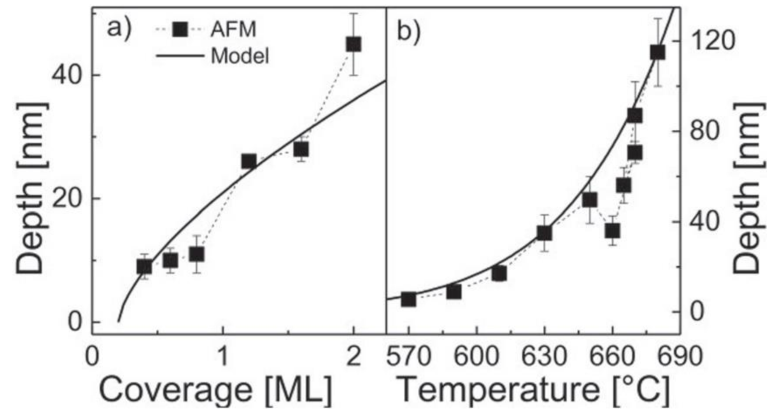

Figure 3.13. Measured and calculated depth d of Al droplet etched nanoholes. (a) Comparison of measured and calculated depth of Al-droplet-etched nanoholes as a function of the Al coverage. (b) Measured and calculated depth of Al-droplet-etched nanoholes as a function of the process temperature[116].

The main advantage of the LDE technique in contrast to DE method, especially using Al droplets, is the rather high temperature during QD fabrication (> 600 °C), which strongly improves the crystal quality of nanostructures. This fact as well as the possibility to obtain highly symmetric nanoholes on (001) surfaces allow to fabricate GaAs QDs grown on AlGaAs/GaAs(001) by Al LDE process, and such dots exhibit excellent optical properties, useful for a single photon and an entangled photon generation[30,52].

Chapter 4. Experimental setup

4.1. MBE system

All samples presented in this work have been grown using the Applied EPI-Vecco Gen II MBE system installed in L-NESS laboratory[120] in Como, Italy. The scheme of the MBE machine is presented in Figure 4.1.

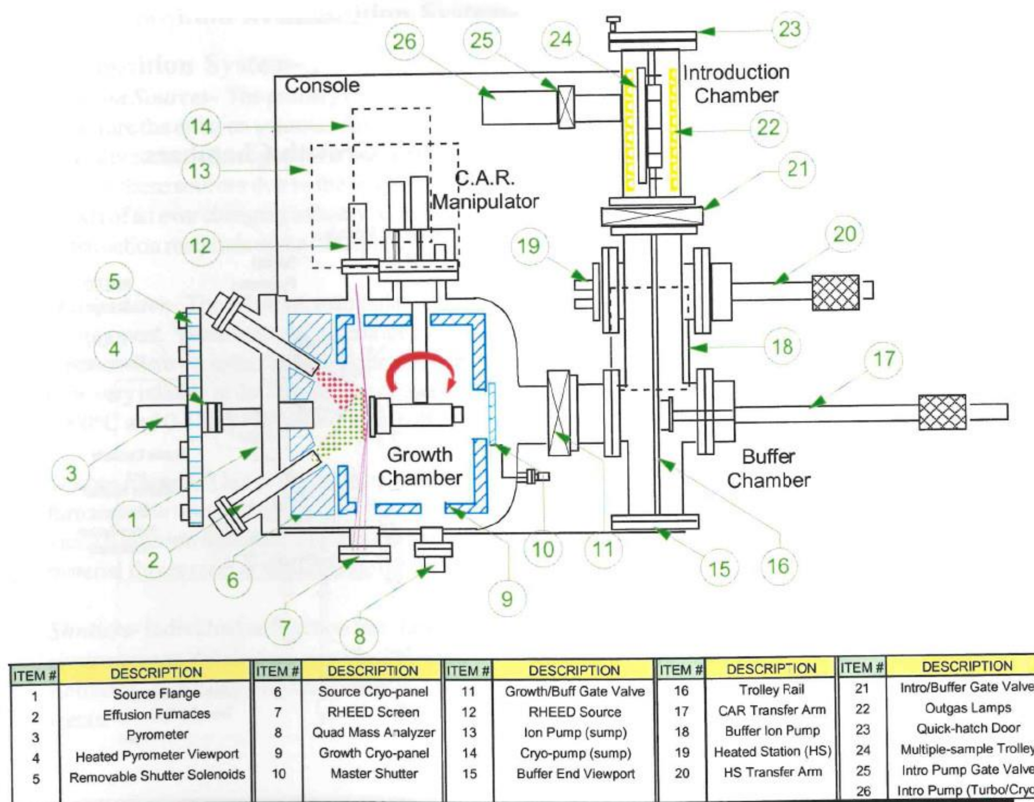

ITEM #	DESCRIPTION	ITEM #	DESCRIPTION	ITEM #	DESCRIPTION	ITEM #	DESCRIPTION	ITEM #	DESCRIPTION
1	Source Flange	6	Source Cryo-panel	11	Growth/Buff Gate Valve	16	Trolley Rail	21	Intro/Buffer Gate Valve
2	Effusion Furnaces	7	RHEED Screen	12	RHEED Source	17	CAR Transfer Arm	22	Outgas Lamps
3	Pyrometer	8	Quad Mass Analyzer	13	Ion Pump (sump)	18	Buffer Ion Pump	23	Quick-hatch Door
4	Heated Pyrometer Viewport	9	Growth Cryo-panel	14	Cryo-pump (sump)	19	Heated Station (HS)	24	Multiple-sample Trolley
5	Removable Shutter Solenoids	10	Master Shutter	15	Buffer End Viewport	20	HS Transfer Arm	25	Intro Pump Gate Valve
								26	Intro Pump (Turbo/Cryo)

Figure 4.1. Functional block diagram of the Gen II MBE system.

The MBE machine consists of three chambers separated by gate valves. The first – introduction chamber is connected to a class 100 flow-box for the preparation and loading/unloading samples and wafers. Wafers and samples are mounted on molybdenum holders and loaded on a trolley inside the intro chamber. This MBE system allows to load maximum 3-inch wafers. A heater inside the flow-box allows to mount small pieces of wafers on a special type molybdenum holder using melted indium. The vacuum in intro chamber is provided by the rotary pump and the Leybold Turbovac 361 turbomolecular pump. Also, since usually the Leybold pump is not switched off during the loading/unloading samples, intro chamber is equipped with hybrid turbomolecular pump with the diaphragm (or membrane) pump for the formation of backing vacuum. The pumps allow to reach 10^{-9} Torr. The pressure inside the chamber is monitored by the Pirani and the cold cathode gauges. To not contaminate MBE system during the loading/unloading procedure by the air, the intro chamber is connected to N_2 flow line. And to prevent the contamination of MBE

machine from the inserted molybdenum blocks with wafers and from the wall of the chamber exposed to the atmosphere pressure during the loading/unloading, intro chamber is equipped with baking system capable to reach about 200 °C.

The intro chamber is connected to the second chamber called the buffer chamber where the wafers are prepared for the growth. The trolley with sample holders can be moved from intro chamber to buffer chamber along a rail. There is a degas station to heat a single molybdenum holder up to 600 °C for thermal treatments or to desorb impurities (water mainly). Usually we heat up GaAs substrates up to 300 – 350 °C to avoid thermal desorption of the oxide layer. The vacuum in the chamber is provided by a Varian VacIon ion pump, which allows to reach the pressure of about 10^{-10} Torr. The pressure is monitored by the UHV nude Bayard-Alpert gauge connected to a Granville-Phillips 350 measurement system.

The third chamber is the main growth chamber equipped with two UHV pumps. A cold head connected to a water-cooled Helix 8200 compressor is able to reach about 10 K and works as a cryogenic pump. Also, the second Varian VacIon ion pump is installed to the growth chamber. The pressure in the growth chamber is monitored by the two UHV nude Bayard-Alpert gauge connected to a Granville-Phillips 350 measurement system. The first gauge is used to monitor the background pressure in the chamber, the second one is placed on the back side of the substrate holder and can be rotated to the growth position to measure the equivalent pressure of molecular beams of the effusion cells. Also, there is a quadrupole mass-spectrometer to monitor the elemental composition of vacuum residue and to find leaks in vacuum system.

Our MBE system is equipped with 5 effusion cells for Ga, Al, In, Si, and Be. Each effusion cell is connected to Eurotherm 900 EPC controllers. Controllers can regulate the temperature of effusion cell crucibles by reading the temperature of a thermocouple situated close to the crucible and by controlling the voltage and the current of the effusion cell filaments. Two effusion cells (for Ga and Al) have two filaments and two thermocouples for careful control of the crucible temperature to avoid accumulation of the source material at the crucible mouth and to improve the beam homogeneity. Other cells have only one filament. Si and Be can be used as dopants for III-V semiconductor materials. For arsenic, the valved cracker cell is used. It allows to fine tune the As flux by the needle valve. The As cell is also connected to Eurotherm 900 EPC controller which can regulate the temperature of the bulk zone and the cracking zone. Controlling the temperature of the cracking zone it is possible to select between As_4 or As_2 molecules (600 – 700 °C for As_4 and 900 – 1100 °C for As_2). Each cell is provided with a pneumatic shutter to open and close the material fluxes on the substrate.

The substrate holder is equipped with heating system, providing homogeneous temperature of the entire substrate surface during rotation of the substrate holder around the central axes, and the thermocouple also connected to and controlled by another Eurotherm 900 EPC controller. Additionally, the substrate temperature above 450 °C can be monitored by the optical pyrometer mounted in front of the growth chamber, also, provided with a shutter to avoid the contamination of quartz window.

The As cell and the substrate manipulator are water-cooled. Additionally, to improve the vacuum inside the growth chamber and to reduce the contamination of the samples, there are two cryo-shrouds inside the chamber, which can be filled with liquid helium.

Our MBE is equipped with a Staib RHEED instrument consisting of the electron gun with a working voltage of 13 keV, RHEED fluorescent screen, and the charge-coupled device (CCD) camera to *in situ* monitor RHEED pattern.

The cells of the MBE machine provide stable homogeneous material fluxes in a long period. Once measure the flux dependence on the crucible temperature, we can use the calibration for several months. Figure 4.2 presents Ga flux calibration measured in 6-month period by RHEED intensity oscillation technique, described in the Chapter 2.4.

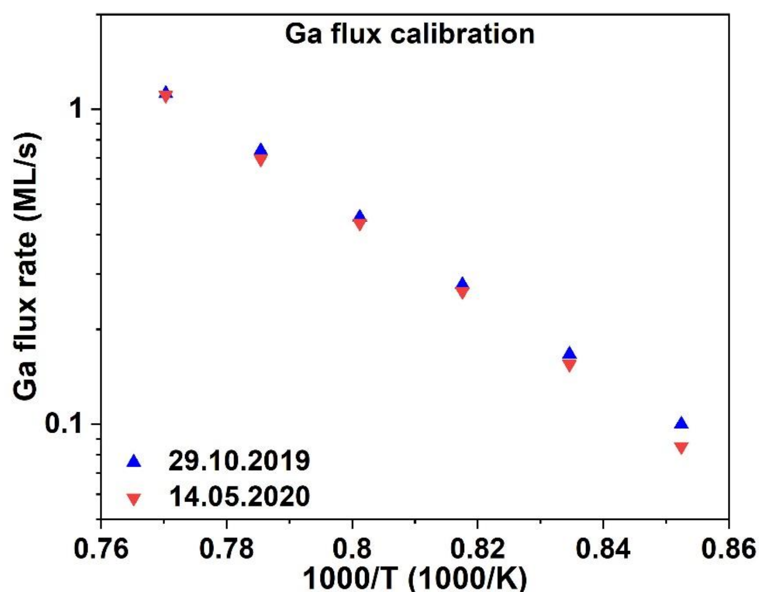

Figure 4.2. Ga flux dependence on the crucible temperature measured in different time.

4.2. Morphological characterization

Figure 4.3. The Veeco Innova scanning probe microscope.

In present work for the morphological characterization of samples we used AFM of the Vecco Innova scanning probe microscope (SPM) (see Figure 4.3), installed in L-NESS[120]. The advantage of AFM technique compared to STM method is the possibility to scan electrically non-conducting samples.

The main parts of the AFM are the SPM head with laser-photodetector system, the piezo scanner, and the cantilevered probe.

The head and attached X-Y stage are kinematically mated to the scanner via three contact points. A pair of retaining springs hold down the head, allowing it to be raised and lowered using adjustment screws threaded through the scanner body.

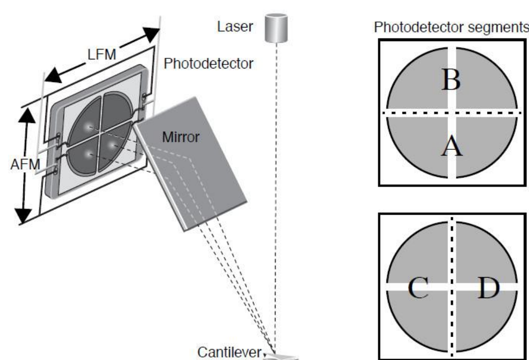

Figure 4.4. Representation of the arrangement of the photodiode elements in the SPM head. Different segments of the photodetector are used for generating Atomic Force Microscopy (AFM) and Lateral Force Microscopy signals.

Photodiode array – the four elements of the quad photodiode (see Figure 4.4) (position sensitive detector) are combined to provide different information depending on the operating mode. In all modes the four elements combine to form the sum signal. The amplified differential signal between the top two elements and the two bottom elements provides a measure of the deflection of the cantilever. Similarly, the amplified differential signal between the sum of two left photodiodes and the sum of the two right photodiodes provides a measure of the torsion in the cantilever.

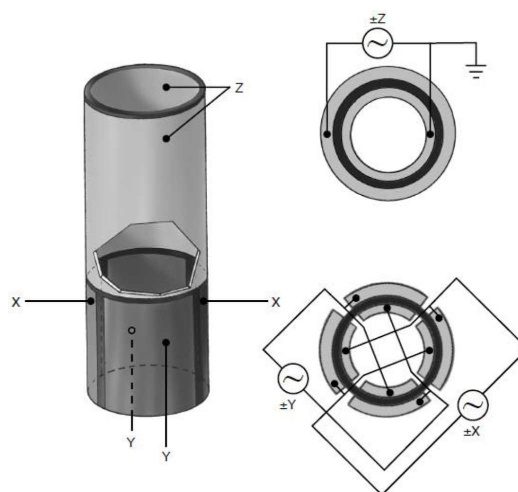

Figure 4.5. Typical scanner piezo tube and x-y-z electrical configurations.

The typical AFM scanner is a piezo tube (see Figure 4.5). Alternating current (AC) signals applied to conductive areas of the tube create piezo movement along the three major axes. AC voltages applied to the scanner crystal x-y axes produce a raster-type scan motion. One of the horizontal axes is referred to as the "fast axis" and scans at a scan rate (typically in our measurements we used 0.5 – 1 Hz scan rate). The second orthogonal axis is known as the "slow axis". In present work piezo scanner with 125 μm×125 μm scan size and about 5 μm vertical range was used.

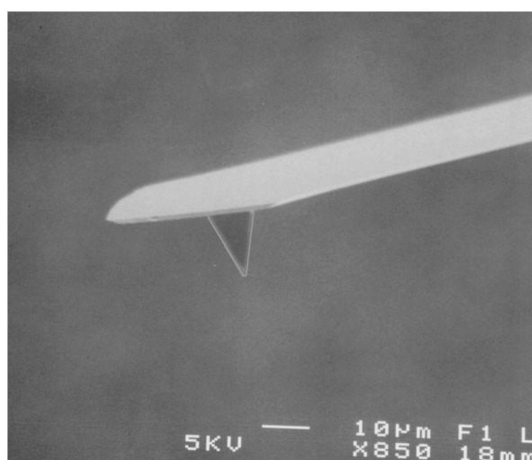

Figure 4.6. The image of silicon cantilevered AFM probe.

The typical AFM probe is presented in Figure 4.6. This consists of a flexible cantilever extending from a rigid substrate, to which a tip has been attached. The cantilever flexibility can act as a nanometric spring, allowing the tip to measure surface forces or the probe is oscillated up and down at its resonant frequency while its amplitude and phase are monitored. The AFM lateral resolution is determined generally by the tip radius of curvature. In present work two types of silicon tips was used: with 10 nm resolution and 2 nm resolution for high resolution scanning. The vertical resolution is limited by the position noise with mechanical, electrical, and thermal contributions and it is typically much below 1 nm (about 0.3 Å for AFM used in the present work).

All measurements in present work were performed in tapping mode (also known as intermittent contact mode) of AFM. The tapping mode AFM has certain advantages over the contact mode where the constant cantilever deflection is maintained. Using the tapping mode, the pressure of the cantilever on the surface is lower, which makes it possible to work with softer and easily destroyable materials, such as polymers, biomaterials, or materials in liquid phase (for instance, liquid Ga droplets). Also, the tapping mode AFM is more sensitive to interaction with the surface, allowing characterize different surface properties – distribution of the viscosity and elasticity, the electrical and magnetic domains[121].

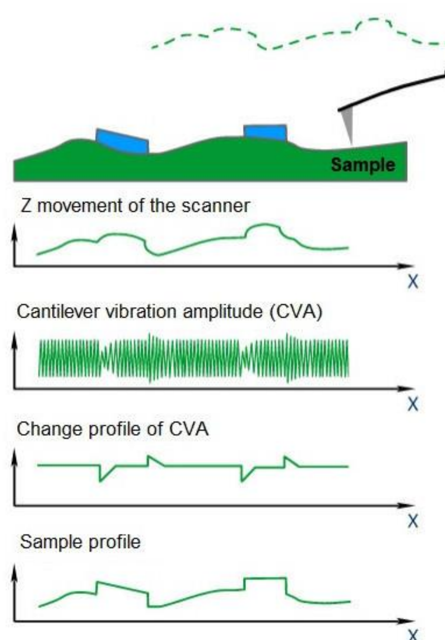

Figure 4.7. Schematic representation of the use of the cantilever vibrational amplitude (CVA) changes for the feedback in tapping mode AFM.

The scanning speed in tapping mode is limited by the response time. But this problem can be overcome. When the sample approaches the vibrating tip, they come into intermittent contact ("tapping"), thereby lowering the vibrational amplitude. The amplitude change can be used for the feedback. The new value of the cantilever oscillation amplitude is set faster than the feedback system will bring the oscillation amplitude to the set value. The time to establish a new value of the oscillation amplitude is determined by the oscillation period and the Q-factor of the cantilever. The feedback error signal (mismatch signal) arising during scanning by tapping mode contains additional information about the surface and can be used to obtain more accurate data on the surface relief[121].

Therefore, additionally the surface morphology can be characterized by cantilever amplitude scanned image. Gentle changes in relief will be poorly displayed on the scanned image, and abrupt changes will be displayed with high contrast. So, it can be useful for finding small irregularities

such as monoatomic steps or very small nano-scale islands on a large, relatively smooth surface. Figure 4.8 shows the cantilever amplitude and topography AFM images of the same GaAs(111)A surface with 2° miscut toward $(\bar{1}\bar{1}2)$ with DE GaAs QDs. Obviously, the amplitude image displays the sharp changes with a higher contrast, so we can see much better the steps (not necessarily monoatomic) of miscut GaAs surface and the shape of DE GaAs QDs. Unfortunately, such image does not give any information about the z-direction, but we can take it from topography AFM image.

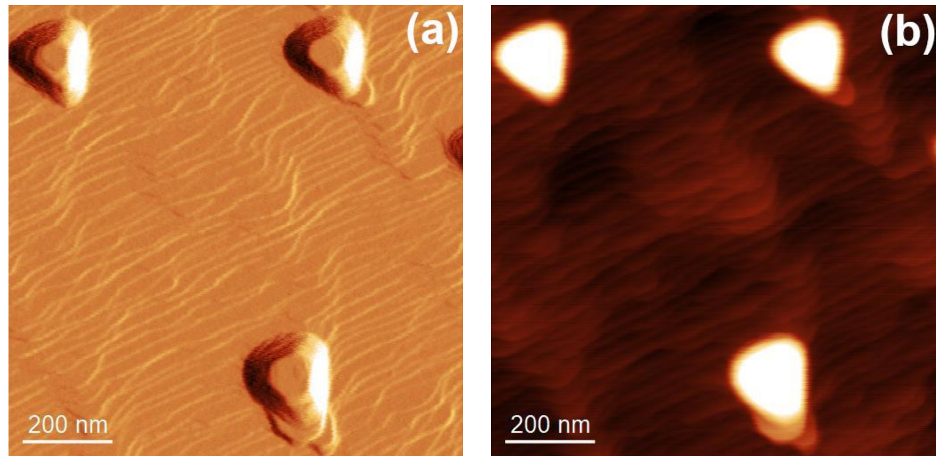

Figure 4.8. (a) Cantilever amplitude AFM image of the GaAs(111)A surface with 2° miscut towards $(\bar{1}\bar{1}2)$ with DE GaAs QDs. (b) Topography AFM image of the same surface.

All AFM images presented in this work were analyzed and obtained using Gwyddion[122] and ImageJ[123] software.

4.3. Photoluminescence setup

μ-PL study of telecom QDs has been carried out during my secondment period at Quantum Nano Photonic laboratory[124] of KTH Royal Institute of Technology in Stockholm, Sweden.

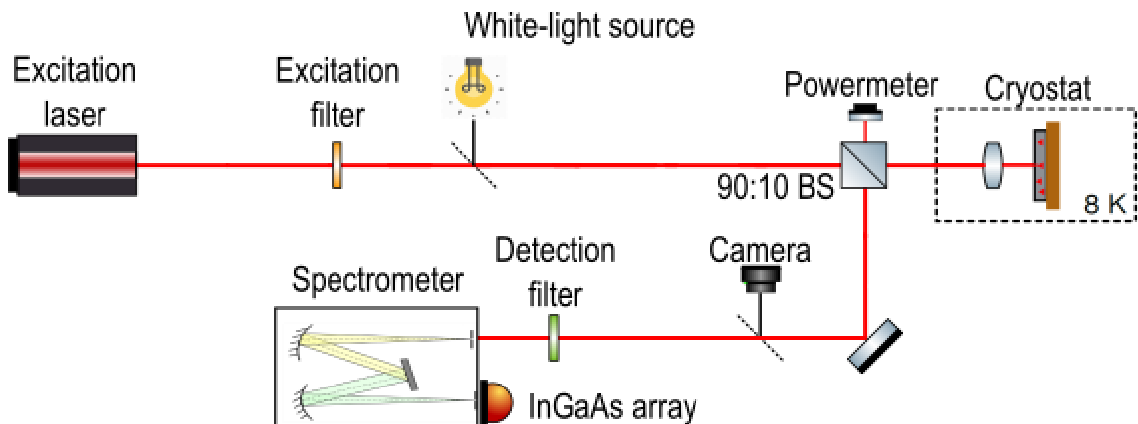

Figure 4.9. The scheme of μ-PL setup for characterization of single QDs.

The scheme of μ-PL setup is presented in Figure 4.9. QD samples are placed in closed-cycle cryostat in high vacuum (≈ 10^{-6} Torr) and cooled to 8 – 10 K. Inside the cryostat there is a piezoelectric precision stage to move the sample along *x*, *y*, *z* axes, allowing to address a distinct position with sub-micron resolution. To excite sample the continuous-wave HeNe laser (632 nm) was used. The laser light is focused on the sample using confocal microscope objective lens with a numerical aperture of 0.85. It creates a beam spot size of about 1 – 2 μm. The luminescence signal is collected by the same lens, passed through 90:10 BS to the SpectraPRO HRS 750 Czerny-Turner spectrometer consisting of a 830 line/mm grating. The luminescence signal is spectrally analyzed using a liquid nitrogen cooled InGaAs photodiode array, enabling detection wavelengths up to 1.6 μm. The resolution of the setup is about 0.07 nm (≈ 50.6 μeV at 1310 nm). The white-light source and the CCD camera was used to focus a laser beam on the sample surface.

To perform polarization-dependent PL measurements, half-wave plate (HWP) on the rotational stage as well as linear polarizing BS were inserted on the optical path before spectrometer. Observation of excitonic FSS below the resolution limit of the spectrometer can be achieved without special interferometric methods if a polarization-sensitive method is employed. As the FS-split components of the neutral exciton obey orthogonal linear-polarization rules, a single component can be selected by a detection side polarization filter (polarizing BS and HWP at the appropriate angle). Hence, switching between both FSS components results in an effective energy shift of the observed transition. And for shifts that are smaller than spatial sampling interval of photodetector pixel, the splitting can be extracted from the center-of-mass intensity[125]. The resolution of this method is mainly limited by the signal-to-noise ratio of the monitored transition. As reported in[126,127], this technique avoids systematic errors arising from the polarization optics and a resolution as small as 0.5 μeV can be achieved.

Part II. Results

Chapter 5. Droplet epitaxy on singular GaAs(111)A

As already mentioned in previous Chapters, the unique properties of self-assembled quantum dots (QDs) such as discrete energy levels and a precise control of the features by QD shape and size, have a great potential on the possible application in the optoelectronic devices[3,128–130]. The main challenge of the self-assembled QD fabrication is the reproducibility of QDs. There are two basic epitaxial growth methods: SK growth mode and DE technique. DE is well-established for fabrication of III-V compound semiconductor nanostructures and allows to control QD density and size in a wide range[99]. Size distribution of DE QDs remains the original size distribution of droplets[131]. Using DE technique, it is possible to obtain narrow QD size distribution, resulting in a small ensemble photoluminescence linewidth[132].

It has been predicted theoretically[31] and shown experimentally[32,133] that QD structures fabricated on (111) surfaces should feature vanishing the FSS due to the natural C_{3v} symmetry of the surface and the fabrication of highly symmetric QDs, which can be used for the entangled photon generation. Nevertheless, the fabrication of QDs on (111) compound semiconductor surfaces is not straightforward. The SK growth technique, like the prototypical InAs/GaAs system[134], due to the low threshold energy for compressive strain relaxation in epitaxial layers by the insertion of misfit dislocations at the substrate-epilayer interface, is not suitable to produce the QD self-assembly[34,35,135].

In this Chapter, the nucleation of GaAs QDs on GaAs(111)A substrates using DE technique was investigated and the growth conditions were identified, which allows QDs to self-assemble with the desired emission wavelength and highly symmetric shape maintaining a high optical quality.

5.1. Ga droplet nucleation

Buffer layer growth

Foremost, for DE QD fabrication it is necessary to have smooth barrier layer surface. The growth and the morphology of epilayers on GaAs(111)A was studied[136,137]. It was established that the epilayer morphology is strongly depends on the growth conditions. In order to obtain highly flat and smooth surface, it is necessary to use rather low growth rate and high V/III ratio[136] or to perform several annealing steps during the growth[137]. Otherwise, it is observed the formation of large (with μm lateral dimensions) triangular pyramidal hillocks consisting of up to several tens of steps, nucleated by staking faults[138].

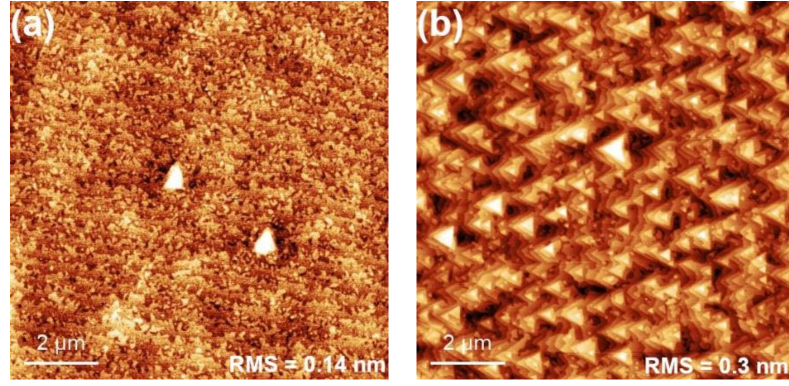

Figure 5.1. (a) 10×10 µm^2 AFM amplitude image of GaAs buffer layer morphology, grown using As BEP of 3.4×10^{-5} Torr according to[136]. (b) 10×10 µm^2 AFM amplitude image of GaAs buffer layer morphology, grown using As BEP of 2.0×10^{-5} Torr.

In present work, the GaAs buffer layer was grown according to[136]. After oxide desorption at 590 °C of an undoped GaAs(111)A substrates, a 50 nm GaAs buffer layer was deposited at growth temperature of 520 °C with a deposition rate of 0.07 ML/s (here and below 1 ML is defined as 6.26×10^{14} atoms/cm^2, which is the site-number density of the unreconstructed GaAs(001) surface. The buffer layer morphology is presented on Figure 5.1a. The buffer layer surface is very smooth with a root-mean-square (RMS) roughness of 0.14 nm. Nevertheless, small hillocks consisting of several steps can be nucleated. Changing the As BEP during the growth of GaAs buffer layer from 3.4×10^{-5} to 2.0×10^{-5} Torr leads to the morphology with the RMS roughness of 0.30 nm (see Figure 5.1b), which is close to the interplanar distance of GaAs in the [111] growth direction (d_{GaAs}(111) = 0.32 nm). Still the roughness is on the favorable level, but the presence of the high number of stepped hillocks makes the surface unsuitable for fabrication of DE QD with adjustable size.

Droplet density dependence on the deposition temperature

According to (3.16) of the classical nucleation theory[85,102], to determine the nucleation activation energy E_a, we need to know droplet density dependence on the deposition temperature, so only the number of droplets nucleated at different substrate temperature T:

$$N \propto \exp(E_a / k_B T). \tag{5.1}$$

On the basis of several studies[114,139,140], we assume that the density of DE III-V semiconductor compound QDs, crystallized at the same temperature as during the group III metal droplet deposition, equals the density of droplets. Therefore, the density of Ga droplets can be studied through the density of crystalline GaAs QDs due to their simpler measurement by AFM than liquid Ga droplets.

After buffer layer growth the substrate temperature was then decreased to the droplet deposition temperature varying from 250 to 450 °C and As cell valve was closed in order to deplete the growth chamber from the arsenic molecules. Then 2 ML of gallium were deposited with a rate of 0.01 ML/s. During the Ga deposition background pressure was below 3×10^{9} Torr. The supply of Ga without As_4 enabled the appearance of Ga liquid droplets on the buffer layer surface. Next, As_4 flux with a BEP of 6.2×10^{5} Torr was supplied at the same temperature for 3 minutes, to crystallize Ga droplets into GaAs QDs. Description of samples are summarized in Table 5.1.

Sample	T, °C	*N*, cm^{-2}	Comments
T1	250	$(1.72\pm0.10)\times10^{11}$	
T2	300	$(7.67\pm1.15)\times10^{10}$	
T3	350	$(1.83\pm0.06)\times10^{10}$	
T3b	350	$(1.85\pm0.09)\times10^{10}$	Arsenization after 30 min annealing
T4	400	$(2.27\pm0.05)\times10^{9}$	
T5	450	$(7.17\pm0.08)\times10^{8}$	

Table 5.1. Substrate temperature during the deposition of 2ML Ga with a flux of 0.01 ML/s and subsequent arsenization, and the GaAs QD density of the samples.

The morphology characterization of DE GaAs islands formed on the GaAs(111)A surface by was carried out by AFM. Figure 5.2 shows an AFM images of samples T1, T3, and T5 with GaAs QDs, grown at 250, 350, and 450 °C, respectively. As expected, with increasing deposition temperature the QD density decreases[99,114,139–141].

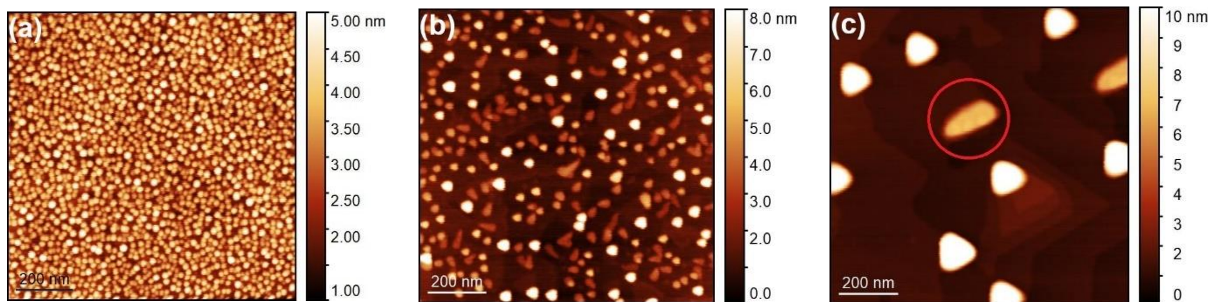

Figure 5.2. AFM topography images of GaAs QDs grown on GaAs(111)A substrate grown at (a) 250 °C (1×1 μm^2, sample T1); (b) 350 °C (1×1 μm^2, sample T3); (c) 450 °C (1×1 μm^2, sample T5). The red circle highlights a kinked dot.

It is worth to mention that some GaAs QDs fabricated on singular GaAs(111)A surface are "kinked" (Ga droplets spontaneously crystallized in a horizontal direction). One kinked dot is highlighted on Figure 5.2c. The analogues of such dots are the kinked NWs obtained by VLS growth on (111) surfaces[142–144]. A horizontal direction growth and subsequent formation of kinked NWs is induced by a twin-mediated mechanism, which can be suppressed/maintained by controlling growth conditions[143,144]. This behavior of spontaneous nucleation of kinked GaAs dots on singular GaAs(111)A surface is in agreement with the expected QD formation during the crystallization (arsenization) process of Ga droplets under VLS mechanism.

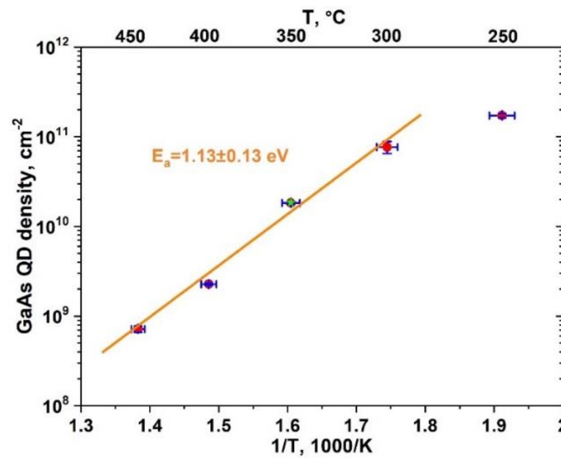

Figure 5.3. The temperature density dependence of DE GaAs QDs grown on singular GaAs(111)A substrate (samples T1, T2, T3, T4, and T5 – red circles). The activation energy calculation (E_a = 1.13±0.13 eV) does not include a point at 250 °C due to almost coalescence of the dots. The green star indicates the QD density of sample T3b. The temperature error bar is ±5 °C.

Plotting log(N) vs. 1/T, it is possible to calculate the activation energy E_a. Figure 5.3 shows the temperature density dependence of GaAs QDs in the range of 250 – 450 °C. The temperature error bar in our measurements is associated with the accuracy of the substrate temperature determination by the thermocouple and equals roughly ±5 °C. The density calculation was carried out using the data of several AFM scans from different areas of the samples. The density varies in the range of $7\times10^{8} - 2\times10^{11}$ cm^{-2}. The density of GaAs QDs grown at 250 °C is less than the expected value for an Arrhenius dependence. Similar behavior of drastically reduced density at T > 200 °C was observed for GaAs DE QDs grown on GaAs(001)[139] and Ga droplets on singular GaAs(111)A[141]. Such phenomenon was attributed to the onset of Ostwald ripening process (growth of large clusters on the cost of smaller ones and hence a decrease of the total cluster density in a closed thermodynamic system[145]). In order to check this hypothesis, we prepared sample T3b (see AFM image of the sample on Figure 5.4b), for which arsenization process was carried out after 30 minutes of annealing at droplet deposition temperature (350 °C). The QD density of the sample equals $(1.85\pm0.09)\times10^{10}$ cm^{-2} (green star on Figure 5.3). The value is almost the same as for sample T3 – $(1.83\pm0.06)\times10^{10}$ cm^{-2}, for which the annealing was not performed. Our observation

shows no Ostwald ripening occurs after the deposition of Ga droplets. So, we attribute the density decrease due to GaAs QD coalescence during the crystallization process. Therefore, we did not take into account the data obtained at 250 °C. The activation energy, calculated from temperature dependence of QD density, $E_a = 1.13 \pm 0.13$ eV.

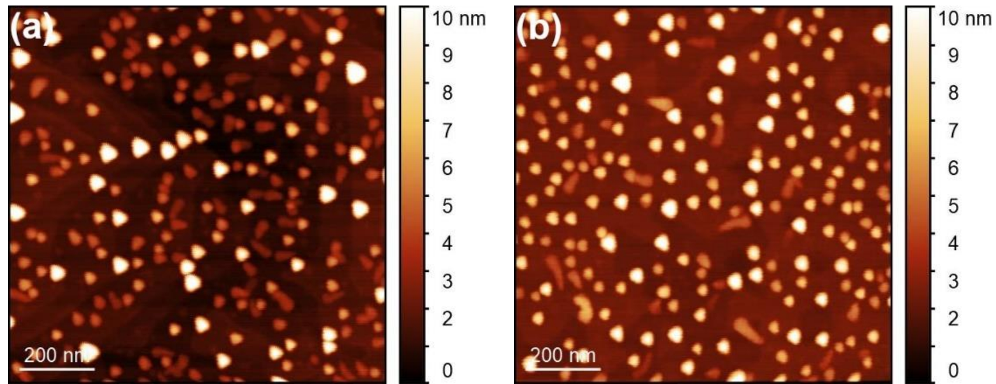

Figure 5.4. AFM topography images of GaAs QDs grown on GaAs(111)A substrate grown at (a) 350 °C without annealing step (1×1 μm^2, sample T3); (b) 350 °C with annealing step (1×1 μm^2, sample T3b).

Capture zone distribution

Another important parameter in the classical nucleation theory[85,102] is the critical cluster size i. According to (3.16), i can be calculated via the droplet density dependence on the group III flux F:

$$N \propto F^{p}, \tag{5.2}$$

where exponent p is a function of the critical cluster size. In the work[141], Ga droplet density dependence on the Ga deposition rate deposited on GaAs(111)A at 200 °C was obtained (see Figure 5.5). The dependence shows a power law, and the critical nucleus size i of Ga droplets on GaAs(111)A can be determined to be 1.

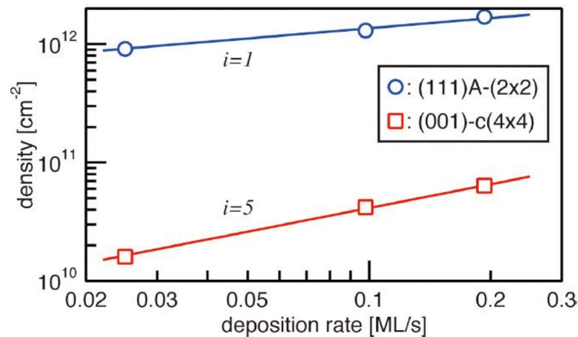

Figure 5.5. Densities of Ga droplets on GaAs(111)A plotted as a function of the deposition rate. The results were obtained at a substrate temperature of 200 °C. The results for GaAs(001)-c(4×4)β are also shown for comparison. The amount of Ga atoms consumed for the droplet formation is 1 ML for both surfaces[141].

We did not investigate the GaAs QD dependence on Ga flux rate, but the size of critical cluster i can be determined from CZD approach[103,104], described in Chapter 3.4.

To determine critical cluster size, it is necessary to analyze normalized (to the mean size of Voronoi cells) CZD distribution[103,104,140] (see Figure 5.6). The fitting parameter β depends on i and dimensionality of the diffusion γ as described in (3.18): $\beta = \gamma i + 1 + \gamma$.

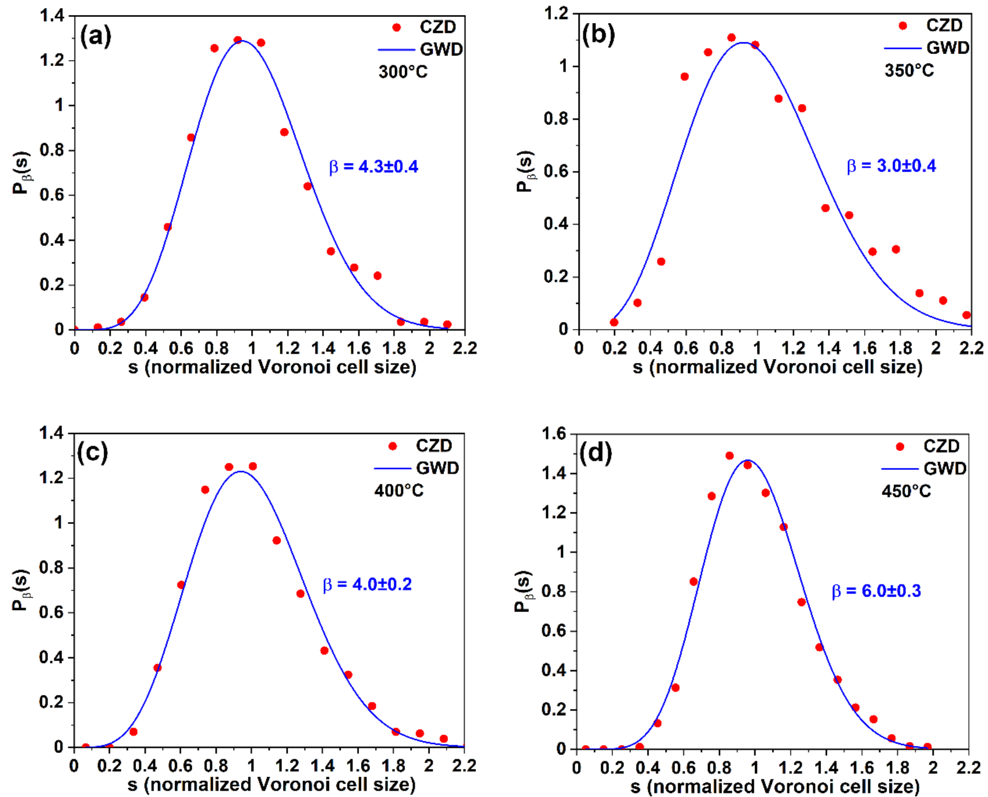

Figure 5.6. CZDs of samples (a) T2, (b) T3, (c) T4, and (d) T5, fitted by GWD.

The parameter β and the critical cluster size i obtained with $\gamma = 1$ (taking into account two-dimensional Ga adatom diffusion[104,140]) are presented in Table 5.2. For $T \leq 400$ °C the critical cluster size for Ga droplet nucleation on singular GaAs(111)A $i = 1$-2 atoms, which is in good agreement with the study[141], where i is determined via Ga droplet density dependence on Ga deposition rate. It means that stable Ga droplet cluster on GaAs(111)A consist of 2-3 atoms. Besides, an increase of the critical cluster size with the increase of deposition temperature is reasonable, since cluster binding process is also thermally activated one[85,102]. And with increasing T the probability of a stable cluster to be decomposed into adatoms increases exponentially.

Sample	T2 (300°C)	T3 (350°C)	T4 (400°C)	T5 (450°C)
β	4	3	4	6
$i = \beta - 2$	2	1	2	4

Table 5.2. The fitting parameter β and the critical cluster size i of samples T2 – T5.

Additionally, CZD method gives a possibility to determine the nucleation activation energy E_a. Figure 5.7 shows a temperature dependence of a mean size of Voronoi cells for samples T2, T3, T4, and T5. Naturally, the total number of Voronoi cells are related to QD density, so using this dependence, it is also possible to determine E_a. From CZD approach E_a = 1.13±0.23 eV, which is in agreement with the value determined from QD density dependence.

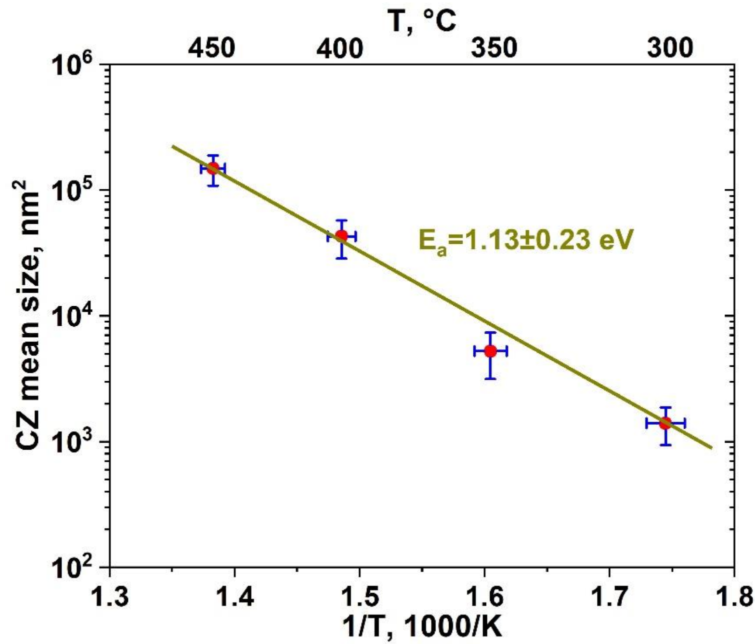

Figure 5.7. The temperature dependence of a mean size of Voronoi cells for samples T2, T3, T4, and T5. The activation energy, calculated from this method, equals E_a = 1.13±0.23 eV. The temperature error is also ±5 °C.

Diffusion of Ga adatoms

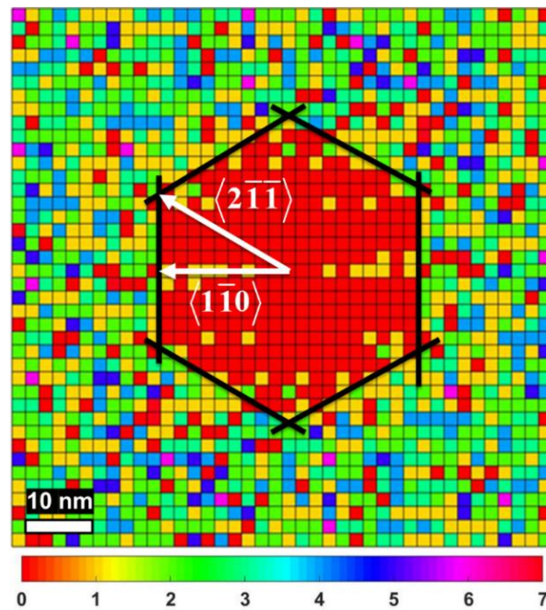

Figure 5.8. The spatial neighbor distribution of QDs for sample T2 (80×80 nm^2).

The diffusivity behavior of Ga adatoms can be monitored through the spatial neighbor distribution of QDs[140]. The spatial dispersion of neighboring QDs for sample T2 is presented in Figure 5.8. The distribution represents the position of neighboring dots around the selected one in the small area (80×80 nm^2 in that case) taking into account all dots in the 1×1 μm^2 AFM image. Therefore, such distribution is 2D histogram of neighboring dots and small colored squares represents bins of that histogram. It shows that the excluded area (the area without neighboring QDs) has a symmetrical, nearly hexagonal shape with vertices in the $\langle 2\bar{1}\bar{1}\rangle$ directions. The shape of the excluded zone suggests that $\langle 2\bar{1}\bar{1}\rangle$ directions are preferable for Ga adatom diffusion on GaAs(111)A.

This observation is in agreement with Ga-vacancy (2×2) surface reconstruction (see Figure 5.9a) of GaAs(111)A[146,147]. According to[147], on GaAs(111)A-(2×2) reconstruction the diffusion activation energies E_D equal 1.06 and 1.14 eV for the Ga adatom diffusion in the $\langle 2\bar{1}\bar{1}\rangle$ and $\langle 1\bar{1}0\rangle$ directions, respectively (see Figure 5.9b). Thus, the diffusion length in the $\langle 2\bar{1}\bar{1}\rangle$ directions should be longer, which was observed from the excluded zone area.

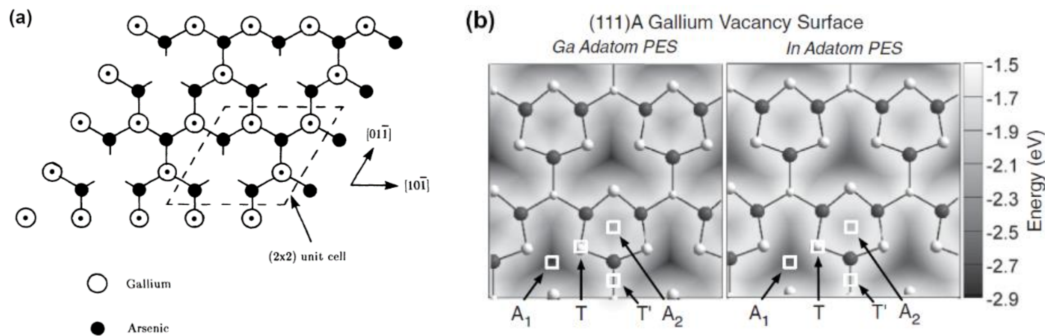

Figure 5.9. (a) Top view of the single-gallium-vacancy model of the GaAs{111)A-(2×2) reconstruction showing the surface gallium atoms and the arsenic atoms immediately below[146]. (b) Potential energy surface for Ga and In adatoms above the Ga vacancy surface. The binding energies at adsorption sites A_i, transition points T and T', the primary diffusion barrier E_D = T−A_1 = 1.06 eV, and the secondary diffusion barrier E'_D = T'−A_1 = 1.14 eV for Ga adatom above the surface[147].

QD size distribution

The last goal was to study a size distribution of QDs. Figure 5.10 shows the QD height distribution of samples T2, T3, T4, and T5 fitted by Gaussian line shapes. At the low deposition temperature of 300 °C the size distribution has a mean QD height of about 2.7 nm with a standard deviation of 43% (Figure 5.10a). A Similar situation is observed at the high temperature of 450 °C (Figure 5.10d). The mean height for sample T5 is about 15.3 nm with the standard deviation of 45%. And the most intriguing observation is the two peaks in the distributions at the intermediate

temperature of 350 – 400 °C, which can be attributed to the bimodal QD size distribution[148,149]. The sample T3 (Figure 5.10b) has two groups of QDs with the mean heights of 4.1 and 8.7 nm. And the mean QD heights for sample T4 (Figure 5.10c) are 7.0 and 14.8 nm. For both cases, the height of bigger dots are approximately two times larger than the height of small ones (2.12 for the sample T3 and 2.11 for T4).

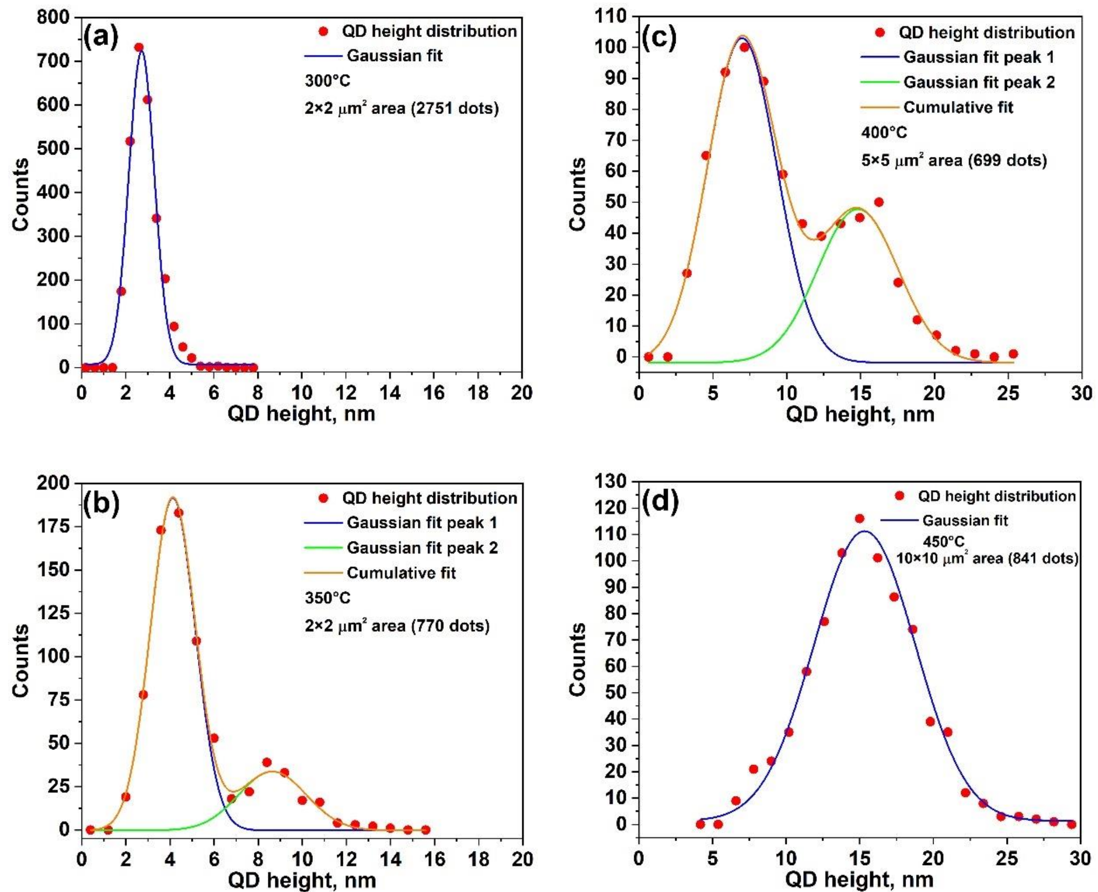

Figure 5.10. (a) The QD height distribution of samples (a) T2, (b) T3, (c) T4, and (d) T5. For the samples T2 and T5 the unimodal distribution is observed with a standard deviation of about 44% for both samples. The samples T3 and T4 have the bimodal distribution.

The most known systems, where bimodal QD size distribution was observed, is the SK InAs/GaAs(001) QDs[148–151], where the bimodal behavior was described in terms of InAs coverage, which is the distinct threshold for the SK dot formation[150,151], and SK Ge/Si(001) islands[152,153], for whom the morphological shape transition of Ge islands is responsible for the bimodal distribution.

In order to understand the origin of bimodal distribution in our samples, we analyzed the size of QDs nucleated in different positions for sample T4, since the bimodal behavior is strongly observed for this sample. Figure 5.11a shows a 1×1 μm^2 AFM image of sample T4 with GaAs QDs grown at 400 °C. The height profiles of 5 dots are presented in Figure 5.11b. The maximum height of dots 1-3 (which we denote as big dots) is about 9 – 12 nm. And the maximum height of small dots 4-5 is about 5 – 6 nm. The most important feature is the position of these dots. The big

dots are localized close to the step edges and the small dots are found near the middle of flat terraces.

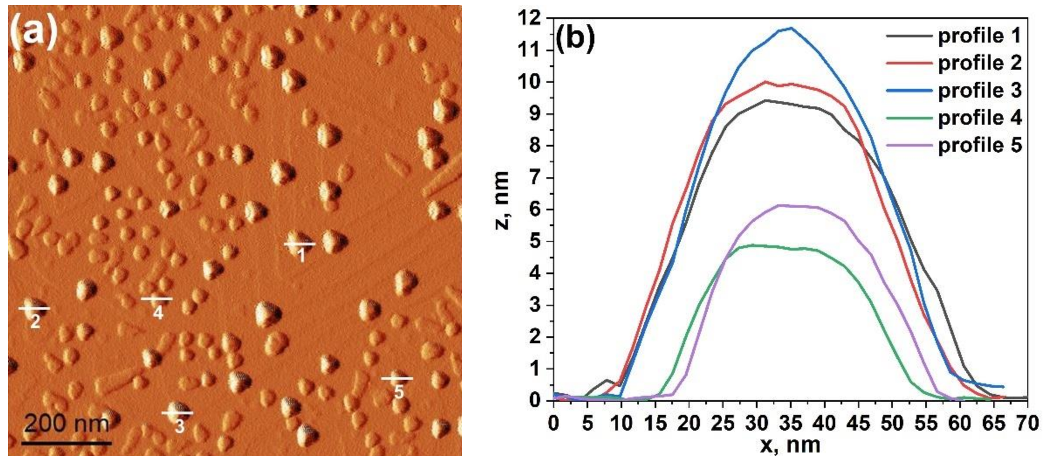

Figure 5.11. (a) 1×1 μm^2 AFM amplitude image of sample T4. The height profiles of 5 dots of the sample taken from (a) are presented in (b).

As already mentioned, we did not observe ripening processes of Ga droplets. Therefore, the bimodal behavior of GaAs DE QDs grown on GaAs(111)A at the intermediate temperature 350 – 400 °C can be explained in terms of original surface morphology, Ga droplet nucleation on the surface, and Ga adatom surface diffusion.

There are triangular pyramidal hillocks on GaAs(111)A surface, which can consist of a huge number of steps (in our samples we observed hillocks with up to 15 monoatomic steps). At intermediate temperature if the droplet is nucleated in the middle of flat terrace, the droplet can capture adatoms only from the terrace, where it is located, due to the presence of sizable Ehrlich-Schwöbel (ES) barrier of GaAs(111)A surface[136,137,140], which hinders adatom diffusion through step edges. If the droplet is nucleated close to the step edge, ES barrier does not prevent the capture of adatoms from both upper and lower terraces. Apparently, it leads to the fact that the height of big QDs, which are crystallized from droplets nucleated on the step edges, are two times larger than the height of small ones, nucleated on the middle of the terraces. The absence of bimodal distribution at lower and higher deposition temperatures is related to the Ga adatom diffusion length. At low temperature, the diffusion length is shorter than the terrace width, and droplets are nucleated everywhere without preferable positions. At rather high deposition temperature, adatoms can easily overcome ES barrier, and droplets can capture adatoms from several terraces.

5.2. QD shape control

The problem of bimodal distribution of GaAs QDs on singular GaAs(111)A does not arise if QDs are needed for single and entangled photon generation due to the fact that for these purposes the density of QDs should be on the range of $10^8 – 10^9$ cm^{-2}. From Figure 5.3 to obtain the Ga droplet

density less than 10^9 cm^{-2}, it is necessary to deposit Ga droplets at $T \geq 450$ °C, where bimodal distribution is not observed.

The next question – could we control the QD shape during the crystallization step on (111)A surfaces as well as on (001) surfaces?

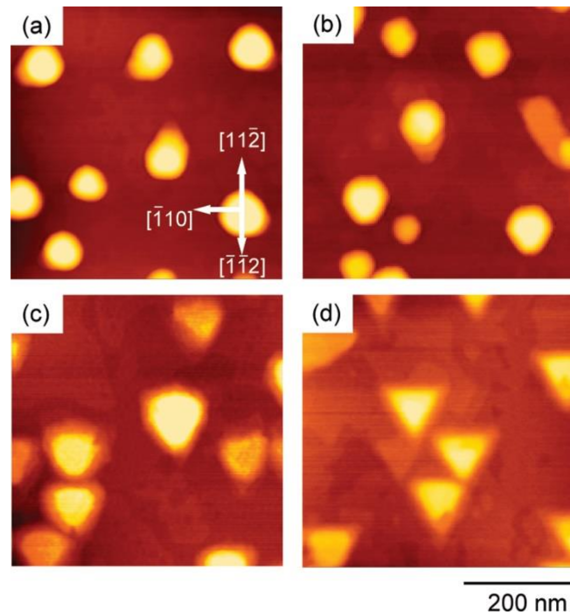

Figure 5.12. 500×500-nm AFM images of GaAs QDs crystallized at different temperatures: (a) 200, (b) 300, (c) 400, and (d) 500 °C. Transition from hexagonal to triangular QDs is visible[39].

M. Jo et al.[39] studied the formation of GaAs QDs on GaAs(111)A and observed shape transition from hexagonal to triangular QDs with increasing crystallization temperature (see Figure 5.12). The group III atom deposition step was performed at 450 °C for all samples, thus the Ga droplet density is the same. At low crystallization temperature of about 200 °C the shape of dots is hexagonal pyramid. The base is a hexagon with the sides normal to $\langle 11\bar{2} \rangle$ directions (see Figure 5.12a). At high temperature of 500 °C QDs have triangular pyramidal shape (see Figure 5.12d). The base is ideal triangle with sides perpendicular to $[11\bar{2}]$, $[1\bar{2}1]$, and $[\bar{2}11]$ directions. Authors called it as B sides. A sides are sides perpendicular to $[\bar{1}\bar{1}2]$, $[\bar{1}2\bar{1}]$, and $[2\bar{1}\bar{1}]$ (see Figure 5.13b). And at the intermediate crystallization temperature of 300 – 400 °C the shape of QDs is in between ideal hexagonal and triangular base pyramid. The sides are no longer equivalent and A sides of dots are shorter that B sides (see Figure 5.12b, c).

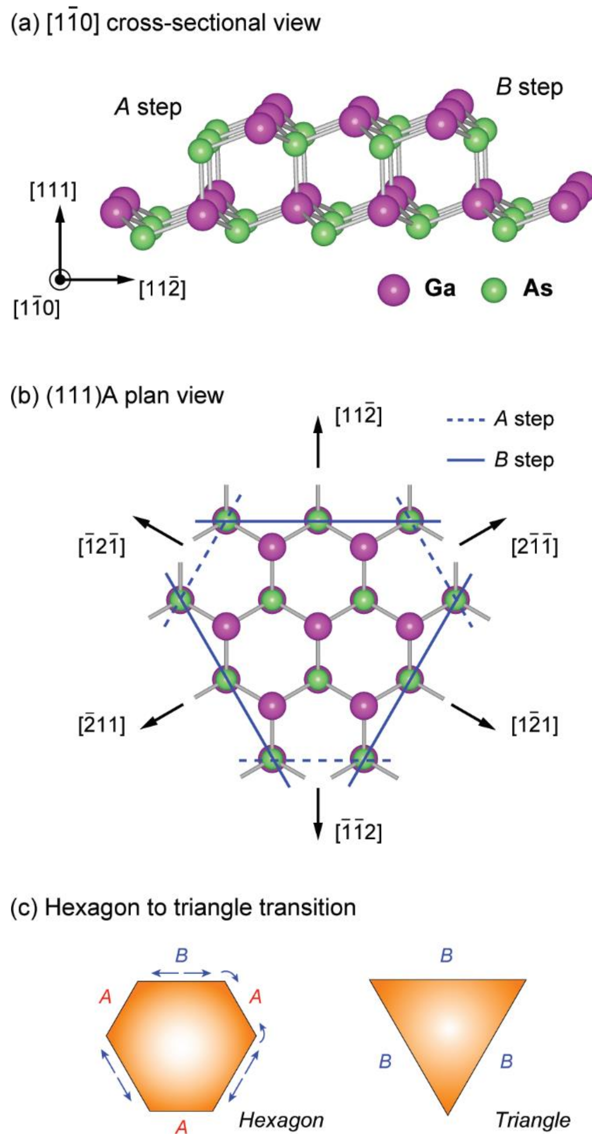

Figure 5.13. Schematic drawing of a GaAs(111)A surface. (a) Cross-sectional view along the $\left[1\,\bar{1}0\right]$ direction. (b) (111)A plan view. (c) Shape evolution of a GaAs QD from hexagon to triangle[39].

Such transition between hexagonal and triangular islands has been explained in terms of the different growth rates of step edges on a (111)A surface. Figure 5.13 presents two types of steps on a GaAs(111)A surface. A steps perpendicular to A sides have two dangling bonds per edge atom, whereas B steps perpendicular to B sides have only one dangling bond per atom. A steps grow faster since the probability to incorporate to A steps is higher due to higher amount of dangling bonds compared to B steps. Therefore, at high crystallization temperature when Ga adatom surface diffusion is high, triangular base dots with B sides are formed. With decreasing the crystallization temperature, the difference in the growth rates along A and B steps are, also, decreasing and became insignificant at temperature of about 200 °C, so it is observed hexagonal base pyramid shape QDs[39].

5.3. High-temperature symmetrical QDs

In terms of the symmetry the hexagonal base QD with the D_6 symmetry has to be considered as more symmetrical than triangular base QD with D_3 point group symmetry. Thus, hexagonal QDs on (111)A surfaces are preferable to obtain for entangled photon generation. But, as we can see from the previously mentioned study[39], such shape of QDs can be obtained at low crystallization temperature. It means that crystal quality and consequently optical properties of the dots is poor without additional annealing steps.

From the investigations about LDE GaAs QDs on GaAs(001)[27,29,52], we know that such dots show excellent performance of the crystal quality and optical properties. Of course, one of the main advantages is the temperature during the fabrication process.

Therefore, the possibility to fabricate hexagonal QDs on (111)A surfaces at high temperature should have an impact on the optical properties and FSS. Therefore, we have studied an influence of As flux during the crystallization of Ga droplets on GaAs(111)A[40].

After the oxide desorption at 580 °C, an atomically smooth surface was prepared by growing a 100 nm thick GaAs buffer layer and a 50 nm $Al_{0.3}Ga_{0.7}As$ barrier layer after reducing the temperature to 520 °C. To achieve a smooth surface with minimal surface roughness (RMS below 0.5 nm), again the growth conditions were kept according to[136]. The substrate temperature was then decreased to 450 °C and the As valve closed in order to deplete the growth chamber from the arsenic molecules. When the background pressure reached a value about 1×10^{-9} Torr, 0.4 ML of Ga was supplied to the substrate surface with a rate of 0.01 ML/s to form droplets. During the Ga supply the surface reconstruction did not show any change. One sample with Ga droplets (sample D) was then removed from the growth chamber. Simple calculations considering the volume of the droplets, the density, and the amount of the deposited Ga, demonstrate with good agreement that all the gallium is collected inside the droplets. This is in agreement with the fact that GaAs(111)A surface is Ga terminated and the Ga excess, during gallium deposition, immediately creates droplets on the surface.

For the other samples, in order to study the influence of substrate temperature and As flux during the crystallization on the QD formation, the substrate temperature was decreased to low temperature, 200 °C (sample L) or medium temperature, 400 °C (sample M) or increased to high temperature, 500 °C (the samples of H series) and then the Ga droplets irradiated with As flux for 5 minutes. The irradiated As BEP is reported in Table 5.3.

Sample	*T* during arsenization, °C	As BEP, Torr
D	–	–
L	200	2×10^{-6}
M	400	2×10^{-6}
H_1	500	2×10^{-6}
H_2	500	5×10^{-5}

Table 5.3. Substrate temperature and As flux for the droplet crystallization of samples.

Figure 5.14 shows AFM images of samples D, L, M, H_1, and H_2. Samples L, M, and H_1 (Figure 5.14 b, c, and d, respectively), on which droplets were arsenized with a BEP of As of 2×10^{-6} Torr at substrate temperature of 200, 400 and 500 °C, respectively, show the formation of QDs with different shapes. On sample L truncated pyramids with a regular hexagonal base are formed, while truncated pyramids with equilateral triangular base are formed on sample H_1. Sample M shows an intermediate behavior. The QDs show a truncated pyramidal shape with an irregular hexagonal base. The shapes of the dots of samples L, M, and H_1 are in agreement with the previous work[39]. Nevertheless, M. Jo et al.[39] have not study an influence of As flux on QD shape. Figure 5.14e presents an AFM scan of single QD of sample H_2, where the droplets were arsenized at 500 °C with As BEP of 5×10^{-5} Torr. Here the QDs show a truncated pyramidal shape with regular hexagonal base.

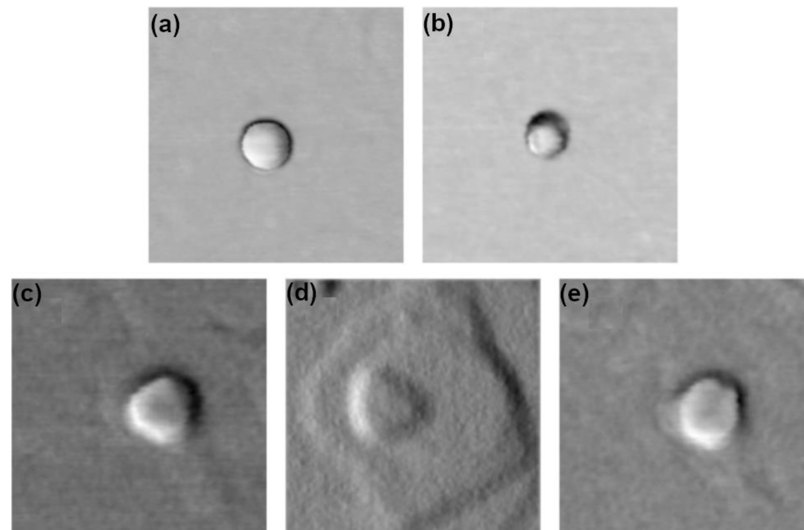

Figure 5.14. 250×250 nm^2 AFM topography scans of single nanostructure on (a) sample D (droplets obtained by deposition of 0.4 ML of Ga at a substrate temperature of 4500 °C), (b) sample L (GaAs dots obtained by deposition of 0.4 ML of Ga at a substrate temperature of 450 °C and arsenization at 200 °C with As_4 BEP of 2×10^{-6} Torr), (c) sample M (GaAs dots obtained by deposition of 0.4 ML of Ga at a substrate temperature of 450 °C and arsenization at 400 °C with As_4 BEP of 2×10^{-6} Torr), (d) sample H1 (GaAs dots obtained by deposition of 0.4 ML of Ga at a substrate temperature of 450 °C and arsenization at 500 °C with As_4 BEP of 2×10^{-6} Torr), and (e) sample H_2 (GaAs dots obtained by deposition of 0.4 ML of Ga at a substrate temperature of 450 °C and arsenization at 500 °C with As_4 BEP of 5×10^{-5} Torr).

The shape of the QDs on samples L, H_1 and H_2 are graphically summarized in Figure 5.15 and compared with the size of the original droplet. Comparing the mean dimensions of Ga droplets on sample D (orange), and of QDs on samples L (light green) and H_1 (light blue), it is possible to see that the formation of QD crystallized with 2×10^{-6} Torr As BEP, while increasing the substrate temperature from 200 to 500 °C, is dominated by incorporation exclusively along A steps, while the incorporation along B steps is suppressed. It can be observed clearly from Figure 5.15a that the sides of the hexagonal dot on sample L (in light green) is mostly tangent to the base circle of the original droplet (orange), and that the sides of triangular dots on sample H_1 (light blue) are mostly tangent to the base circle of the original droplet only along B steps, thus confirming the absence of incorporation in those directions. These observations confirm that the shape of the QDs is determined by kinetically controlled diffusion and incorporation processes in which the different growth velocity between A and B steps determines anisotropy at high temperature[39].

By increasing the As BEP up to 5×10^{-5} Torr at high substrate temperature, it is possible to obtain again QDs with hexagonal symmetrical shape. A graphical representation is reported in Figure 5.15b. Here we consider the shape and the mean size measured for the original gallium droplet (orange) and we compared it with the shape and the mean size measured for the QDs on sample H_2 (dark green). Also, it can be observed that on sample H_2 all the sides of the hexagonal dots are away but at the same distance from the base circle of the original droplet.

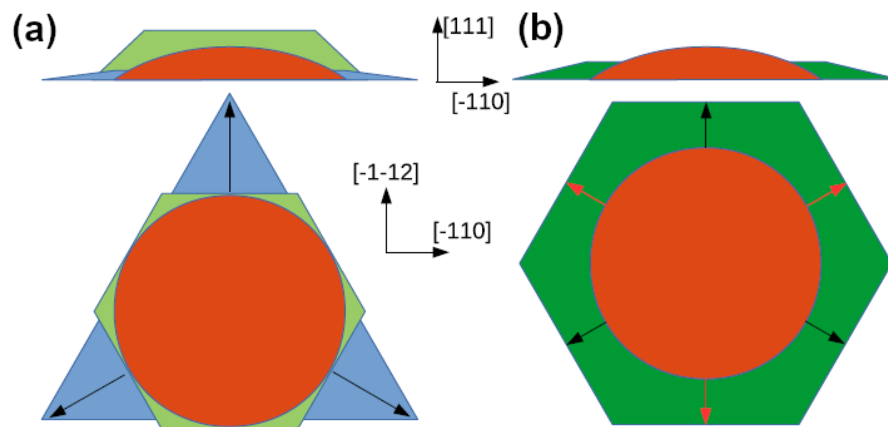

Figure 5.15. Sketch of mean sized quantum dot on sample L, H_1 and H_2 compared with the original Ga droplet size. (a) Graphical representation of mean sized droplet on sample D (orange) and of quantum dot on samples L (light green) and H_1 (light blue). (b) Graphical representation of mean sized droplet on sample D (orange) and of quantum dot on sample H_2 (dark green). Black and red arrows in (a) and (b) indicate directions perpendicular to steps A and B, respectively.

In order to understand presented phenomenology, Ga diffusion length on B steps l_B was analyzed. When $l_B > L_B$ (the B step length), the Ga adatom arriving at B steps can easily diffuse along the step and then reach the A steps with higher incorporation rate. The consequent higher growth rate of the A steps, due to both higher incorporation probability and higher Ga atom flux with respect

to B steps, causes the disappearance of the A steps. This leads to a triangular QD shape limited by facets with B steps. On the other side, when $l_B < L_B$, there is no transfer of Ga atoms between B and A steps and Ga is incorporated at the arrival step. This condition leads to QDs with a hexagonal shape. The l_B is controlled by the Ga diffusivity along the B steps $D_{Ga}^{B} \propto \exp\left(-E_D / kT\right)$, where E_D is the diffusivity activation energy, and by Ga average time $\tau \propto 1/J_{As}$ (J_{As} is As flux) between the arrival and the reaction at the step: $l_B = \sqrt{D_{Ga}^{B} \cdot \tau} \propto \exp\left(-E_D / 2kT\right) \cdot J_{As}^{-1/2}$. The diffusion length is, therefore, minimized by low temperatures and/or high As fluxes growth conditions.

Comparing samples L and H_2, the two which exhibit QDs with hexagonal shape, we observe that the increase in the arsenization temperature from 200 °C (L) to 500 °C (H_2) determines an increase of a factor 5 of the diffusivity term in l_B while the concurrent increase in J_{As} from 2×10^{-6} Torr (L) to 7×10^{-5} Torr decreases the Ga lifetime around factor 6. Therefore, the two effects cancel each-other in the determination of diffusion length, leaving almost unchanged l_B. We then interpret the observed QD hexagonal shape in L and H_2 samples as the results of $l_B < L_B$ due to the low temperature (L) and high As flux (H_2) growth conditions. As a result, we can state that Ga diffusion length on B steps is the physical parameter that controls the kinetics of the growth, and thus, in turn, the QD shape.

The described behavior allows for the growth of GaAs QDs by DE at substrate temperature much higher than the one typically used on (001) substrates and, compared to the data previously reported on (111)A substrates, to preserve the hexagonal shape also for arsenization performed up to 500 °C. This is expected to allow for the growth of materials with improved crystalline quality with respect to the usual DE QDs crystallized at 200 °C. In fact, a low temperature of crystallization for the Ga droplets[154,155] and subsequent AlGaAs barrier deposition[156] is detrimental for the crystalline and the optical quality of the QDs, mainly due to the formation of vacancies and the incorporation of defects.

As a result, the highly symmetric dots obtained with this modified recipe (high substrate temperature and high As flux for the droplet crystallization) show a mean line width of the neutral exciton of about 15 μeV and a best value of 9 μeV, a mean FSS of 4.5 μeV, which results in the large fraction (more than 95%) of emitters capable of generating entangled photon, as reported in[13].

Conclusions

DE fabrication of GaAs QDs on GaAs(111)A substrates have been studied. The temperature dependence of GaAs QD density in the range of 250 – 450 °C was investigated. The activation energy E_a = 1.13±0.23 eV was calculated by two approaches (from QD density dependence[85,102] and CZD[103,104]). Also, using CZD the critical cluster size i for Ga droplet nucleation on GaAs(111)A was estimated, taking into account two-dimensional behavior of Ga adatom diffusivity[104,140]. i = 1-2 atoms at deposition temperature T < 400 °C and 4 atoms at 450 °C. We monitored the spatial neighbor distribution of QDs. It shows that the area without neighboring QDs has a symmetrical, nearly hexagonal shape with vertices in the $\langle 2\bar{1}\bar{1} \rangle$ directions. The shape of the excluded zone suggests that $\langle 2\bar{1}\bar{1} \rangle$ directions are preferable for Ga adatom diffusion on GaAs(111)A. This observation is in agreement with Ga-vacancy (2×2) surface reconstruction of GaAs(111)A[146,147]. And we observed the bimodal size distribution of GaAs QDs, grown at intermediate temperature of 350 – 400 °C, attributed to an influence of surface morphology and Ga adatom surface diffusion during Ga droplet nucleation process. Small droplets are nucleated close to the middle of big flat terraces. Otherwise, the big droplets are nucleated near the step edges of the terraces.

We investigated and modeled the dependence of the QD shape and size on the growth parameters during the crystallization process. The model proposed shows that high temperature droplet epitaxy on (111)A substrates is governed, as the standard droplet epitaxy on GaAs(001), by the balance between crystallization within the droplet and the process of Ga adatom detachment from the droplet, diffusion and incorporation into the crystal surrounding the droplet. The predominance of the former over the latter allows for the self-assembly of 3D islands. This is realized on GaAs(111)A substrates at high T owing to the low residence time of the As on the (111)A surface which hinders the diffusion/crystallization processes on the crystal surface around the droplet. The high As pressure required for the crystallization also permits the equalization of the growth velocities along the A and B steps by increasing the incorporation of Ga adatoms along the B steps, resulting in a symmetric hexagonal shape. As a result, the highly symmetric GaAs/AlGaAs QDs obtained with this modified recipe (high substrate temperature and high As flux for the droplet crystallization) show a mean line width of the neutral exciton of about 15 μeV and a best value of 9 μeV, a mean FSS of 4.5 μeV, which results in the large fraction (more than 95%) of emitters capable of generating entangled photon[13].

Chapter 6. Droplet epitaxy on vicinal GaAs(111)A

As previously mentioned, the general issue, related to the epitaxial growth on a singular (111) surface, is the formation of large pyramidal hillocks, nucleated by stacking faults[138]. To create well-defined DE QDs, a flat surface should be obtained. Optimal growth conditions for Ga(Al)As layers on a singular GaAs(111)A surface are low growth rate and high V/III flux ratio[136], so the growth of QD embedded in a planar cavity with the thick DBRs becomes problematic on the singular (111)A surface. These critical requirements can be mitigated using a vicinal (111) surface, in which the growth conditions (high growth rate and low V/III ratio) are similar to those for a GaAs(001) surface thanks to the presence of preferential nucleation sites at the step edges[133,154]. However, in this case, presence of steps should change the formation process and the distribution of nanostructures. Accordingly, understanding the metal droplet nucleation process and QD formation dynamics on (111) vicinal surfaces in QD-DE self-assembly is, therefore, a fundamental step for improving presented QD devices.

GaAs QD fabrication on misoriented GaAs(111)B substrates with a miscut of 1° toward (211) have been already studied[158]. During droplet deposition and arsenization, rather low substrate temperatures had to be employed to suppress the strong Ga diffusion on the (111)B surface[159] and achieve the desired droplet density of about $10^8 – 10^9$ cm^{-2}. The only effect of the miscut on the DE process could be observed on big Ga droplets deposited at high temperatures. They do not show the desired circular symmetry but are elongated in the direction of the miscut. Medium and small droplets were not influenced by the misorientation.

6.1. GaAs QDs on vicinal GaAs(111)A

Buffer layer growth

Samples were grown on semi-insulating GaAs(111)A substrates with a miscut of 2° miscut toward $(\bar{1}\bar{1}2)$. We observed a good reproducibility of the temperature (580 °C) for native oxide desorption and appearance of (2×2) reconstruction[146,147]. After oxide desorption at 590 °C, a 130 nm GaAs buffer layer was deposited at growth temperature of 520 °C, to obtain a smooth surface. The growth rate was 0.5 ML/s. The BEP of As_4 flux was set at 2×10^{-5} Torr. Then, the surface was smoothed out at the same temperature and As_4 BEP of 8.7×10^{-6} Torr for 5 minutes. During the growth of the buffer layer, only (2×2) reconstruction is observed.

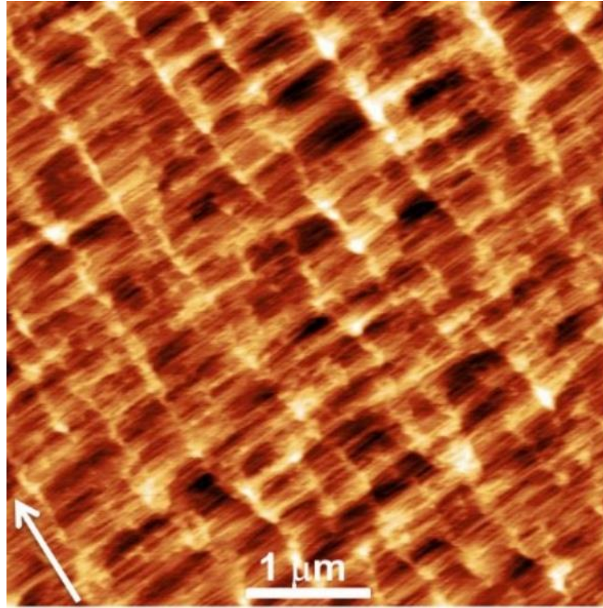

Figure 6.1. AFM topography image (5×5 μm^2) of GaAs buffer layer grown on GaAs(111)A with 2° miscut toward $(\bar{1}\bar{1}2)$. Arrow indicates $[\bar{1}\bar{1}2]$ direction perpendicular to steps. The average terrace width is 12.8 nm.

The sample surface topography, measured by AFM, before the metallic Ga deposition is shown in Figure 6.1. Via AFM measurements we have determined that the GaAs buffer layer consists of terraces separated by step with height in the 1 – 3 ML range. The measured average width of the terraces in our conditions is 12.8 nm. (The width of 1 ML terrace is 9.3 nm). The step edges are perpendicular to the $[\bar{1}\bar{1}2]$ direction.

Ga droplet nucleation

We have investigated the nucleation of Ga droplets and fabrication of DE GaAs QDs on vicinal GaAs(111)A substrates and the influence of deposition conditions on the QD density and shape[140].

After the growth of buffer layer, the substrate temperature was then decreased to the droplet deposition temperature varying from 300 to 500 °C and As cell valve was closed in order to deplete the growth chamber from the arsenic molecules. Then 2 ML of Ga were deposited with a rate of 0.01 – 0.08 ML/s. During the Ga deposition background pressure was below 3×10^{-9} Torr. The supply of Ga without As_4 enabled the appearance of Ga liquid droplets on the surface. The surface reconstruction remained (2×2) also during this step. Next, As_4 flux with BEP of 6.2×10^{-5} Torr was supplied at the same temperature for 3 minutes, in order to crystallize Ga droplets into GaAs QDs. A sample D2 was prepared without annealing in As_4 atmosphere, this leaving liquid the Ga droplets on the surface. Growth conditions of samples are summarized in Table 6.1.

Sample	T, °C	Ga flux, ML/s	N, cm^{-2}
T1	300	0.01	$(4.1\pm0.5)\times10^{10}$
T2	350	0.01	$(5.6\pm0.5)\times10^{9}$
T3	400	0.01	$(4.7\pm0.3)\times10^{8}$
T4	450	0.01	$(3.6\pm0.1)\times10^{8}$
T5	500	0.01	$(1.7\pm0.1)\times10^{8}$
F1	350	0.01	$(5.6\pm0.5)\times10^{9}$
F2	350	0.04	$(2.8\pm0.4)\times10^{10}$
F3	350	0.08	(4.2±0.4)×1010
F4	450	0.01	$(3.6\pm0.1)\times10^{8}$
F5	450	0.04	$(5.9\pm0.4)\times10^{8}$
F6	450	0.08	$(7.9\pm0.3)\times10^{8}$
D1	350	0.01	$(5.6\pm0.5)\times10^{9}$
D2	350	0.01	$(7.2\pm1.1)\times10^{9}$

Table 6.1. Conditions used for the growth of the samples on vicinal GaAs(111)A substrate. The deposition temperature, Ga flux rate during Ga droplet deposition, and the density of GaAs QDs (Ga droplets for sample D2) of samples are indicated.

A fundamental starting point is the demonstration that the QD density measured after the annealing in As_4 atmosphere equals the density of droplets formed during the Ga deposition also on the vicinal GaAs(111)A substrate. This assumption is tested by comparing samples D1 and D2, obtained using the same conditions for the deposition of the Ga droplets. On sample D2 the density of Ga droplets is $(7.2\pm1.1)\times10^{9}$ cm^{-2}, thus in agreement with the density of GaAs QDs measured in sample D1: $(5.6\pm0.5)\times10^{9}$ cm^{-2}. The surface topography of the samples D1 and D2 is presented in Figure 6.2.

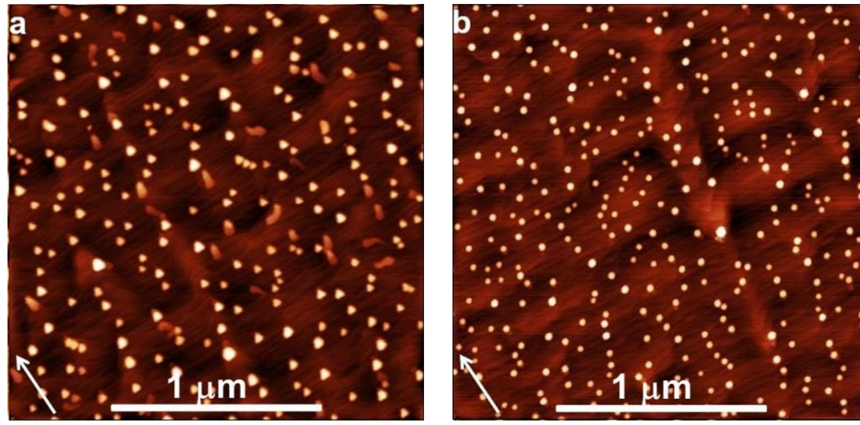

Figure 6.2. AFM topography images of (a) GaAs QDs (2×2 μm^2, sample D1) and (b) Ga droplets (2×2 μm^2, sample D2) grown on GaAs(111)A with 2° miscut toward $(\bar{1}\bar{1}2)$ at 350 °C. Arrows indicate $[\bar{1}\bar{1}2]$ direction perpendicular to steps.

The AFM images of the samples T1, T2, T4, T5 are reported in Figure 6.3. The droplets are randomly nucleated at the sample surface, with a higher probability at the terrace boundaries. The deposition temperature range drives the system in the complete condensation regime, due to the quenching of the Ga desorption[102].

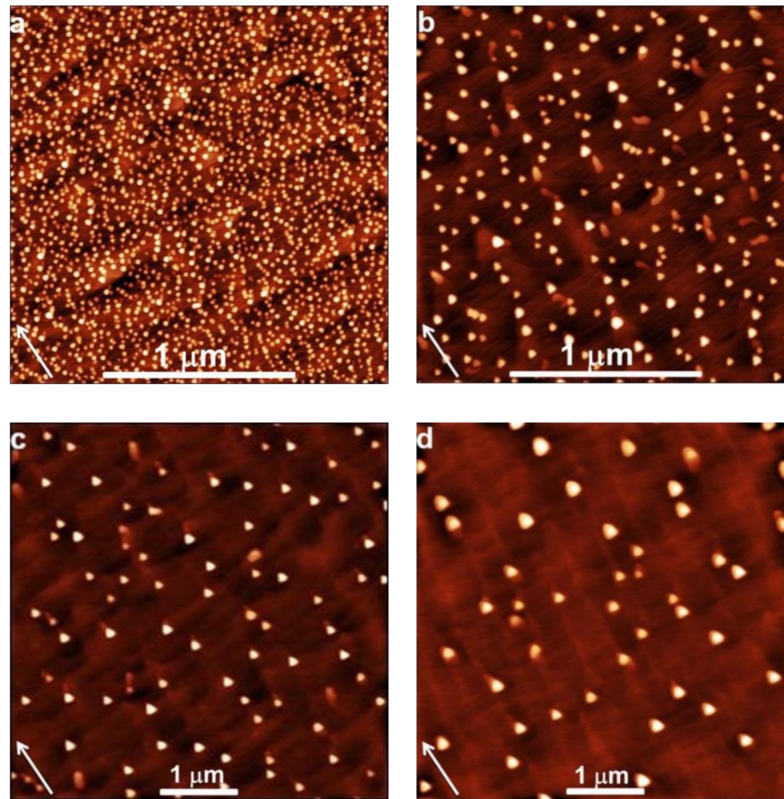

Figure 6.3. AFM topography images of GaAs QDs grown on GaAs(111)A with 2° miscut toward $(\bar{1}\bar{1}2)$ at (a) 300 °C (2×2 μm^2, sample T1); (b) 350 °C (2×2 μm^2, sample T2); (c) 450 °C (5×5 μm^2, sample T4); (d) 500 °C (5×5 μm^2, sample T5). Arrows indicate $[\bar{1}\bar{1}2]$ direction perpendicular to steps.

As expected, the droplet density *N* is a function of droplet deposition temperature *T* and Ga flux rate *F*. As mentioned in Chapters 3.3 and 5.1, from the classical nucleation theory the density of

droplet formed by diffusing adatoms on the surface, according to (3.16), is expected to vary with the law:

$$N(F,T) \propto F^{p} \cdot \exp\left(E_a / kT\right). \qquad (6.1)$$

The exponent p depends on the characteristics of the process of atom aggregation. The p parameter is a function of critical cluster size i and depends on the actual characteristics of the growth process[160]. E_a is a combination of a diffusion activation energy E_D and the nucleation energy of critical cluster E_i[85,102]:

$$E_a = pE_D + pE_i / i. \qquad (6.2)$$

Critical cluster size cannot be less than 1, for Ga droplets deposited on singular (001) and (111)A GaAs surfaces the critical cluster size was reported and equals two[139] and one[141], respectively. Previously we also determine i = 1-2 atoms for low temperatures below 400 °C and i = 4 for high temperatures in case of Ga droplet nucleation on singular GaAs(111)A.

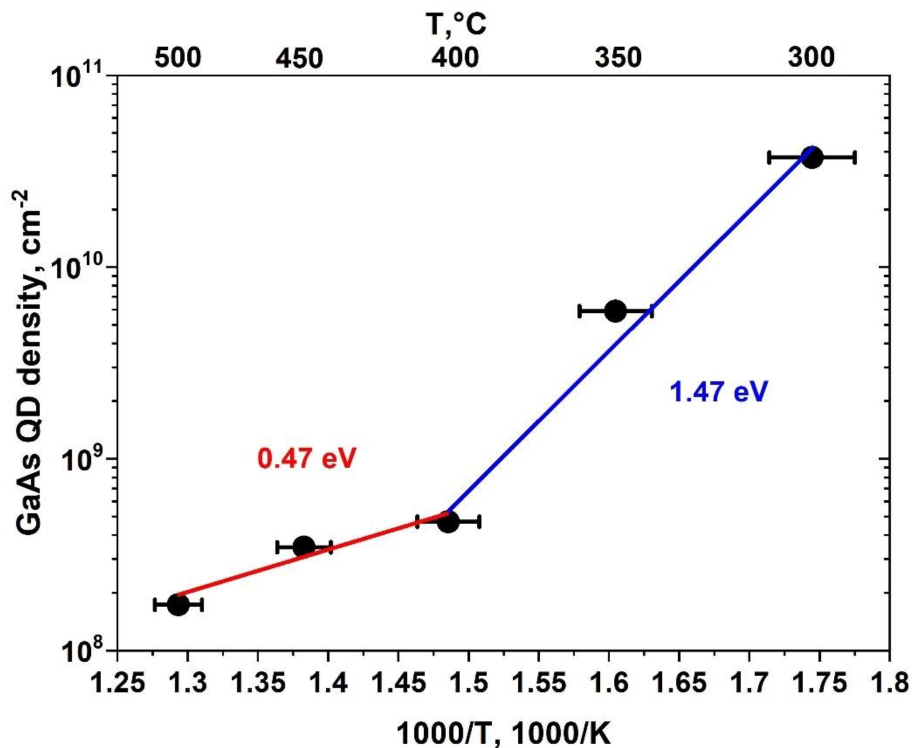

Figure 6.4. The density of GaAs QDs grown on GaAs(111)A with 2° miscut toward $\left(\bar{1}\bar{1}2\right)$ as a function of deposition temperature. 0.47 eV and 1.47 eV are activation energies for two different Ga droplet nucleation regimes.

As reported in Figure 6.4, with the increasing deposition temperature, droplet density decreases. A clear bend in the T dependence of N is observed around 400 °C. The activation energy changes value from E_a = 1.47 ± 0.10 eV at low temperatures to E_a = 0.47 ± 0.03 eV at high temperatures. Here the main error source in the activation energy determination is related to measure of the exact

deposition temperature. The presence of two temperature ranges with different activation energies in $N(F, T)$ has not been observed on singular (111)A surfaces[141,161,162] and, therefore, it is peculiar for vicinal surfaces.

Since E_i is the binding energy that is gained when i single adatoms form a cluster of the size i, in the first approximation the value of E_i depends linearly on the size of critical cluster, so the value E_i/i is a constant[141]. Thus, according to Equation (6.2), the change in the Arrhenius plot slope of N is related to a change in the energy E_d due to a temperature modification of the surface diffusion phenomena, or to a variation in the p parameter value. p can be independently determined via the dependence of N on F (see Figure 6.5). p equals 0.95±0.09, and 0.37±0.04 at 350 and 450 °C, respectively, thus showing that a relevant change in the nucleation process is occurring at ≈ 400 °C.

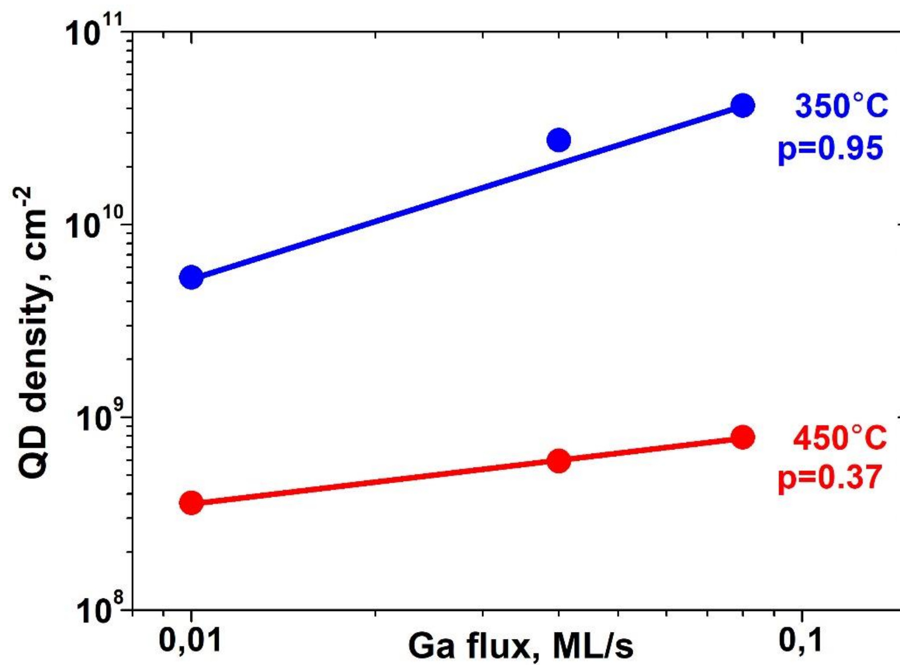

Figure 6.5. The density of GaAs QDs grown on GaAs(111)A with 2° miscut toward $(\bar{1}\bar{1}2)$ as a function of Ga flux rate. 0.95 and 0.37 are exponent parameter p of density dependence on Ga flux at 350 and 450 °C, respectively.

The surface reconstruction, as measured by RHEED, remains (2×2) in the whole temperature range showing that no change in the microscopic diffusion process and thus, in turn, of the diffusion activation energy happens at $T = 400$ °C.

Thus, the change with T in E_a is therefore related to the change in the p parameter. According to classical nucleation theory[85,102], p depends on i as:

$$p = \frac{i}{i+2}\,. \qquad (6.3)$$

A reduction in p is therefore related to a strong decrease in critical island size i. If the observed dependence of p on T is stemming from a temperature dependence of the critical island size i, it would require a change in critical island size, in order to justify the change of p of around a factor of 2.5 when temperature crosses $T = 400$ °C, from $i = 1$ at high T to $i \approx 40$ at low T, thus too steep and in the wrong direction (lowering the temperature usually stabilizes the nuclei) to be reasonable. Therefore, the decrease of p cannot be explained in terms of classical nucleation theory[85,102].

Influence of miscut substrate on diffusion behavior

According to[104], p depends on i and the diffusion environment:

$$p = \frac{i}{\gamma i + \gamma + 1}, \tag{6.4}$$

where γ is a parameter which indicated the dimensionality of the diffusion process. For two-dimensional isotropic diffusion, $\gamma = 1$. If the adatom diffusion is strongly anisotropic, thus rightfully considered one-dimensional, $\gamma = 2$. Any case of restricted adatom diffusion, e.g. in presence of impurities acting as obstacles, is characterized by a parameter $\gamma > 1$. So, the change in p is could be related o a change in the diffusion dimensionality, which affects the parameter γ.

A change in the dimensionality of the surface diffusion from two to one dimension may justify the reduction of a factor two of p at high T. Therefore, it is the utmost importance to independently determine the behavior of adatom diffusivity and the critical nucleus size i with deposition temperature on (111)A vicinal surface.

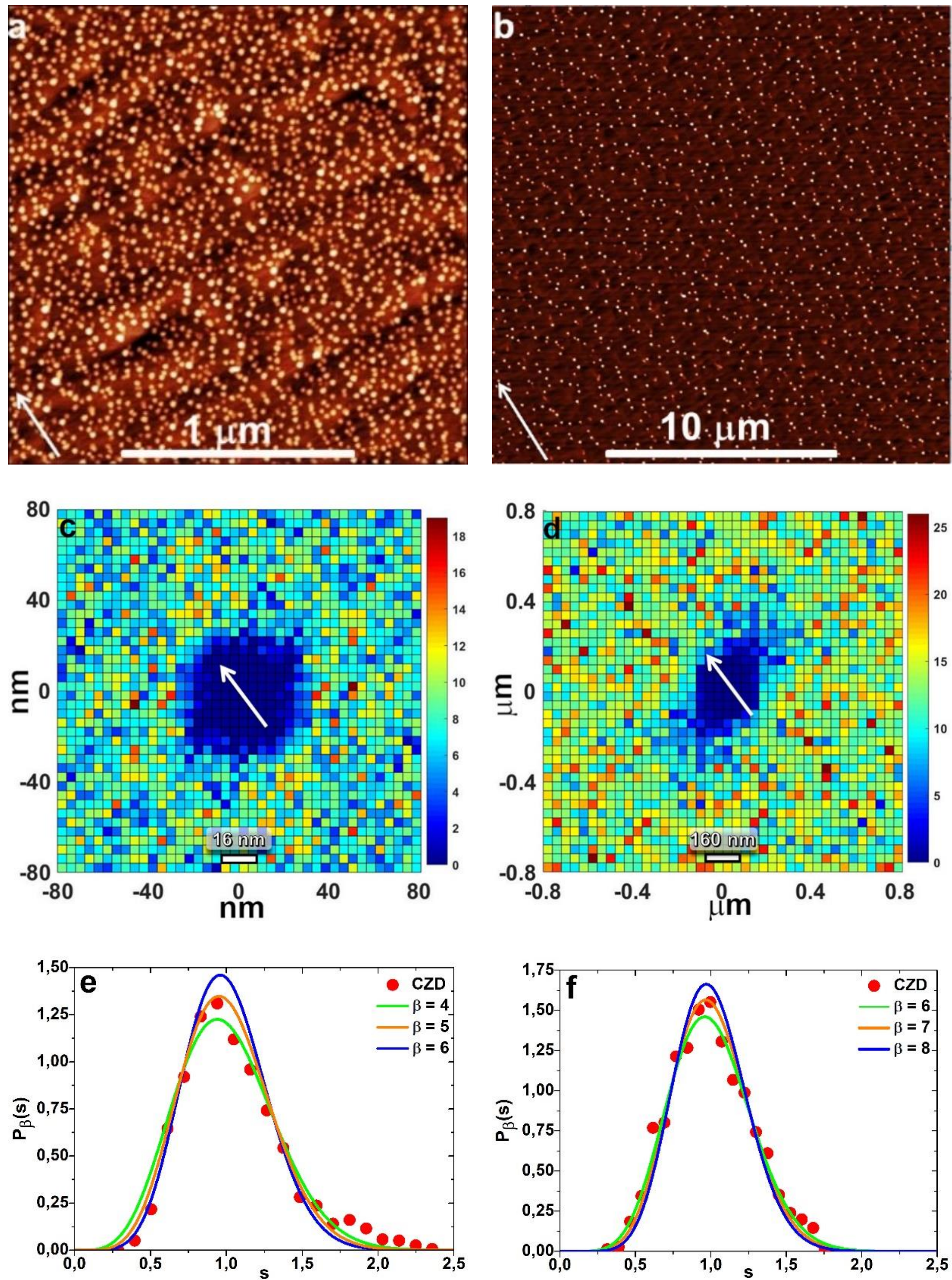

Figure 6.6. (a) AFM topography image of QDs grown on GaAs(111)A with 2° miscut toward $\left(\bar{1}\bar{1}2\right)$ at 300 °C (2×2 μm^2, sample T1), corresponding (c) spatial dispersion of neighboring QDs (0.16×0.16 μm^2) and (e) CZD obtained from voronoi tessellation, fitted by GWD. (b) AFM toppgraphy image of QDs grown on GaAs(111)A with 2° miscut toward $\left(\bar{1}\bar{1}2\right)$ at 450 °C (20×20 μm^2, sample T4), corresponding (d) spatial dispersion of neighboring QDs (1.6×1.6 μm^2) and (f) CZD obtained from voronoi tessellation, fitted by GWD. Arrows indicate $\left[\bar{1}\bar{1}2\right]$ direction perpendicular to steps.

Any change in the diffusivity behavior of the adatoms can be monitored through the spatial neighbor distribution of droplets (see Figure 6.6c, d). From these graphs it is possible to extract the average excluded zone around each droplet, which is due to the adatom density depletion stemming from the efficient adatom capture by the droplet within one diffusion length from the droplet itself. This makes the adatom density low enough to inhibit additional droplet nucleation in the area[160]. The excluded zone size and shape is then related to the actual adatom diffusion on the surface, and it permits to extract a qualitative dependence of this quantity at different deposition conditions. At $T < 400$ °C, the excluded area has a symmetrical, nearly hexagonal, shape (see Figure 6.6c), which shows no preferential direction for Ga adatom diffusion. The excluded zone radius is around 20 nm at $T = 300$ °C. This value corresponds approximately to two times the average terrace width. From AFM scans, we have observed that the droplets nucleate at the terrace steps, thus being able to collect adatoms from two contiguous terraces. The observed excluded zone radius thus stands for to a situation where the adatom, on average, can travel to the droplet without meeting a step. A clear transition in the shape of the excluded zone occurs around 400 °C. At $T > 400$ °C the excluded zone area becomes strongly asymmetrical, with a dimension along $\left[\bar{1}\bar{1}2\right]$ exceeding 60 nm and strongly elongated in the $\left[1\bar{1}0\right]$ direction, thus along steps. This behavior stems from the presence of a sizeable ES barrier at the step edge which hinders adatom diffusion across the steps[136]. In fact, the ES barrier corresponds to an additional energy needed for an adatom to jump across the terraces[163], which characterize the (111)A vicinal surface, and decreases the diffusivity in the $\left[1\bar{1}0\right]$ direction. Therefore, Ga adatoms at $T > 400$ °C predominantly migrate in the direction along steps in a strongly anisotropic way, this way approaching a quasi-one-dimensional diffusion behavior.

Capture zone distribution

An estimation of the critical cluster size i can be gained from the analysis of the capture zone (CZ) distribution[103,104] of the droplets. CZs can be determined from Voronoi cells. The CZs derived from the AFM images of the self-assembled droplet at 300 and 450 °C are reported in Figure 6.6e,f, respectively. The parameter β is related to the critical nucleus size i and to dimensionality of diffusion γ by $\beta = \gamma i + 1 + \gamma$.

The experimental normalized capture zone distribution has been obtained from CZ tessellations and have been fitted by generalized Wigner distribution (see Figure 6.6e,f). The fitted β equals 5±1 at 300 and 350 °C while β = 7±1 at 400, 450, and 500 °C. Thus, the measured β values correspond to, taking into account the two-dimensional adatom diffusion (γ = 1), critical nucleus

size $i = 3\pm1$ at $T < 400$ °C. At $T \geq 400$ °C, we observe a quasi-one-dimensional adatom diffusion behavior, so we fit with $\gamma \approx 2$. Then observed β value is consistent with $i = 2.0\pm0.5$. Therefore, according to GWD analysis, the critical cluster size i can be assumed the same in the whole measured T range and equal to $i = 2$. This means that three Ga atoms are sufficient to form minimal stable cluster on the vicinal GaAs(111)A surface. The same size for stable Ga cluster was previously demonstrated by *in-situ* STM during the growth on GaAs(001) substrate[164]. It is worth noticing that the i value, as determined by CZ analysis, qualitatively accounts for the observed values of p. From (6.4) the predicted scaling parameter for one dimensional diffusion at high T, calculated using $i = 2.0\pm0.5$ and $\gamma = 2$, $p_{HT} = 0.29\pm0.11$, and the ratio between the low T and high T values of p, $p_{HT}/p_{LT} = 1.72\pm0.65$, determined setting $i = 2$ and varying γ between its high and low T values, are within the errors of the experimental $p_{HT} = 0.37\pm0.04$ and $p_{HT}/p_{LT} = 2.57\pm0.52$.

6.2. In droplets on vicinal GaAs(111)A

Quantum networks require a long-distance communication, therefore for exploiting the optical fibers with low optical losses it is necessary to fabricate quantum sources mitting at telecom band range. Since lattice-matched GaAs/AlGaAs QDs systems emit at a wavelength in the 750 to 800 nm range[13,32,33], to shift an emission wavelength up to telecommunication bands (1.31 – 1.55 μm), it becomes necessary to adapt the heterostructure composition to allow for the emission in the required energy range. One possible way is to fabricate InAs QDs embedded in InGa(Al)As layers, pseudomorphically grown on InP substrates[165,166] or metamorphically grown on GaAs substrates[15,167–169]. Thus, we investigated indium islands self-assembly (the first step of InAs QD fabrication by DE technique) on vicinal GaAs(111)A substrates[170].

The temperature dependence of In island density

Firstly, we have studied an influence of the deposition temperature on the indium islands density, in order to determine suitable conditions for the fabrication of individual emitters. Indium islands were self-assembled on semi-insulating GaAs(111)A substrates with 2° miscut toward $\left(\bar{1}\bar{1}2\right)$.

After an oxide desorption at 590 °C for 5 min, a 130 nm GaAs buffer layer was deposited to smooth the surface. The substrate temperature T was varied from 30 to 395 °C. The temperature was calibrated by the desorption of native oxide and appearance of (2×2) reconstruction at 580 °C and by melting a piece of indium, attached to sample holder, at 156.6 °C. The total amount of indium supplied for the island formation was 2 ML, deposited with a growth rate of 0.04 ML/s. For one sample 1 ML of In was deposited at 80 °C, to check the influence of a deposited indium amount on the island density. During the indium deposition the background pressure was below 3×10^{-9} Torr. The supply of indium without As_4 enabled appearance of indium liquid droplets or indium

solid islands on the surface, depending on the deposition temperature. Every growth experiment was monitored in situ by RHEED.

Figure 6.7 shows AFM images of indium islands obtained on vicinal GaAs(111)A at different deposition temperature and the same In flux rate. From the nucleation theory of J. A. Venables[85,102] (described in Chapter 3.3), the density of stable clusters exponentially depends on the temperature: with decreasing the deposition temperature the density of stable clusters is increasing. The density dependence of Ga droplets and GaAs QDs self-assembled on GaAs(001)[139], on singular GaAs(111)A[141,161], and on vicinal GaAs(111)A[140], as well as In droplets and InAs QDs on GaAs(001)[171] and on InP(001)[114] satisfy the behavior described by the nucleation theory.

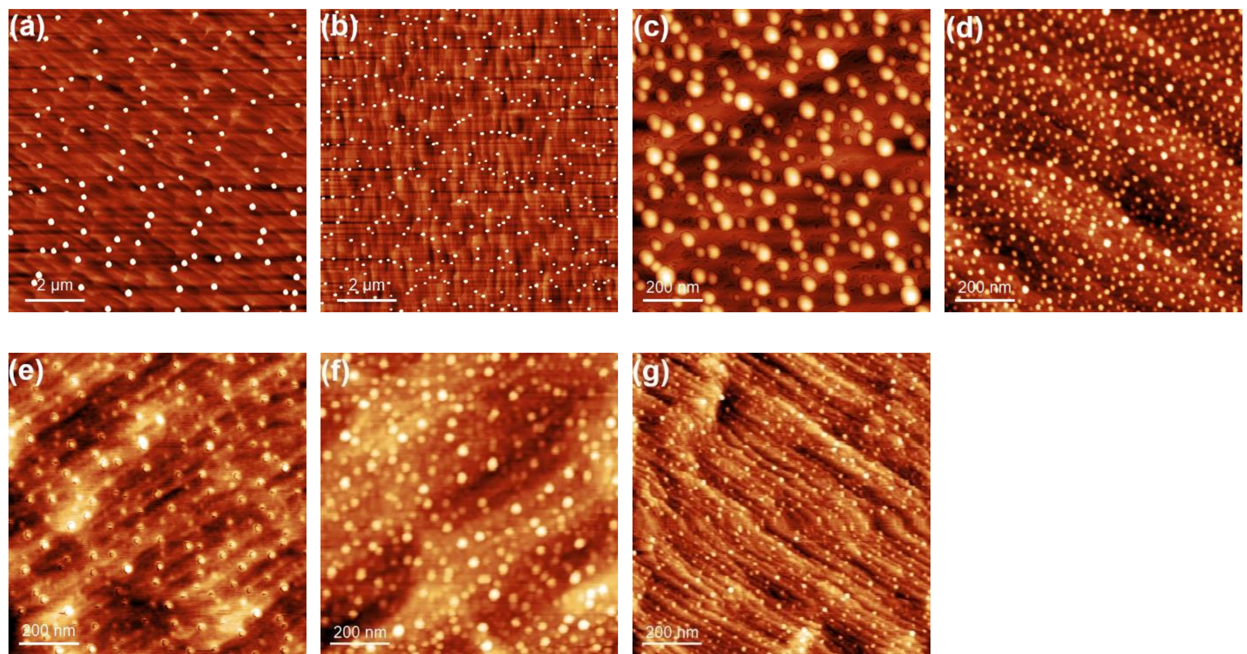

Figure 6.7. AFM topography images of indium islands, obtained by depositing 2 ML of indium on GaAs(111)A with 2° miscut toward $(\bar{1}\bar{1}2)$ at (a) 395 °C (10×10 μm²), (b) 370 °C (10×10 μm²), (c) 240 °C (1×1 μm²), (d) 160 °C (1×1 μm²), (e) 80 °C (1×1 μm²), and (f) 30 °C (1×1 μm²). (g) AFM topography image of indium islands, obtained by depositing 1 ML of In on GaAs(111)A with 2° miscut toward $(\bar{1}\bar{1}2)$ at 80 °C (1×1 μm²).

As it is clear from Figure 6.8, the density of indium islands self-assembled on vicinal GaAs(111)A displays a complex dependence on the deposition temperature. In the reported 30 – 395 °C temperature range, indeed, deviations from the monotonic increase of density with decreasing temperature predicted by the nucleation theory[85,102] is quite evident. The same behavior in the range of 100 to 200 °C is shown by In islands self-assembled on both on-axis and vicinal (111)A substrates (green stars and red circles, respectively, in Figure 6.8), thus excluding an origin related to the presence of the strong anisotropy in the adatom diffusion coefficient on vicinal substrates due to ES barrier at the step edges[140]. The temperature error bar in our measurements is associated with the accuracy of the substrate temperature determination by the thermocouple and equals

approximately ±5 °C. The temperature or density error bar is not presented, if it is less than the size of red circles or green stars.

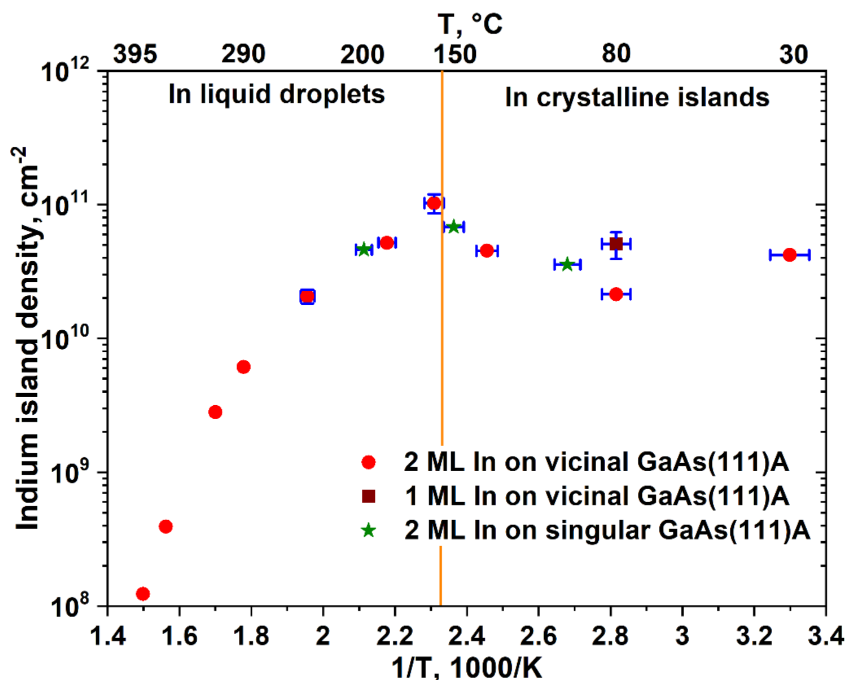

Figure 6.8. Temperature density dependence of self-assembled indium islands. Red circles correspond to 2 ML In deposited on vicinal GaAs(111)A with 2° miscut toward $(\bar{1}\bar{1}2)$; the brown square corresponds to 1 ML In deposited on vicinal GaAs(111)A 2° miscut toward $(\bar{1}\bar{1}2)$ at 80 °C; and green stars correspond to 2 ML In deposited on singular GaAs(111)A at 100, 150, and 200 °C. Temperature error is ±5 °C. The temperature or density error bar is not presented if it is less than the size of red circles or green stars. Orange line indicates the indium melting point (T_{In}^{melt} = 156.6 °C).

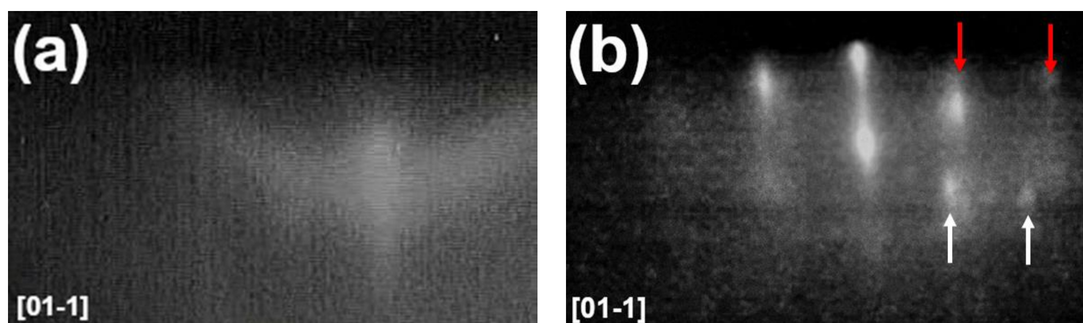

Figure 6.9. RHEED patterns of 2 ML In deposited on vicinal GaAs(111)A with 2° miscut toward $(\bar{1}\bar{1}2)$ at (a) 185 °C (halo pattern) and at (b) 80 °C (spotty pattern). Red arrows indicate RHEED reflexes from indium crystalline islands and white arrows indicate RHEED reflexes from GaAs.

Data in Figure 6.8 were conveniently analyzed by considering separately liquid droplets and solid nanocrystals. The RHEED diffraction pattern was monitored during the deposition to assess the indium island state. A halo pattern was observed at deposition temperatures of 160 and 185 °C (see Figure 6.9a), which confirms the self-assembly of liquid droplets on the surface at

temperatures above the In melting temperature $T_{In}^{melt} \approx 157$ °C. On the contrary, at temperatures below T_{In}^{melt}, a spotty pattern was observed (see Figure 6.9b), indicating the formation of epitaxial crystalline islands. It is worth mentioning that no indication of the formation of liquid droplets or solid islands can be obtained from RHEED at $T > 200$ °C, due to the low density of the formed islands and only (2×2) reconstruction of GaAs(111)A surface was observed during the deposition of indium.

RHEED analysis of In solid island formation

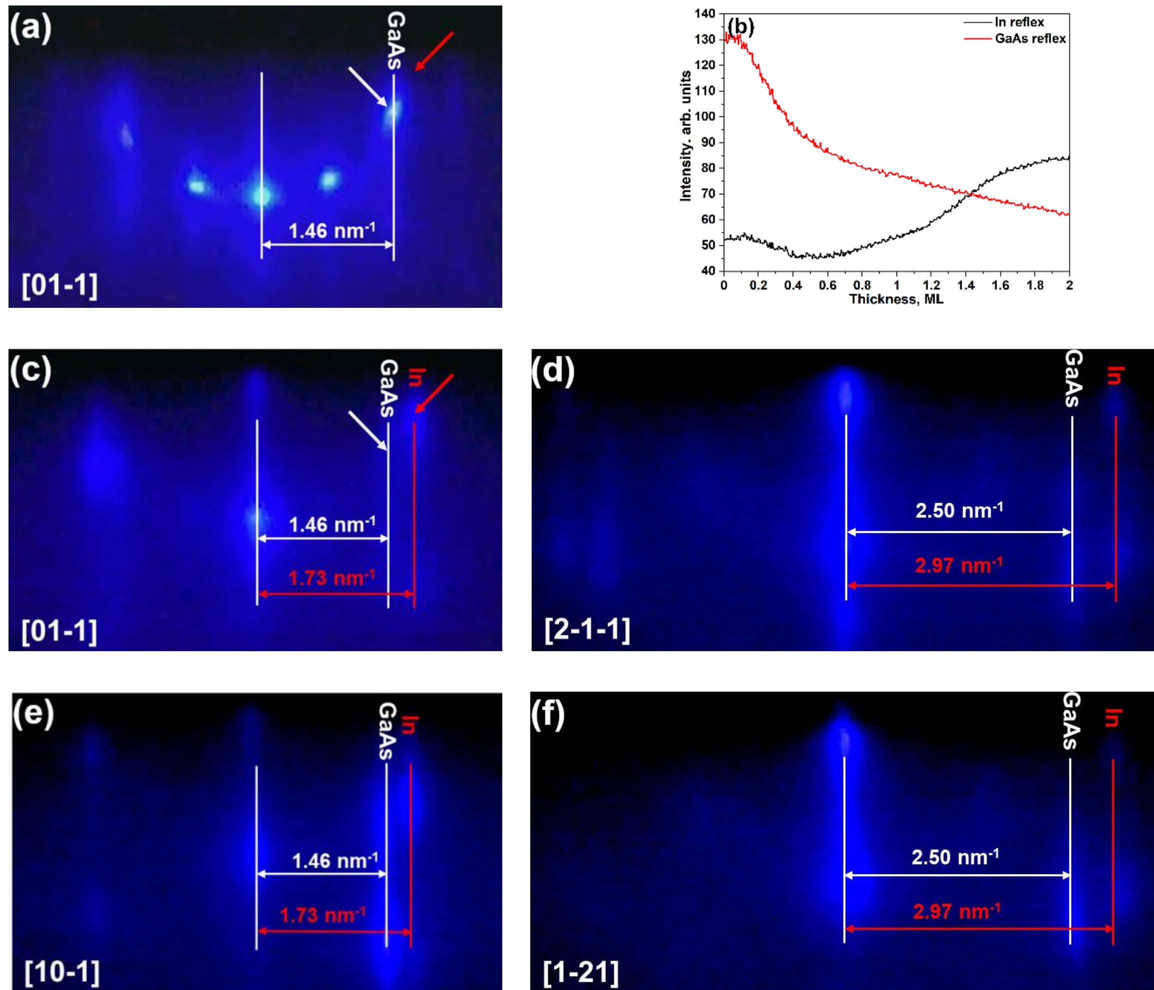

Figure 6.10. (a) RHEED pattern of GaAs buffer before the deposition of In. (b) The time dependence of the intensity of RHEED reflexes from GaAs and In taken along the $[01\bar{1}]$ azimuth. RHEED patterns along (c) $[01\bar{1}]$ (d) $[2\bar{1}\bar{1}]$, (e) $[10\bar{1}]$, and (f) $[1\bar{2}1]$ azimuths after the deposition of 2 ML In on vicinal GaAs(111)A with 2° miscut toward $(\bar{1}\bar{1}2)$ at 80 °C. Red and white arrows correspond to points where the intensity dependence of In and GaAs reflexes, respectively, on panel (b) was measured.

A detailed analysis of the RHEED patterns recorded during the deposition of In at 80 °C (see Figure 6.10) permits to assess the crystal structure and the lattice parameter of the indium crystalline islands. Before the indium deposition, only (2×2) - GaAs(111)A reconstruction was observed (Figure 6.10a). After the deposition of 2 ML In, the diffraction reflexes of (2×2)

reconstruction disappeared and (1×1) - GaAs(111)A reconstruction and additional spotty and elongated reflexes were observed in $\langle 1\bar{1}0 \rangle$ and $\langle \bar{2}11 \rangle$ azimuths (Figure 6.10c-f). The appearance of the additional spots shows that the indium islands are crystalline, but the growth is not pseudomorphic to the GaAs(111)A substrate. The calculated interplanar distances of In islands along each of the equivalent direction on (111) surface are the same (l_1 = 0.336±0.002 nm along $\langle 1\bar{1}0 \rangle$ and l_2 = 0.584±0.005 nm along $\langle \bar{2}11 \rangle$). Additionally, the ratio l_2/ l_1 equals 1.74±0.03 agrees with value $\sqrt{3}$ for a cubic crystal. This observation confirms that In islands, grown on vicinal GaAs(111)A substrate at 80 °C, have FCC crystal structure with lattice constant a_{In}^{FCC} = 0.475±0.003 nm.

Figure 6.10b shows RHEED intensity dependence of In and GaAs reflexes taken along the $\left[01\bar{1}\right]$ azimuth. The points where the intensity was measured are pointed by arrows on Figure 6.10a, c. The intensity of the In reflex at 0 ML is not zero because there is a diffusive background from GaAs surface reconstruction. The In reflex intensity decreasing up to ≈ 0.5 ML is related to drastic decreasing of GaAs reflex intensity and its diffusive background. After 0.5 ML, the In reflex intensity starts increasing while GaAs reflex decreases until the end of the 2 ML deposition. It is related to a nearly pseudomorphic state of initially small islands and/or to low sensitivity of RHEED technique.

Bulk indium has body-centered tetragonal (BCT) lattice. Any BCT lattice can be also represented as face-centered tetragonal (FCT) lattice, which, in the case of In has the following parameters: a_0 = 0.460 nm and c_0 = 0.495 nm at 300 K[172]. Considering thermal expansion[173], the FCT lattice constants at 80 °C (353.15 K) are a_0 = 0.466 nm and c_0 = 0.500 nm. A slight expansion of a_0-axis of 1.8% and a compression of c_0-axis by 5% results in transition from FCT to FCC lattice in agreement with our observation. FCC lattice of indium have been already observed for In nanoparticles (NPs)[172,174] and indium islands[175] with a lattice constant of 0.47 – 0.50 nm[172,174,175]. It is assumed that BCT-FCC transition occurs because of the surface tension with little volume dilatation at a small size of NPs. Thus, indium islands deposited on vicinal GaAs(111)A substrate at $T < T_{In}^{melt}$ are relaxed, with lattice constant that closely matches that of In FCC crystal.

Moreover, it is necessary to emphasize that BCT lattice of indium has a lattice mismatch with GaAs of ≈ 19%. It means that, evidently, the In/GaAs interface is such that a large portion of the big mismatch is accommodated by plastic deformation. Moreover, there is a residual strain, due to BCT-FCC transition.

Strain-induced reentrant behavior of In island density dependence

Our observations point that T_{In}^{melt} splits the island density temperature dependence into two zones (separated by a vertical orange line in Figure 6.8), namely, above T_{In}^{melt}, where the islands are liquid indium droplets, and below T_{In}^{melt}, where the islands are slightly strained, indium FCC nanocrystals.

In the liquid phase, the indium island density is increasing with decreasing temperature. Despite the behavior being simple, it is worth noting that the indium island density deviates from the single exponential law predicted by straightforward application of nucleation theory[85,102], showing reduced activation energy at T < 300 °C with respect to the higher temperature values. Such behavior is attributed to the diffusive movement of small droplets clusters which may contribute to the subsequent coalescence of small metal clusters, which reduce the number of islands on the surface[139,141,176].

As the temperature is lowered and solidification takes place, the density dependence on temperature completely changes behavior. At first, a surprising decrease with decreasing temperature is observed until, at even lower temperatures (≈ 80 °C), another drastic change in slope takes place bringing back the temperature dependence of the island density to the expected increase with decreasing temperature.

At sufficiently low temperature the density of islands grows with decreasing temperature (extreme right portion of Figure 6.8) and it is a direct consequence of reduced diffusion length of In adatoms[139,141,161]. The island density, after reaching a minimum approximately 80 °C, increases by increasing the temperature until T_{In}^{melt}. Interpreting such behavior in the island density vs. temperature dependence using standard nucleation theory is impossible. Within this approach possible sources of the activation energy change (the slope in the log(island density) vs. $1/T$) could be linked to an increase/decrease of the critical nucleus size or to a non-monotonic change of the adatom diffusivity, which could suffer below the In solidification temperature[85,102]. Both explanations are, however, hardly justifiable as the change of the critical nucleus is not expected and no transition in surface reconstruction of the GaAs surface is observed at T_{In}^{melt} to explain a different adatom diffusivity. Nevertheless, within the nucleation theory approach[85,102], the activation energy can change the value but cannot change the sign and become negative.

Here, we point out that the observed behavior could be justified by the onset of a coarsening process, active when the islands are solid and not when they are in the liquid phase. Large mass transfer between islands would reduce the measured island density, with respect to the one expected based on critical nucleus size and diffusivity. A fingerprint of its presence can be gained

by the analysis of the size distribution of islands (see Figure 6.11), as a sizable broadening of the distribution is expected in the case of active coarsening phenomena. In fact, the island ensemble distribution clearly broadens, with the full width at half maximum (FWHM) of normalized (to mean size) lateral size distribution of In islands, passing from 0.8 at 160 °C (Figure 6.11a) to 1.5 at 30 °C (Figure 6.11c). It is worth mentioning that a broadening of the island size could originate from a reduction of the critical nucleus size, but it should be accompanied by a concurrent increase of the island density[103]. As island coarsening is intrinsically a kinetic effect, as originating from island to island mass transfer, to provide and additional proof of its presence we grew a sample (see Figure 6.7f) at the same temperature and flux of the one (see Figure 6.7e) resulting in the maximum deviation (T = 80 °C), but reduced the deposition time by one half (brown square in Figure 6.8). The island density increases, thus showing that the reentrant behavior of the island density is caused by a kinetically controlled coarsening effect.

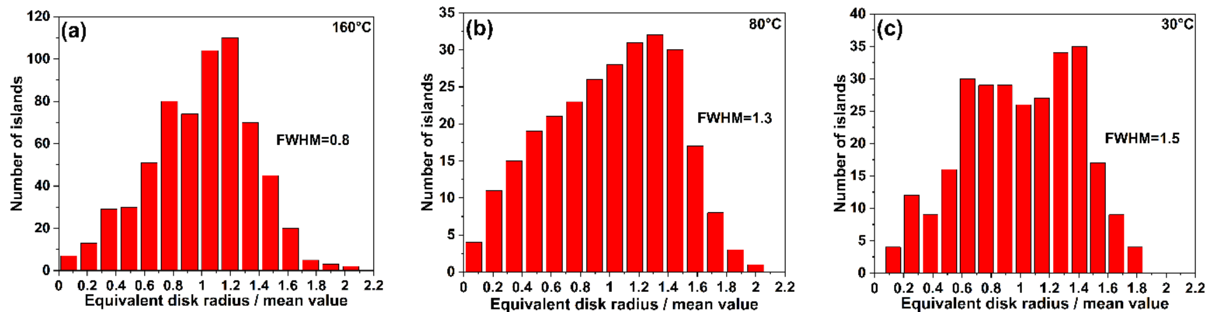

Figure 6.11. Size distributions of indium islands normalized to their mean size at (a) 160 °C, (b) 80 °C, and (c) 30 °C calculated from 1×1 μm² AFM scans of each sample. The mean equivalent disk radius for (a) is 8.5±3.0 nm, (b) 9.7±4.1 nm, and (c) 10.6±4.1 nm.

The presence of an effective mass transfer when the islands are in the solid phase and not in the liquid phase could be traced back to the residual strain in the In crystalline islands. Strain and its local relaxation are powerful physical phenomena which control the interaction between neighboring islands, thus affecting the self-assembly island dynamics and statistics[177]. Above T_{In}^{melt} the islands are constituted by indium droplets. The liquid state of the droplets makes them able to accommodate any strain. Therefore, it is reasonable to not expect any change in the island density and statistical distribution within the droplet ensemble related to the presence of strain. A completely different scenario is expected when the islands are crystalline. In the crystal phase, the strain can be accommodated via an enhancement of the height to base ratio of the islands, which allows for strain relaxation[178–180]. As the volume of the island increases, a large height to base ratio allows for a stronger strain relaxation. However, it also requires a large cost in terms of the surface energy[177]. Therefore, in an island growing in volume, after a critical size is reached, insertion of a dislocation within the island lowers the need for strain relaxation[180], because the dislocation induced strain relaxation strongly reduces the chemical potential of the dislocated crystalline

islands with respect to the islands without a new additional dislocation. Moreover, coarsening in the island ensemble is expected[181]. The dislocated island increases in volume at the expenses of the neighboring islands lying within an indium adatom diffusion length. This phenomenon was reported in several experiments on island formation in the presence of strain[182] (see, e.g., Figure 6.12). The net effect of the strain reduction by dislocation insertion, observed in the solid In islands, should be then the onset of a strong mass transfer effect that results in the reduction of the island density as the island volume exceeds the critical volume, with respect to the purely pseudomorphic islands case, as those islands which are close to a dislocated one disappear due to the strong mass transfer. As discussed in the analysis of the RHEED patterns, we have evidence that the solid In islands are not pseudomorphic, with a nearly completed strain relaxation. Thus, supporting the interpretation of an origin of the coarsening effect as due to dislocation induced changes in the chemical potential of the islands.

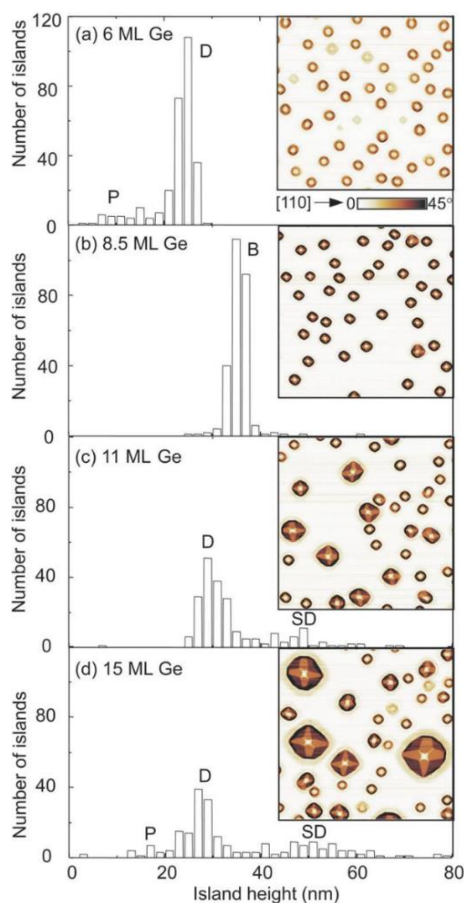

Figure 6.12. Histograms of the island height for different samples containing (a) 6 ML Ge, (b) 8.5 ML Ge, (c) 11 ML Ge and (d) 15 ML Ge deposited at 700 °C on Si(001). Different island shapes are labeled as P – pyramid, D – dome, B – barn, and SD – superdome. The corresponding AFM images 2 μm×2 μm are shown in the insets. Size distribution broadens essentially due to coarsening effect[182].

Conclusions

The presence of a sequence of parallel steps and terraces which characterizes the surface of vicinal GaAs(111)A substrates strongly affect the nucleation process of the Ga droplets, formed as precursors of GaAs QDs in DE growth procedure. A crossover between two different diffusion regimes with different dimensionality, occurs at $T = 400$ °C in case of 2° miscut toward $\left(\bar{1}\bar{1}2\right)$. Two-dimensional isotropic diffusion characterizes the low T regime. At $T > 400$ °C, the diffusion becomes highly anisotropic, elongated in the $\left[1\bar{1}0\right]$ direction, thus showing that diffusion is hindered by the presence of steps and mainly happens along the terraces. The anisotropy in the adatom diffusivity is the outcome of a sizeable ES barrier, which increases the energy barrier of diffusion across the steps. This crossover has large effects on the droplet density dependence on T and F. The critical parameter p and activation energy E_a undergo to a reduction of a factor two crossing the critical temperature of the crossover. This means a mild dependence of N on the actual growth parameter, thus limiting the droplet density, and the DE-QD engineering opportunities. CZ distribution analysis, which permits to extract the critical droplet size, shows that i equals 2, meaning three Ga atoms are sufficient to form a stable nucleus. This observation appears to be independent on substrate orientation and diffusion dimensionality.

We have shown that In islands deposited on GaAs (111)A substrates, both nominal and vicinal with 2° miscut toward $\left(\bar{1}\bar{1}2\right)$, display a complex non-monotonic dependence in terms of density vs. temperature. The usual behavior, well described by nucleation theory[85,102], is maintained only until the islands remain in the liquid phase (above T_{In}^{melt} ~160 °C). When the islands crystallize, coarsening phenomena take place, leading to broadening of the island distribution and to a reduction in the island density. At lower temperature (below 80 °C), islands density increases again is due to the reduction of the diffusion length which limits the range of mass transfer phenomena. The origin of the coarsening effect active only in the solid phase could be related to the presence of strain and strain relaxation in the epitaxial In islands which activates a strong mass transfer between islands. From RHEED observations, indium solid islands grown at 80 °C have FCC structure with lattice constant a_{In}^{FCC} = 0.475±0.003 nm.

Chapter 7. Telecom InAs QDs on GaAs(111)A vicinal substrates

To have QDs emitting at telecom wavelength it is necessary to use direct-bandgap semiconductor materials with the bandgap below 0.8 eV. One of the III-V semiconductor which may satisfy such requirement is InAs with the bandgap of 0.35 eV at 300K and about 0.42 eV at the temperature of liquid He. Unfortunately, InAs QDs embedded in a GaAs matrix emit at a wavelength about 1 μm[134,183,184] due to lattice mismatch between GaAs and InAs (about 7%, , which affect both the bandgap (compression leads to bandgap increase) and the maximum size of coherent islands).

Therefore, to shift an emission to higher wavelengths and to improve the crystal quality it is necessary to adapt the heterostructure composition. There are several approaches: the use of strain-reducing layers[43,185] or the fabrication of QDs embedded in the layers, metamorphically grown on the lattice-mismatched substrate, to reduce the strain between QD and barrier layer or/and the energy of barrier layer[167]. Metamorphic buffer layer (MMBL) approach was successfully used to shift the InAs QD emission to telecom band (1.31 – 1.55 μm)[15,167–169,186–188].

7.1. Metamorphic growth of InAlAs buffer layer

The term "metamorphic epitaxial material" describes a single-crystal thin film on a single-crystal substrate, where the film and substrate have a significant structural difference. This difference is often the relative lattice constants of the film and substrate but can also include film/substrate materials with different unit cells. The term metamorphic is similar to the geological and biological designation indicating a "change in form", because there is indeed a change in the material structure due to the elastic strain relaxation and plastic deformation processes that occur during the growth process[189].

The realization of a InAl(Ga)As MMBL with a high crystalline quality and a flat and smooth surface on GaAs(111)A substrate is made complex by the actual atomic surface configuration of the surface. To obtain near fully relaxed InAl(Ga)As layer on singular GaAs(111)A substrates T. Mano *et al.*[187,190] inserted a thin InAs interlayer between the substrate and MMBL. A drastic relaxation occurs due to an introduction of misfit dislocations at the InAs/GaAs interface during the growth of InAs on GaAs(111)A[191,192]. It was found that optimal thickness of InAs interlayer is 3 – 7 ML, otherwise the crystal quality and/or the surface morphology of the InAl(Ga)As MMBL become worst. Nevertheless, even if InAs layer is not optimized, the InAs interlayer is elastically deformed by growing InAl(Ga)As layer on the top together with the dislocation density change at the InAs/GaAs interface. As a result near strain-free metamorphic InAl(Ga)As layer can be formed on singular GaAs(111)A[187,190].

Sample	MMBL	In deposition	Annealing in As atmosphere	Capping layer	Comments
A	$In_{0.52}Al_{0.48}As$ 470 °C, 100 nm	–	–	–	From XRD analysis: In content = 52.0±0.4%
B	$In_{0.52}Al_{0.48}As$ 470 °C, 100 nm	–	–	–	Insertion of 3 ML InAs interlayer
C	$In_{0.6}Al_{0.4}As$ 470 °C, 100 nm	–	–	–	RMS = 0.43 nm from 1×1 μm^2 AFM scan
D	$In_{0.6}Al_{0.4}As$ 470 °C, 200 nm	370 °C, 1 ML	370 °C, 5×10^{-5} Torr	–	QD density = 2.52×10^{8} cm^{-2}
E	$In_{0.6}Al_{0.4}As$ 470 °C, 200 nm	370 °C, 2ML	370 °C, 5×10^{-5} Torr	–	QD density = 2.50×10^{8} cm^{-2}
F	$In_{0.6}Al_{0.4}As$ 470 °C, 200 nm	370 °C, 1 ML	370 °C, 5×10^{-5} Torr	$In_{0.6}Al_{0.4}As$ 10 and 140 nm at 370 and 470 °C	FSS = 15 – 100 μeV
G	$In_{0.6}Al_{0.4}As$ 470 °C, 200 nm	370 °C, 2 ML	370 °C, 5×10^{-5} Torr	$In_{0.6}Al_{0.4}As$ 10 and 140 nm at 370 and 470 °C	FSS = 55 – 120 μeV

Table 7.1. Layer structure and growth parameters of the samples presented in this work.

In present work same $In_{0.52}Al_{0.48}As$ composition has been chosen, in order to compare with[187] a possibility to grow metamorphic InAlAs layer on vicinal GaAs(111)A substrate with 2° miscut toward $(\bar{1}\bar{1}2)$. The sample growth description is presented in Table 7.1. We found that already 100 nm InAlAs layer, directly grown on vicinal GaAs(111)A substrate, is almost fully relaxed. Figure 7.1a displays X-ray diffraction (XRD) two-dimensional reciprocal space map for (333) symmetric Bragg reflection of sample A. It shows two diffraction peaks that originate from GaAs and $In_{0.52}Al_{0.48}As$. The peak position analysis suggests the indium content in InAlAs layer to be 52.0±0.4%.

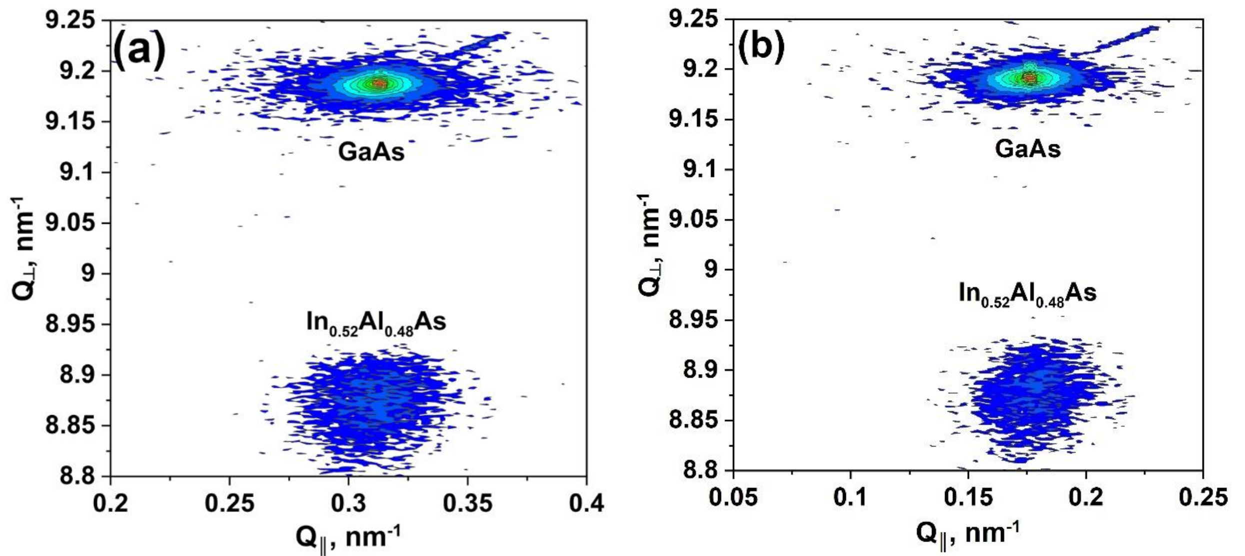

Figure 7.1. XRD two-dimensional reciprocal space map, taken near (333) symmetric Bragg reflection of (a) sample A and (b) sample B.

The insertion of a thin InAs interlayer between the substrate and InAlAs MMBL does not change a metamorphic state of the subsequent InAlAs buffer layer. Peak position of $In_{0.52}Al_{0.48}As$ on XRD reciprocal space map of Sample B is the same as for Sample A (see Figure 7.1b). Moreover, the appearance of large islands with the average lateral size and height of 602±69 and 17.8±4.9 nm, respectively, and with a density about 7×10^{6} cm^{-2} is observed for that sample (see Figure 7.2). Such islands can become nucleation sites for droplets and non-radiative recombination centers during the subsequent growth of the QD active layer. Therefore, the structure of InAlAs MMBL without insertion of thin InAs layer is chosen for following DE QD fabrication.

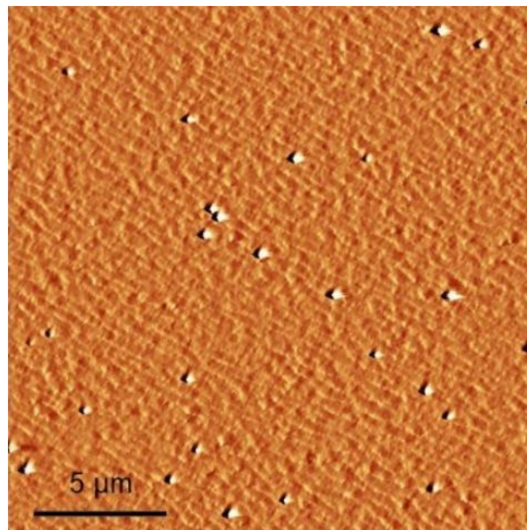

Figure 7.2. 20×20 μm^2 AFM amplitude image of sample B.

To find InAlAs barrier layer content for InAs QD emission at telecom band we perform a quantum mechanical 8-band k•p model calculation. From the pseudopotential theory calculation[193], considering only biaxial strain the InAs bandgap (the energy between conduction and heavy hole bands) is almost constant depending on the compression strain (see Figure 7.3). Thus, to calculate more accurately the bandgap of InAs QDs it is necessary to take into account hydrostatic strain emerging at capped QDs[184,194].

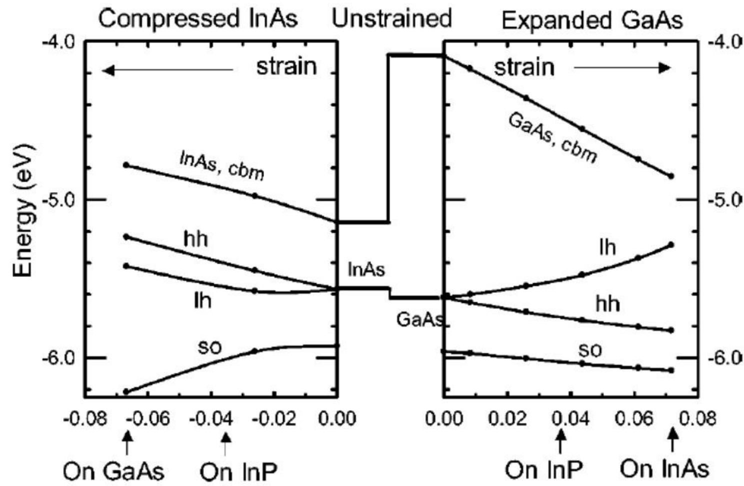

Figure 7.3. Local density approximation (LDA)-calculated strain-modified eigenvalues of epitaxially compressed InAs (on GaAs or InP(001) substrates) and epitaxially expanded GaAs (on InP or InAs)[193].

The calculation was carried out using multiscale simulation tool TiberCAD[195] for the simulation of electronic and optoelectronic semiconductor nanodevices, which allows to include any kind of strain (biaxial or hydrostatic). InAs QD has been modeled as truncated pyramid with regular triangular base and a small aspect ratio – height to width ratio (see Figure 7.4a). As presented below, the actual aspect ratio of our InAs QDs is about 0.05. InAs QD is surrounded by strain relaxed InAlAs area. The simulation suggests using Al content in InAlAs layer below 50% and the thickness of QD more than 4 nm (see Figure 7.4b). Thus, $In_{0.6}Al_{0.4}As$ barrier layer was chosen for subsequent QD fabrication. Additionally, the growth of InAlAs layer with such In content significantly reduces strain between barrier layer and InAs QDs, which decreases a number of misfit dislocation in the InAs/InAlAs interface improving the QD optical properties.

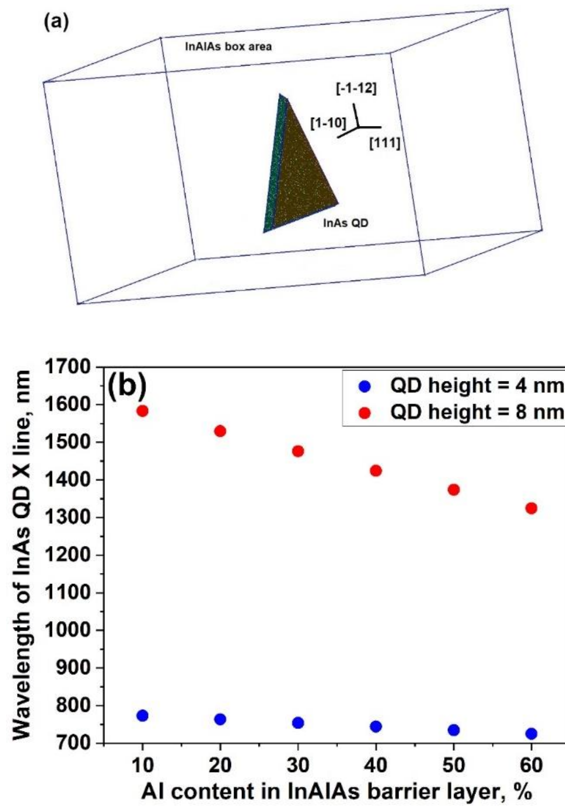

Figure 7.4. (a) The shape of InAs QD inside strain relaxed InAlAs box modeled in quantum calculation. [111] is the growth direction, $\{11\bar{2}\}$ are directions from the center of regular triangle base to the vertices of triangle. (b) Dependence of InAs QD emission wavelength on Al content in InAlAs barrier layer and the height of QD.

Smoothing the barrier layer surface

Then it was necessary to find a growth conditions to have the smooth $In_{0.6}Al_{0.4}As$ surface for In droplet deposition. The surface roughness was investigated depending on the growth temperature in the range of 450 – 510 °C and the growth rate in the range of 0.3 – 0.7 ML/s. The results are presented in Figure 7.5. The optimal conditions to have smooth surface are low growth temperature (450 – 470 °C) and high growth rate (0.5 – 0.7 ML/s). At these conditions the smooth surface is achieved by the suppression of surface diffusion and desorption of In adatoms, since the Al adatom diffusion and desorption at such temperature are very low. When diffusion desorption of In adatoms are not suppressed (at high growth temperature and low deposition rate) a rough surface due to step bunching is observed. The height of the step bunching for profile 2 is 12 nm, which corresponds to approximately 36 ML steps. Step bunching on the smoothest InAlAs surface is also observed, but the number of bunched steps is much less. Profile 1 shows the height of the step bunching of 2.2 nm (~ 7 ML steps).

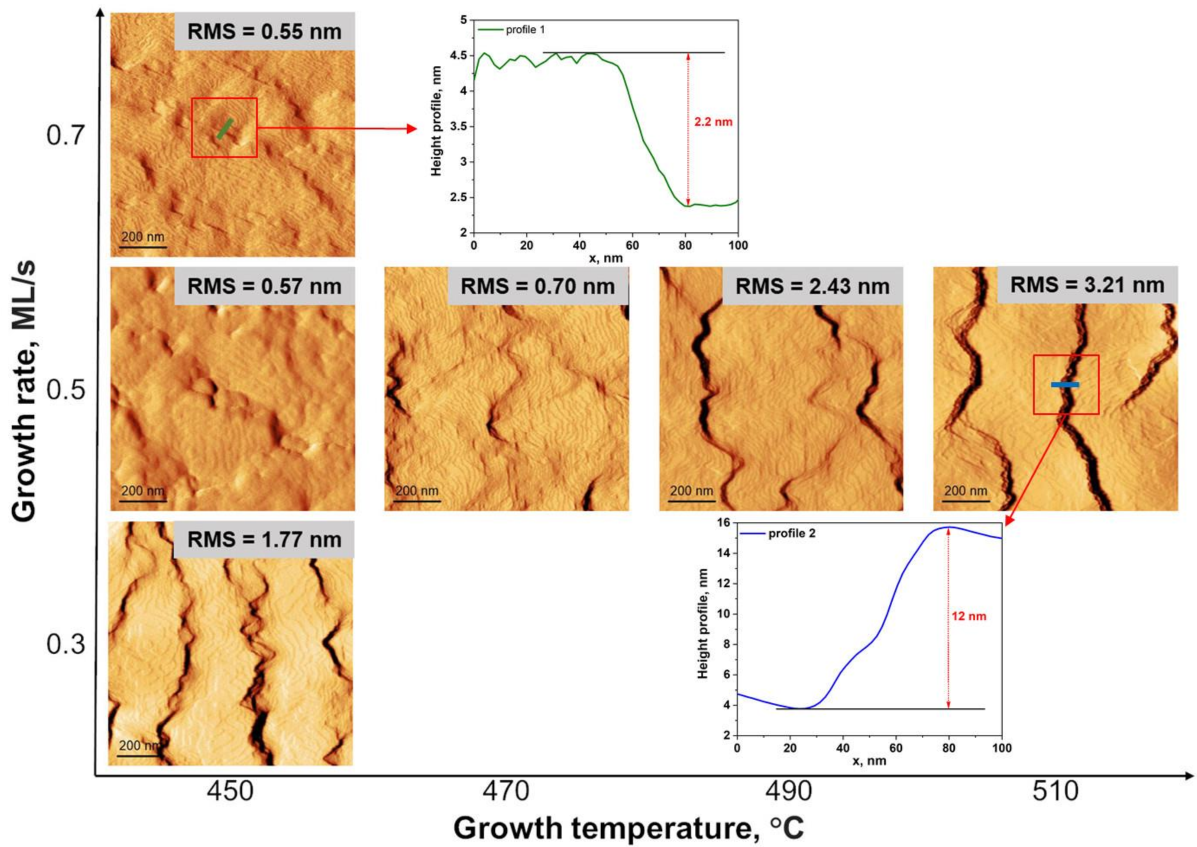

Figure 7.5. Growth conditions (the deposition temperature and the growth rate) effect on the surface roughness of 100 nm $In_{0.6}Al_{0.4}As$ directly grown on vicinal GaAs(111)A with 2° miscut toward $(\bar{1}\bar{1}2)$. Arrows indicates AFM height profiles taken along green and blue lines.

Threading dislocation density

In metamorphic systems, there is, in principle, no limit to the degree of lattice mismatch that can be accommodated. Early studies in this area found that misfit dislocations that accommodate the lattice mismatch between an epitaxial layer and substrate often generate threading dislocations[196,197]. Threading dislocation density (TDD) is generally determined by the kinetics of dislocation nucleation and glide, as threading dislocation segments contribute relatively little to strain relaxation; threading dislocations are often nearly vertical, and the amount of strain relieved by a dislocation is proportional to its length projected onto the interface plane. Since they act as nonradiative recombination centers, contributing to carrier scattering, and creating spatial inhomogeneities that can lead to early device failure, one of the most important metrics for metamorphic epitaxial materials is a low TDD[189].

Thus, another goal was to check the number of threading dislocations of InAlAs layer grown at these conditions. There are several techniques used to calculate the amount of dislocations threading the epitaxial layer. The first is transmission electron microscopy (TEM)[197,198]. However, it is very time-consuming technique due to special preparation of samples as well as there is not

so much amount of TEM due to their expensive price and the complexity of its maintenance. The second approach is XRD technique[192,198]. Nevertheless, results of the work[192] show that narrower (broader) peaks in X-ray rocking curves are not necessarily an indication of lower (higher) density of threading defects in heteroepitaxial layers. And the third is simpler and fast etch pit density (EPD) approach[190,198,199]. When the etch solution is applied on the surface, the etch rate is increased in places where threading dislocations comes out the crystal resulting in pits. The dislocation density can be estimated by counting the number of spots (pits) in a fixed area of AFM or optical microscopy image.

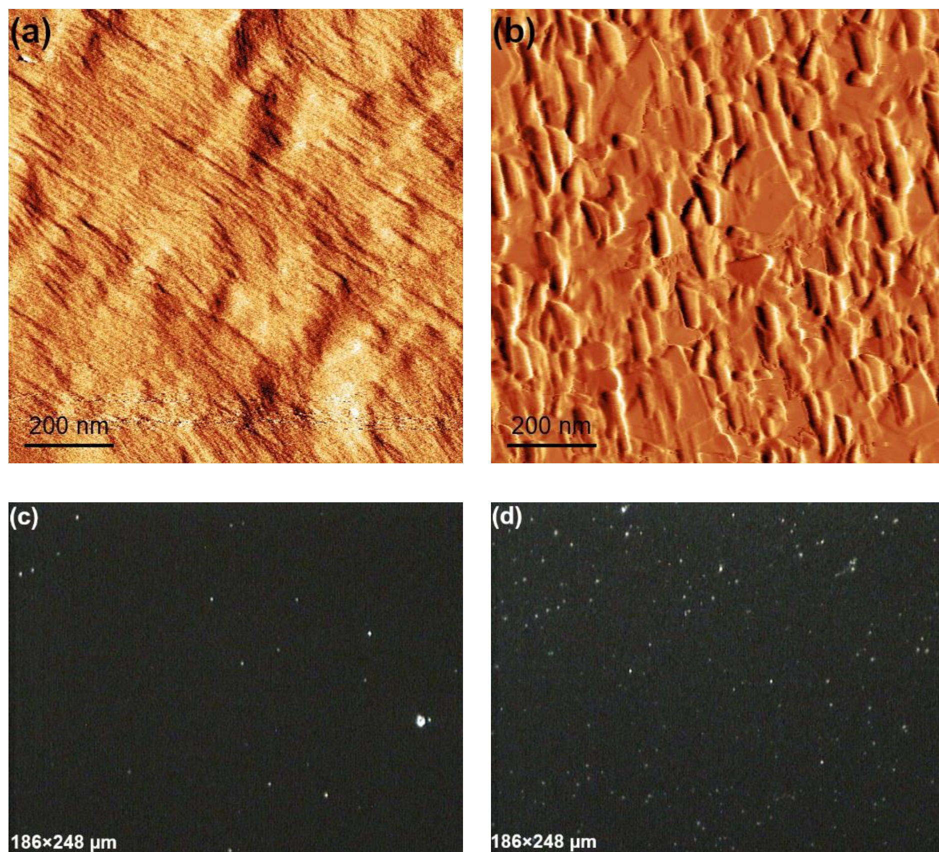

Figure 7.6. (a) 1×1 μm^2 AFM amplitude and (c) 186×248 μm^2 Nomarski microscope images of the sample with 100 nm $In_{0.6}Al_{0.4}As$ layer grown on vicinal GaAs(111)A before etching. (b) 1×1 μm^2 AFM amplitude and (d) 186×248 μm^2 Nomarski microscope images of the same sample after wet etching by HNO_3:H_2O (1:3) solution for 1 min at room temperature.

The wet etching solution for InAlAs layers was not found, but for InGaAs layers it is possible to use HNO_3:H_2O (1:3) solution for 1 min at room temperature[190]. We applied this solution to 100 nm $In_{0.6}Al_{0.4}As$ layer grown on vicinal GaAs(111)A and no etching pits was observed for that sample (see Figure 7.6). Thus, we decided to apply the solution to InGaAs layer with the same In content of 60% grown on vicinal GaAs(111)A, considering that InGaAs and InAlAs layers with the same In content have the same lattice mismatch with GaAs substrate and, in the first approximation, same strain relaxation behavior and the density of threading dislocations. Still some differences

can be present due to the different growth dynamics of InAlAs and InGaAs layers (like different bond strength), but we except that this effect is negligible. Figure 7.7 shows AFM and optical Nomarski microscopy images of the sample with 100 nm $In_{0.6}Ga_{0.4}As$ layer grown on vicinal GaAs(111)A before and after applying the above-mentioned wet etching solution. The EPD are about 1.1×10^7 and 1.2×10^7 cm^{-2} measured by AFM and Nomarski microscope, respectively. Such level of TDD is not the lowest value but it is satisfying for our goal since the desired density of InAs QDs is about 10^8 cm^{-2}, thus, only 1 of 10 dots will be placed close to dislocation.

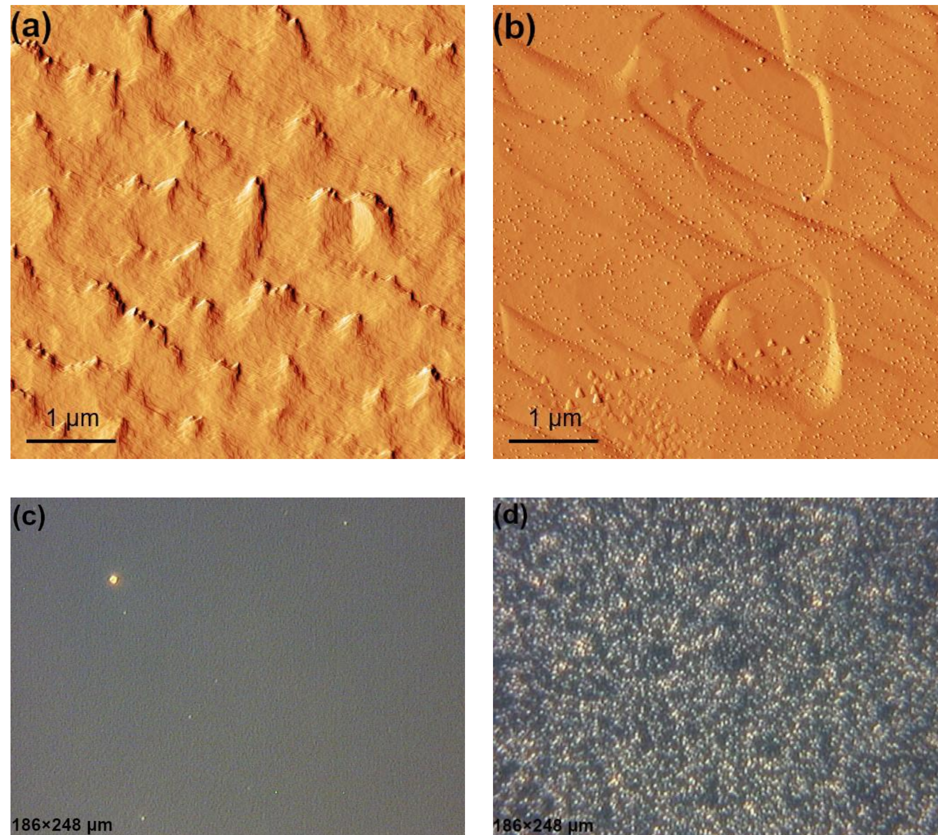

Figure 7.7. (a) 5×5 μm^2 AFM amplitude and (c) 186×248 μm^2 Nomarski microscope images of the sample with 100 nm $In_{0.6}Ga_{0.4}As$ layer grown on vicinal GaAs(111)A before etching. (b) 5×5 μm^2 AFM amplitude and (d) 186×248 μm^2 Nomarski microscope images of the same sample after wet etching by HNO_3:H_2O (1:3) solution for 1 min at room temperature.

Finally, to confirm the correspondence between EPD and TDD the etching solution was applied to GaAs(111)A vicinal substrate (see Figure 7.8). The measured EPD is about 1×10^3 cm^{-2} whereas the EPD $\leq$ 500 cm^{-2} from the substrate description.

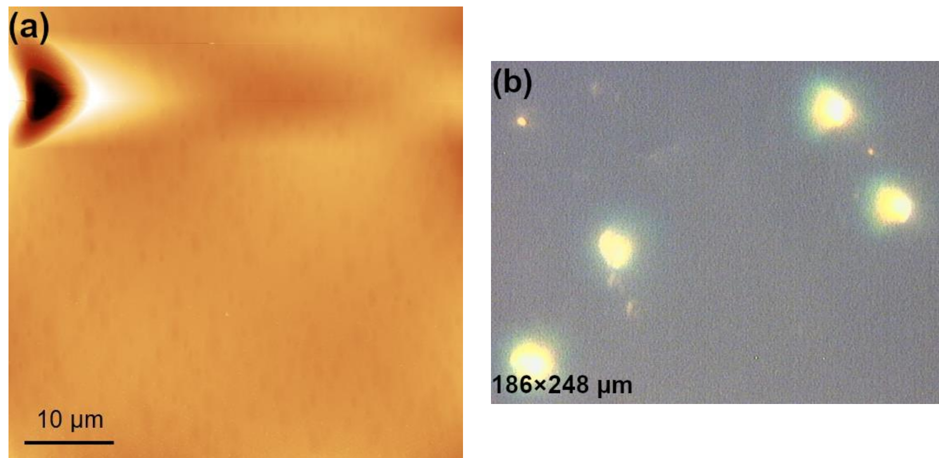

Figure 7.8. (a) 50×50 μm^2 AFM topography and (c) 186×248 μm^2 Nomarski microscope images of vicinal GaAs(111)A substrate after wet etching by HNO_3:H_2O (1:3) solution for 1 min at room temperature.

Therefore, the growth temperature of about 450 – 470 °C and the growth rate of 0.5 – 0.7 ML/s are optimal growth conditions to obtain smooth surface of InAlAs layer with high In content on vicinal GaAs(111) with the satisfactory level of threading dislocations. 470 °C was chosen as the growth temperature of $In_{0.6}Al_{0.4}As$ barrier layer to improve the crystal quality and optical properties of the layer. RMS of sample C is observed to be 0.43 nm, calculated from 1×1 μm^2 AFM scan, which is comparable to the 1.3 ML thickness of $In_{0.6}Al_{0.4}As$ along [111] direction. RMS calculated from 5×5 and 10×10 μm^2 AFM scans, is about 1 nm (see Figure 7.9).

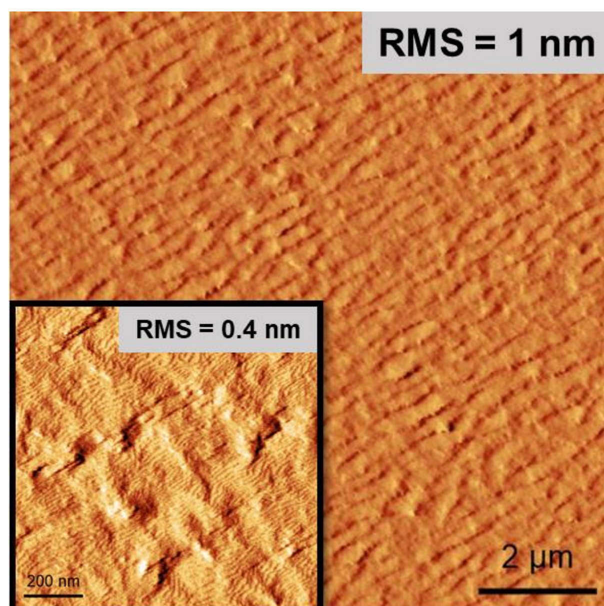

Figure 7.9. 10×10 μm^2 AFM amplitude image of sample C (the inset shows 1×1 μm^2 AFM amplitude image of the sample).

7.2. μ-PL characterization of single InAs QDs

In order to perform μ-PL study of individual QDs, it is necessary to fabricate nanostructures with a density of $10^8 – 10^9$ cm^{-2}. From the previous work[170], In droplets, directly deposited on vicinal GaAs(111)A substrate at a temperature about 400 °C, have the desired density.

Figure 7.10 shows the morphology of samples D and E with uncapped self-assembled DE InAs QDs fabricated on 200 nm $In_{0.6}Al_{0.4}As$ MMBL by deposition of 1 and 2 ML of indium at 370°C, respectively, followed by an annealing in As_4 atmosphere at same temperature. QD densities for both samples are almost the same: $2.52×10^8$ cm^{-2} for sample D and $2.50×10^8$ cm^{-2} for sample E, calculated from 10×10 μm^2 AFM scan of each sample. It is worth mentioning that the shape of QDs is different for these samples. Most of QDs of sample D have triangular pyramidal shape (see the inset of Figure 7.10a) with a height of 9.6±2.3 nm and width of 196±41 nm, measured for 50 dots. On the other hand, the majority of dots of sample E has hexagonal-like pyramidal shape (see the inset of Figure 7.10b) with a height of 15.9±3.3 nm and width of 266±52 nm, measured also for 50 dots. According to[115], GaAs DE-QD formation process is strongly affected by the diffusion of Ga adatoms out of the droplet, which leads to GaAs material accumulation within a Ga diffusion length from the droplet edge. Using identical crystallization conditions (substrate temperature and As flux), the Ga adatom diffusion length is the same. Considering a model of triangular and hexagonal DE GaAs QDs formation on GaAs(111)A[39,40], with the increasing initial droplet size, shape transition from triangular to hexagonal should occur. Furthermore, hexagonal QDs of sample E are elongated in the $\left[1\bar{1}0\right]$ direction along steps due to presence of sizeable ES barrier[136,140], which hinders an adatom diffusivity in the $\left[\bar{1}\bar{1}2\right]$ direction perpendicular to steps.

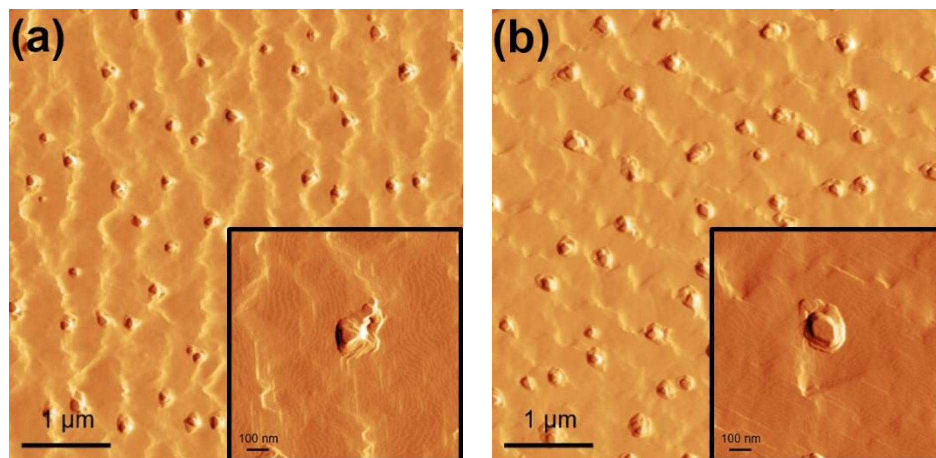

Figure 7.10. (a) 5×5 μm^2 AFM amplitude image of sample D (the inset shows 1×1 μm^2 AFM amplitude image of individual QD with triangular pyramidal shape with the height of 14 nm); (b) 5×5 μm^2 AFM amplitude image of sample E (the inset shows 1×1 μm^2 AFM amplitude image of individual QD with asymmetrical hexagonal-like pyramidal shape with a height of 16.6 nm).

Samples F and G with capped InAs QDs were characterized by µ-PL. Figure 7.11 shows the ensemble PL spectra of samples F and G at 800 – 1500 nm range. The peak at 838 nm is associated with GaAs substrate, the peaks at 900 – 1110 nm range corresponds to $In_{0.6}Al_{0.4}As$ barrier layer and the emissions from InAs QDs are placed in 1100 – 1350 – nm broad band.

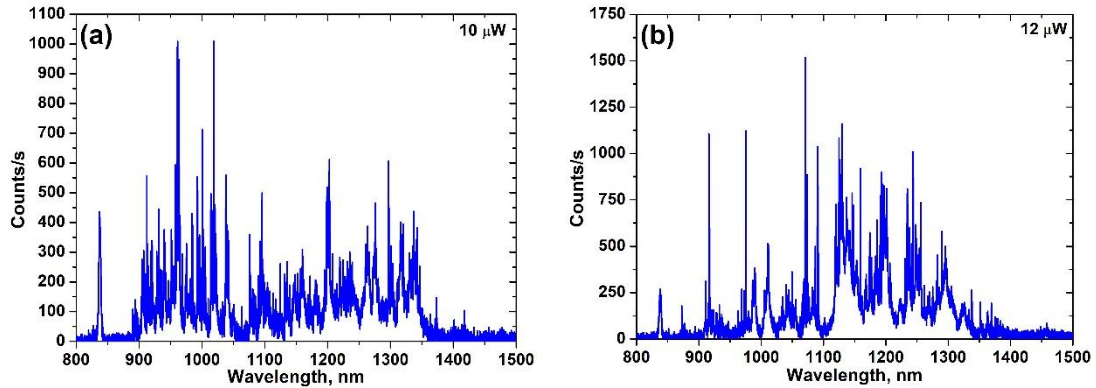

Figure 7.11. The ensemble luminescence spectra (a) of sample F with a cw excitation of 10 µW and (b) sample G with a cw excitation of 12 µW.

A typical photoluminescence spectrum for individual QD of sample F is presented in Figure 7.12. The observed peak with a linewidth (FWHM) of about 250 µeV (0.33 nm), fitted by Lorentzian function, is attributed to neutral X line, due to linear dependence of PL intensity on excitation power. The observed FWHM of QDs for both samples is in the range of 130 – 350 µeV. The resolution of the PL set-up is 0.07 nm, which corresponds to about 50 µeV at 1310 nm.

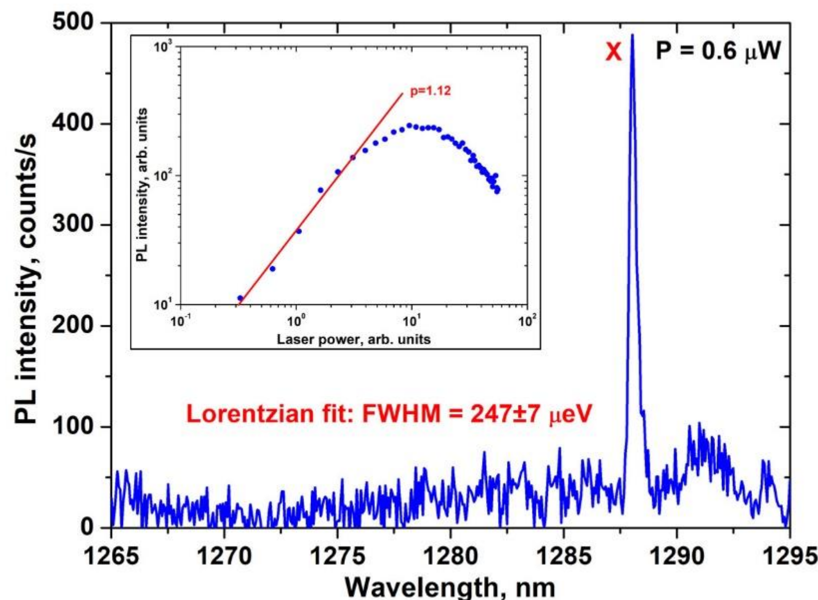

Figure 7.12. The luminescence spectrum of an individual InAs dot for sample F with a cw excitation of 0.6 µW. The inset shows power dependence of PL intensity of observed neutral X line.

FSS measurements

Polarization-dependent PL measurements were performed (see Figure 7.13). FSS measurements below the limit of the spectrometer were achieved by the polarization sensitive detection method[45,125], which make it possible to measure FSS with a limit of about 1 μeV using this set-up[169]. Figure 7.13a shows a polarization angle dependence of emission line energy extracted from center-of-mass PL intensity for individual QD of sample G, emitted at 1310 nm. The measurements reveal a FSS of 55±4 μeV for this QD.

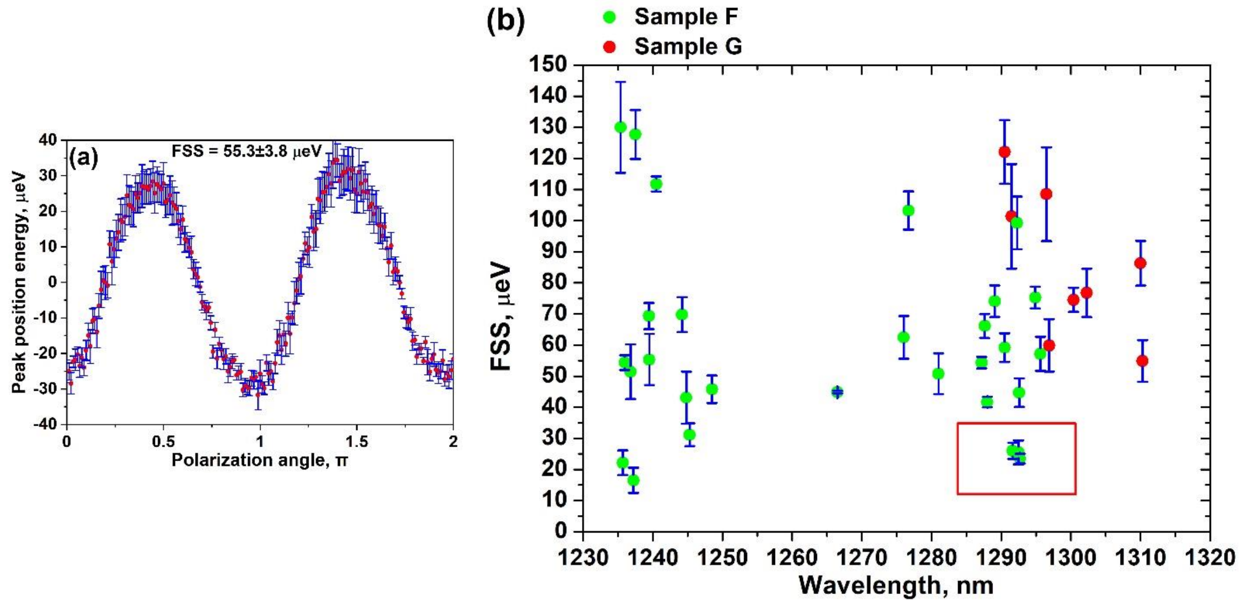

Figure 7.13. (a) Polarization dependence of QD emission line (1310 nm) of sample G with a finite FSS = 55.3±3.8 μeV. (b) Statistical distribution of FSS of samples F (green points) and G (red points).

The most important feature is the existence of telecom QDs with FSS value below 20 μeV (highlighted by red rectangular in Figure 7.13b). FSS of sample F is within the range of 15 – 100 μeV, with most of values below 60 μeV. As expected, bigger QDs of sample G emit at longer wavelengths. Poor statistics for the sample are associated with the fact that most of observed peaks are related to charged excitons, which doesn't show FSS and just few neutral lines were observed. FSS of sample G is within the range of 55 – 120 μeV, which is higher than the majority of sample F.

To generalize our observations, we measured corresponding polarization angles of the high energy QD excitonic peak for both samples (see Figure 7.14). The high energy component of the bright exciton is aligned along a particular direction (about 40 – 50° of HWP in our measurements), which is related to the QD anisotropy. In the work[30] similar behavior was attributed to QD shape anisotropy. Unfortunately, in these measurements we do not know the exact direction of the miscut (correspondence with HWP angle), therefore it is impossible to match the polarization of high energy excitonic peak with the direction of miscut or elongation of QD (actually these directions are orthogonal). In sample D, only symmetrical shape QDs were observed. However, sample F with the same but capped QDs, also shows the presence of particular direction of the high energy excitonic peak. And for QDs grown on exact (111) surface, the isotropic in-plane distribution of photoluminescence exciton polarization was observed[200]. Thus, we conclude that such behavior may be associated with the presence of miscut along $\left[\bar{1}\bar{1}2\right]$ direction perpendicular to steps of vicinal surface, which break the perfect C_{3v} symmetry of QDs grown on the (111) surface.

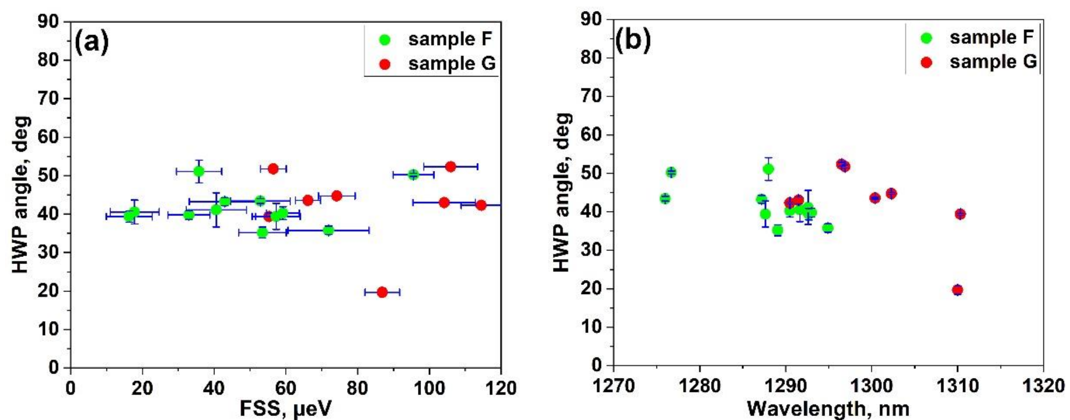

Figure 7.14. Polarization angles of the high-energy component of QD exciton peak vs. (a) FSS, (b) emission wavelength.

7.3. Increasing the brightness

Now we are facing several problems, which should be solved to achieve highly efficient entangled photon emission. There are the wide linewidth of X and XX lines, broad range of FSS, and low extraction efficiency. The first two are very complex issues, whereas the brightness of the dots can be easily increased by embedding QDs in cavity placed between DBR structures. Such approach is well established for emission enhancement of QDs grown on (001) substrates.

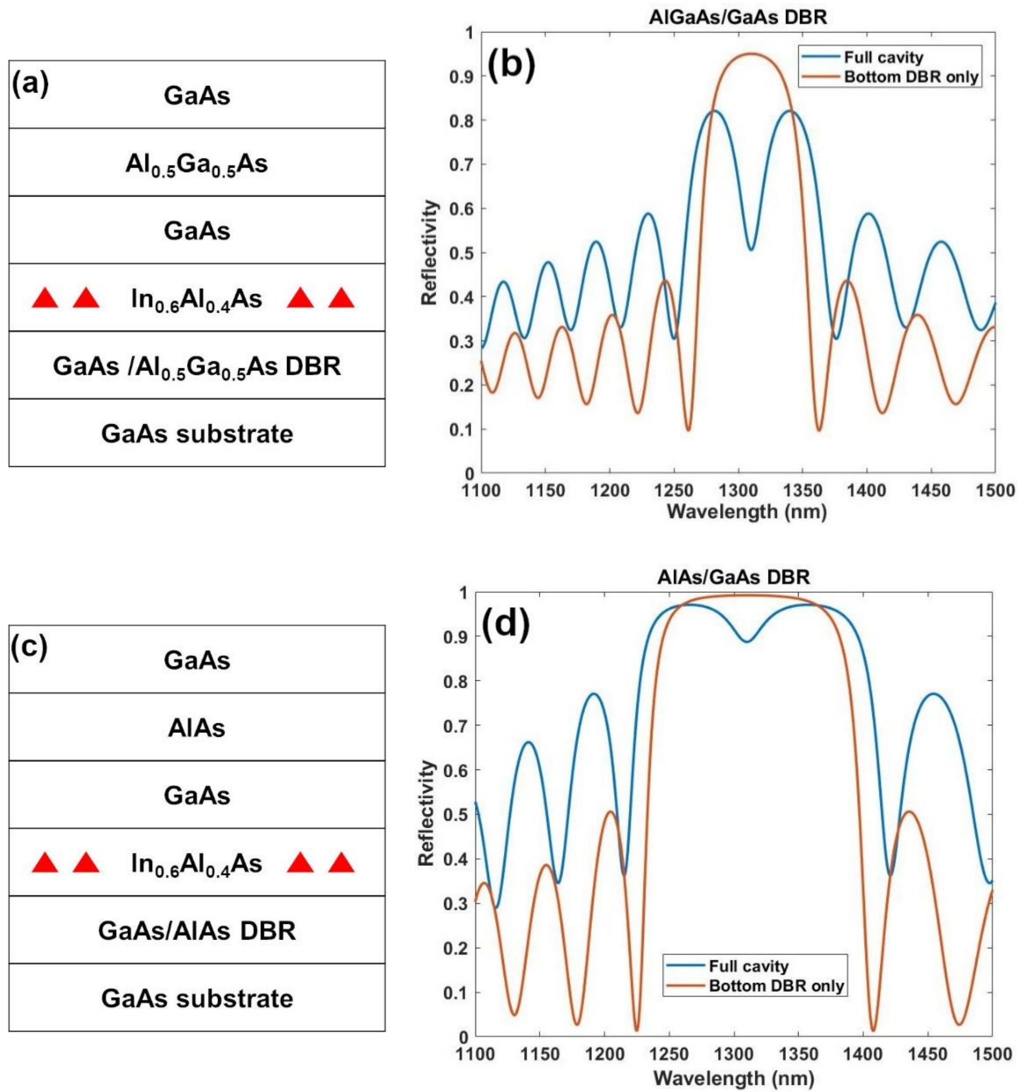

Figure 7.15. The $In_{0.6}Al_{0.4}As$ cavity design with DBRs consisting of several periods of (a) $Al_{0.5}Ga_{0.5}As$/GaAs and (b) AlAs/GaAs layers. Red triangles indicate InAs QDs, which should be placed in the middle of cavity layer. (b) and (d) Calculated room temperature reflectivity of full cavity and only bottom DBR of structures (a) and (c), respectively.

Since we achieved so far the emission from InAs QDs on vicinal GaAs(111)A in the O-band telecom range (1260 to 1360 nm), thus we designed the cavity for the wavelength of 1310 nm.

All the next work was done in the collaboration with Andrea Barbiero, PhD student in Cambridge Research Laboratory of Toshiba Research Limited[201]. He made the calculation of the cavity design and carried out all PL measurements of the samples with InAs QDs embedded in the cavity grown in L-NESS[120].

Two cavity structures consisting AlGaAs/GaAs DBR layers with Al content of 50 and 100% have been designed (see Figure 7.15). The asymmetric cavity design allows to avoid photon leakage to the substrate and realize photon emission in the opposite direction. An ideal case is to use AlAs/GaAs DBRs due to larger refractive index difference between the layers, which leads to

wider photonic bandgap of DBR. On the other hand, the growth of AlGaAs layers with high Al content on GaAs(111)A is a complicated task due to reduced surface migration lengths of Al adatoms compare to mobile Ga adatoms. Readily adsorbed Al adatoms are able to rotate about the available single chemical bond on (111) surface, promoting the formation of twin defects. Under high adatom migration (as in the case of Ga adatoms), however, adatoms can easily migrate to existing terrace edges where more than one dangling bond is present, suppressing twin defect formation effectively[157]. Thus $Al_{0.5}Ga_{0.5}As$/GaAs DBR is good alternative for the cavity design.

Firstly, it was necessary to optimize the final surface of bottom DBR layer for subsequent InAlAs barrier growth and DE InAs QD fabrication. We have tested the growth of bottom DBR structure on two vicinal GaAs(111)A substrates with 1° and 2° miscut toward $(\bar{1}\bar{1}2)$. For both substrates optimal growth conditions for DBR structure are high growth rate and high deposition temperature. For $Al_{0.5}Ga_{0.5}As$/GaAs DBR we used 0.5 ML/s for GaAs layer growth, 1 ML/s for AlGaAs, and the deposition temperature of 590 – 610 °C for both layers. It is necessary to emphasize again that the optimal growth rate for AlGaAs layers on singular GaAs(111)A is less than 0.1 ML/s[136], which makes the growth of DBR structure on singular substrate much longer.

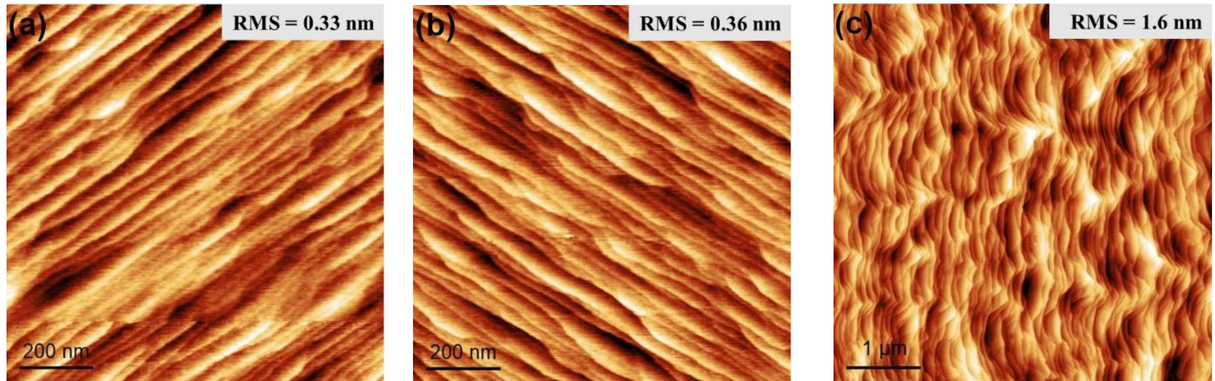

Figure 7.16. 1×1 µm^{2}AFM topography images of $Al_{0.5}Ga_{0.5}As$/GaAs DBR structure grown on vicinal GaAs(111) substrate with (a) 1° and (b) 2° miscut toward $(\bar{1}\bar{1}2)$. (c) 5×5 µm^2 AFM topography image of AlAs/GaAs DBR structure grown on vicinal GaAs(111) substrate with 2° miscut toward $(\bar{1}\bar{1}2)$.

Figure 7.16a, b shows AFM images of 20 periods of $Al_{0.5}Ga_{0.5}As$/GaAs grown on both 1° and 2° miscut GaAs(111)A, respectively. The morphology with the bunching of 5-6 steps is observed. RMS roughness for both substrates is on the level of 1 ML GaAs(111)A thickness, which is suitable for DE QD fabrication.

Fabrication of a very flat AlAs/GaAs DBR structure was not successful. The minimal RMS roughness of about 1.5 nm was achieved for the deposition temperature of 610 °C and 1 ML/s growth rate for both layers (see Figure 7.16c).

Therefore, we have chosen the cavity design with $Al_{0.5}Ga_{0.5}As$/GaAs DBR and then optimized the thicknesses of GaAs and AlGaAs layers to shift the center of DBR photonic bandgap close to 1310 nm wavelength. Figure 7.17 shows room temperature reflectivity measurements of such DBR structure. The maximum reflectivity at ~ 1330 nm is below 70% due to the low number of AlGaAs/GaAs periods, since for that sample we were interested only in the position of the maximum.

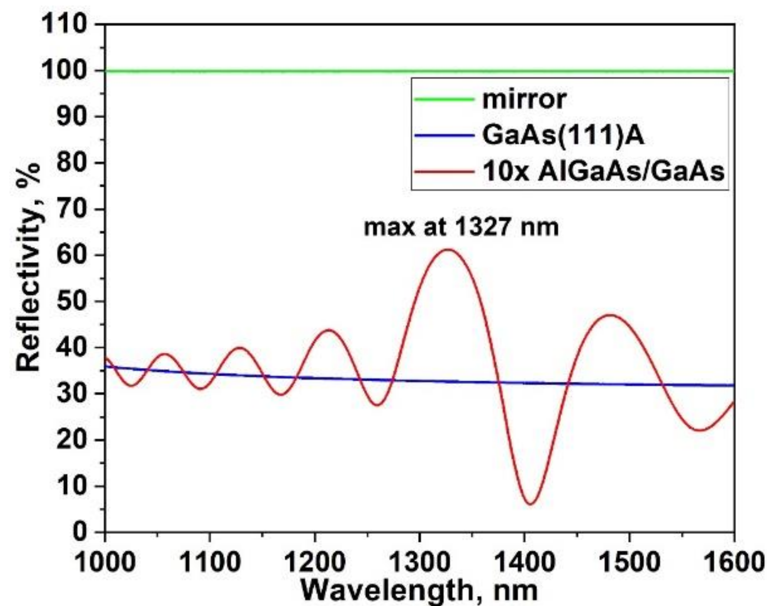

Figure 7.17. Room temperature reflectivity measurement of 10 periods of $Al_{0.5}Ga_{0.5}As$/GaAs layers grown on vicinal GaAs(111)A.

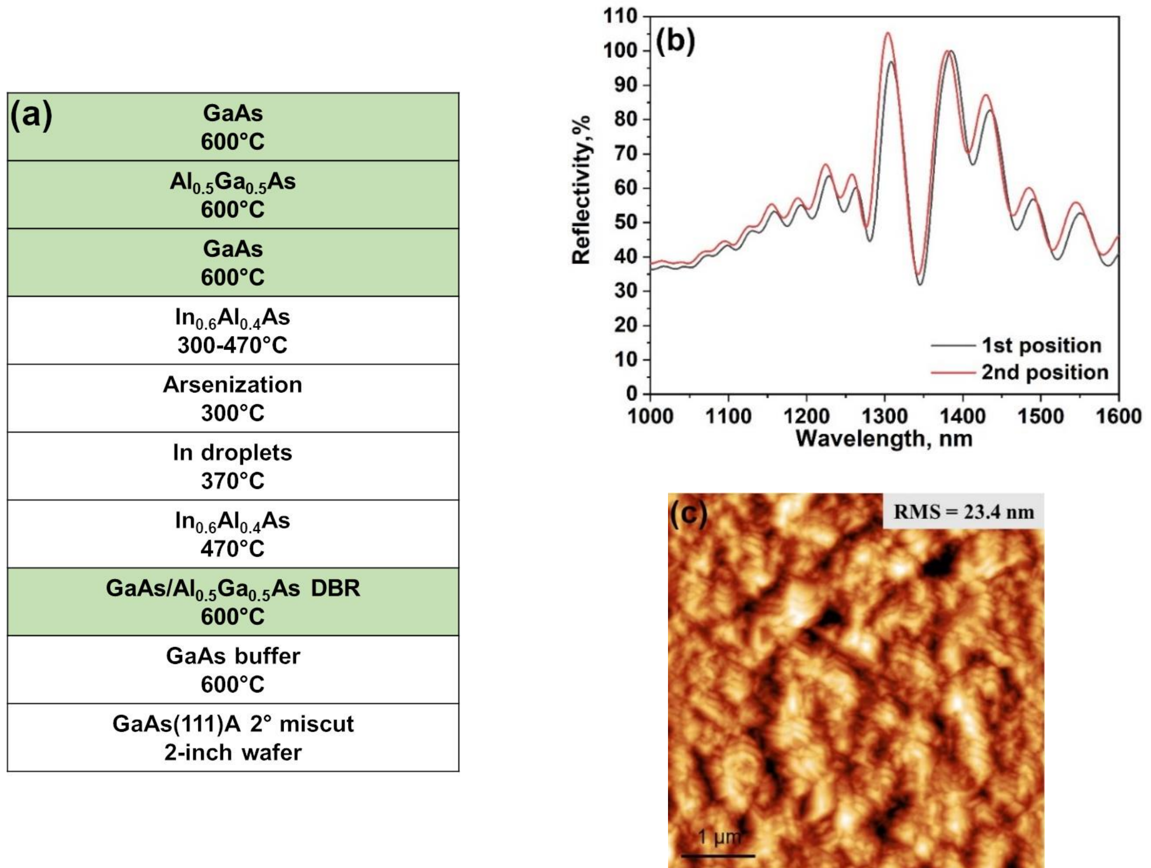

Figure 7.18. (a) The structure and the growth parameters of sample with DE InAs QDs embedded in the cavity. (b) Room temperature reflectivity measurements of that sample in two different positions of 2-inch wafer (position 1 – center of the wafer, position 2 is close to the edge of the wafer). (c) 5×5 μm^2AFM topography image of the final morphology of the sample.

For sample H (InAs QDs embedded in the cavity) the growth conditions for InAlAs barrier layer and DE InAs QD fabrication were the same as for sample F (see Table 7.1). The DE deposition on DBR structure slightly increased the density of InAs islands (from 2.5×10^8 cm^{-2} without bottom DBR to 4×10^8 cm^{-2} with DBR). The structure of the sample H is presented in Figure 7.18a. Reflectivity measurements show similar behavior of cavity structure with the gap of about 1350 nm in two different spots of 2-inch wafer, center of the wafer and the edge (see Figure 7.18b). AFM characterization shows a large RMS roughness of 23.4 nm in 5×5 μm^2 scan area of the final surface morphology and the presence of twin defects. The appearance of twins was observed during the growth by RHEED technique. It is established that these defects appear during capping InAs QDs by InAlAs barrier layer and it becomes more significant with increasing the thickness of top layer. We associate the appearance of twins with the strain relaxation close to InAs QDs. Then, with increasing the thickness of the capping layer, the defects became larger in size and cover all surface, which leads to rough surface morphology of the final GaAs layer. Figure 7.19 shows the morphology after the capping QDs only by 100 nm InAlAs layer. There is the presence

of big twin structures, however they cover only part of the surface. Similar behavior was observed during the growth of InAlAs MMBL layer, when we inserted thin intermediate InAs layer (see Figure 7.2), but the density of 3D features was not enough to confirm twin defect appearance by RHEED.

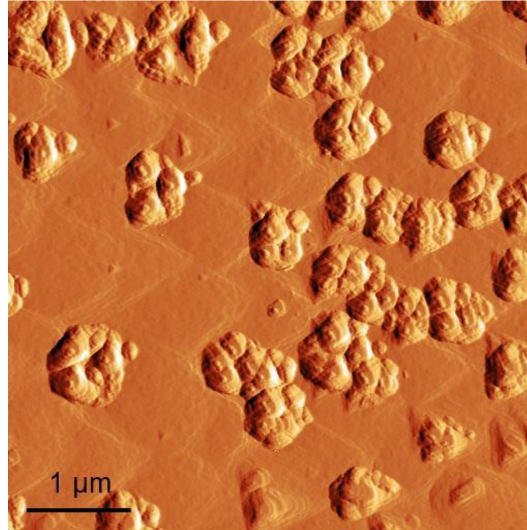

Figure 7.19. 5×5 μm^{2}AFM amplitude image sample with InAs QD grown on DBR structure and capped by 100 nm InAlAs layer.

PL characterization

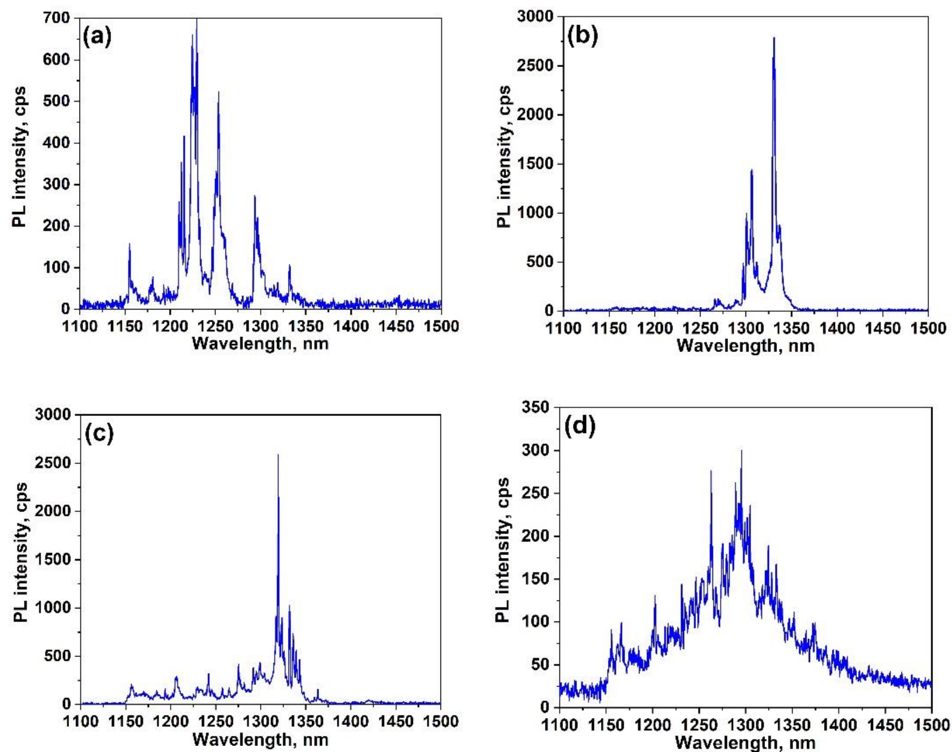

Figure 7.20. (a), (b), and (c) The luminescence spectrum of sample H taken on area A, B, and C, respectively. (d) The luminescence spectrum of sample F (InAs QDs without the cavity). All measurements were performed under cw laser excitation of ~ 200 μW.

μ-PL characterization was carried out using the setup, which is very similar to the one, described in Chapter 4.3. There are several differences. The set-up in Cambridge Research Laboratory[201] is fiber-coupled, thus it explains why the PL intensities measured in KTH[124] are larger for the sample F (compare Figure 7.11 and Figure 7.20d). A long pass-filter was used, which cuts all emissions below 1100 nm. And the main difference is related to polarization-dependent measurements. To measure FSS the quarter-wave plate (QWP)[165] was used instead of HWP.

Three areas of the waver were analyzed: the center, the middle and the edge of the 2-inch wafer, named as A, B, and C areas, respectively. All three areas show a smaller number of brighter PL peaks compare to sample F (although the density of InAs islands is slightly higher). There are two factors that explain the lower density of PL lines in this sample: first of all the presence of the cavity, which increases the light extraction in narrow wavelength range around 1310 nm, while PL spectra of dots without the cavity show a broadband of PL peaks from InAs QDs (see Figure 7.11). Additionally, cubic zirconia SIL[60,202,203] was placed on the top the sample, in order to improve the laser focusing (decrease the laser spot size) and to increase collection efficiency.

Nevertheless, areas B and C show brighter peaks than area A. The brightness is up to ten times higher compare to no cavity dots (see Figure 7.20). And higher number of "sharp" lines was observed in area C. Thus, all the next PL measurements were performed in that area of wafer. We associate this difference with the temperature gradient due to the thermocouple situated between substrate holder and the wafer close to the center of wafer. It leads to slightly lower growth temperature in the center of wafer compare to middle and edge areas.

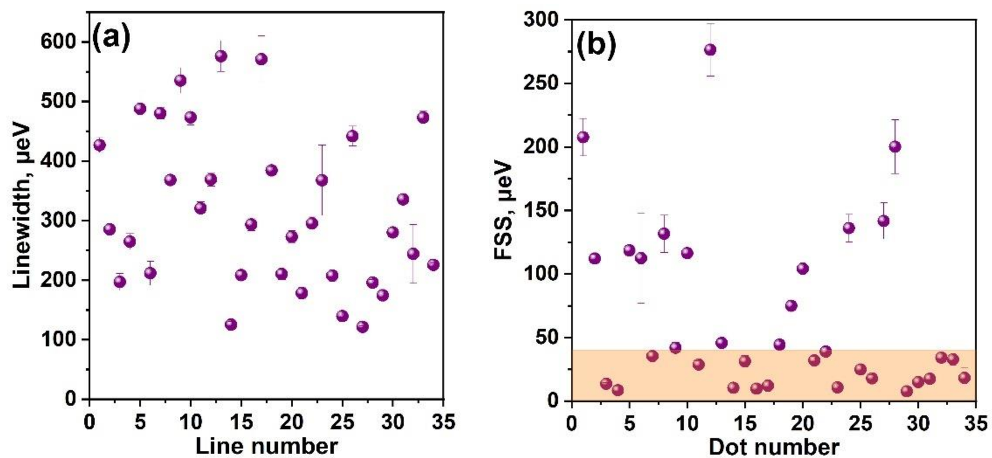

Figure 7.21. (a) PL linewidths of InAs QDs embedded in cavity and (b) their FSS.

Figure 7.21a presents statistics of linewidth values of PL lines taken in C area of the sample H. It is observed that linewidth of dots embedded in cavity is on the same level as for dots grown without DBR layers. The average value is about 350 μeV. We attribute such behavior of rather high linewidth for both samples (with and without cavity) to the presence of point defects, due to low

deposition temperature for Al during InAlAs layer growth, the presence of threading dislocations in InAlAs MMBL, and twin defect after the capping InAs QDs. The surface charge fluctuation is not relevant, since there is no difference in linewidth for sample F and H, although the thickness of capping layer for sample H is more than two times bigger (150 nm for sample F and ~ 400 nm for sample H).

Such large linewidths lead to a limit in the FSS value, which can be resolved. FSS is extracted by fitting the position of the center of mass of the peaks. Thus, if the peak is broad, it becomes more complicated to extract the small position variations, which leads to noisy data and less accurate fitting. For the average linewidth of 350 μeV, we estimated a resolution limit around 35 μeV (10% of the linewidth).

Two groups of dots with high FSS (> 100 μeV) and with small FSS (below 50 μeV) were observed (see Figure 7.21b). Low FSS dots show random polarization angle position, and the polarization direction of high FSS dots is aligned along specific orientation about 60 – 70° of QWP angle (see Figure 7.22). Since the specific polarization direction was observed also for dots without cavity structure (see Figure 7.14) and the FSS dependence on the emission wavelength suggest that two group of dots is not related to their size (see Figure 7.22b), thus we attribute random polarization angle position of QDs with lower FSS to the problem in polarization direction determination due to the resolution level of the measurements, induced by broader linewidth of QDs in cavity structures.

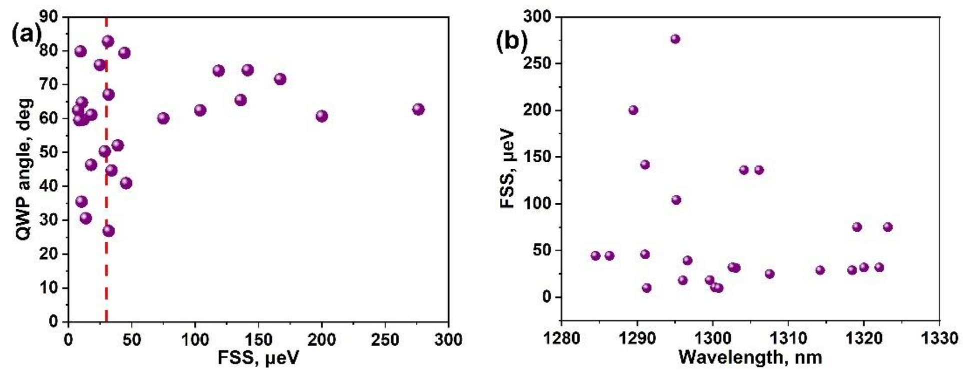

Figure 7.22. (a) Polarization angles of the high-energy component of QD exciton peak vs. FSS, (b) FSS dependence on the emission wavelength.

Finally, polarization dependence measurements were carried out with the alignment to the $\left[\bar{1}\bar{1}2\right]$ direction of miscut. It corresponds to the rotation of QWP through an angle of ~ 52° (see Figure 7.23). Unfortunately, the less efficient spectrometer was used for that measurement, and due to limited time only few dots were resolved. However, it is observed that most of polarization directions of QD exciton high energy components are aligned to the miscut direction.

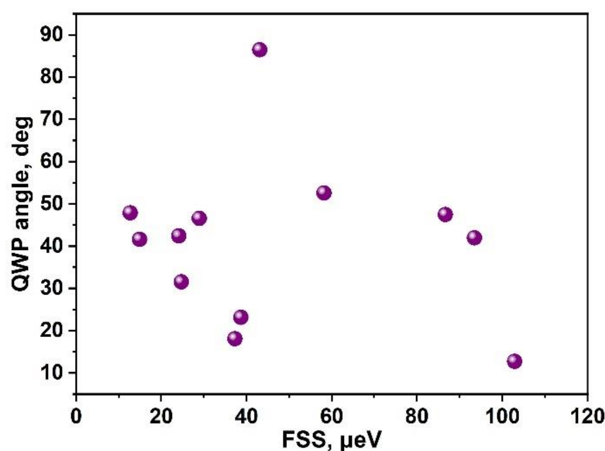

Figure 7.23. Polarization angles of the high-energy component of QD exciton peak vs. FSS.

Atomistic Pseudopotential Theory calculation

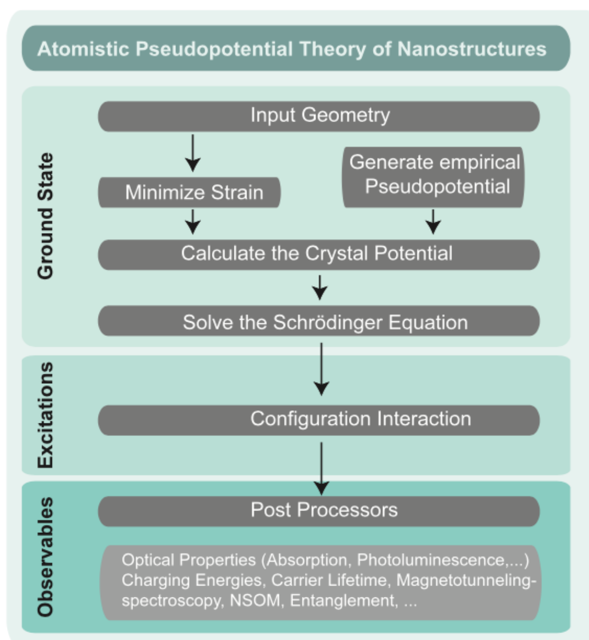

Figure 7.24. Flowchart of the methodology underlying the atomistic calculation of various observables for semiconductor nanostructures. The flowchart is divided into three logical sections: ground state, excitations (many-body part), and observables[204].

To understand if the stepped surface influence on QD exciton polarization and FSS, Geoffrey Pirard, PhD student of Hamburg University made a calculation using Atomistic Pseudopotential Theory[204], to determine the polarization of X lines in presence of substrate miscut misorientation.

The basis of the methodology is given in Figure 7.24 in the form of a flowchart summarizing the different components of the approach. The methodology is divided into three logical segments, labeled *Ground State*, *Excitations* and *Observables*, feeding into each other. The calculation of the ground state requires the input of the geometry and relaxation of the atomic positions to minimize strain. The generation of empirical pseudopotentials is the prerequisite for the construction of the total crystal potential used subsequently in the Schrödinger equation. The ensuing eigenfunctions

are fed into a configuration interaction treatment to obtain excitations. Finally, from the many-body wavefunctions, observables can be obtained through the use of post-processor tools[204].

The simulation was simplified by using $GaAs/Al_{0.15}Ga_{0.85}As(111)A$ QD. The QD shape was established as a truncated pyramid with a hexagonal base. The miscut direction was aligned toward $\left[\bar{1}\bar{1}2\right]$ direction. The miscut angle is varied from 0 to 3°. The result of the simulation is presented on Figure 7.25. The simulation confirmed that the presence of miscut breaks the C_{3v} symmetry and the polarization is aligned to the miscut direction.

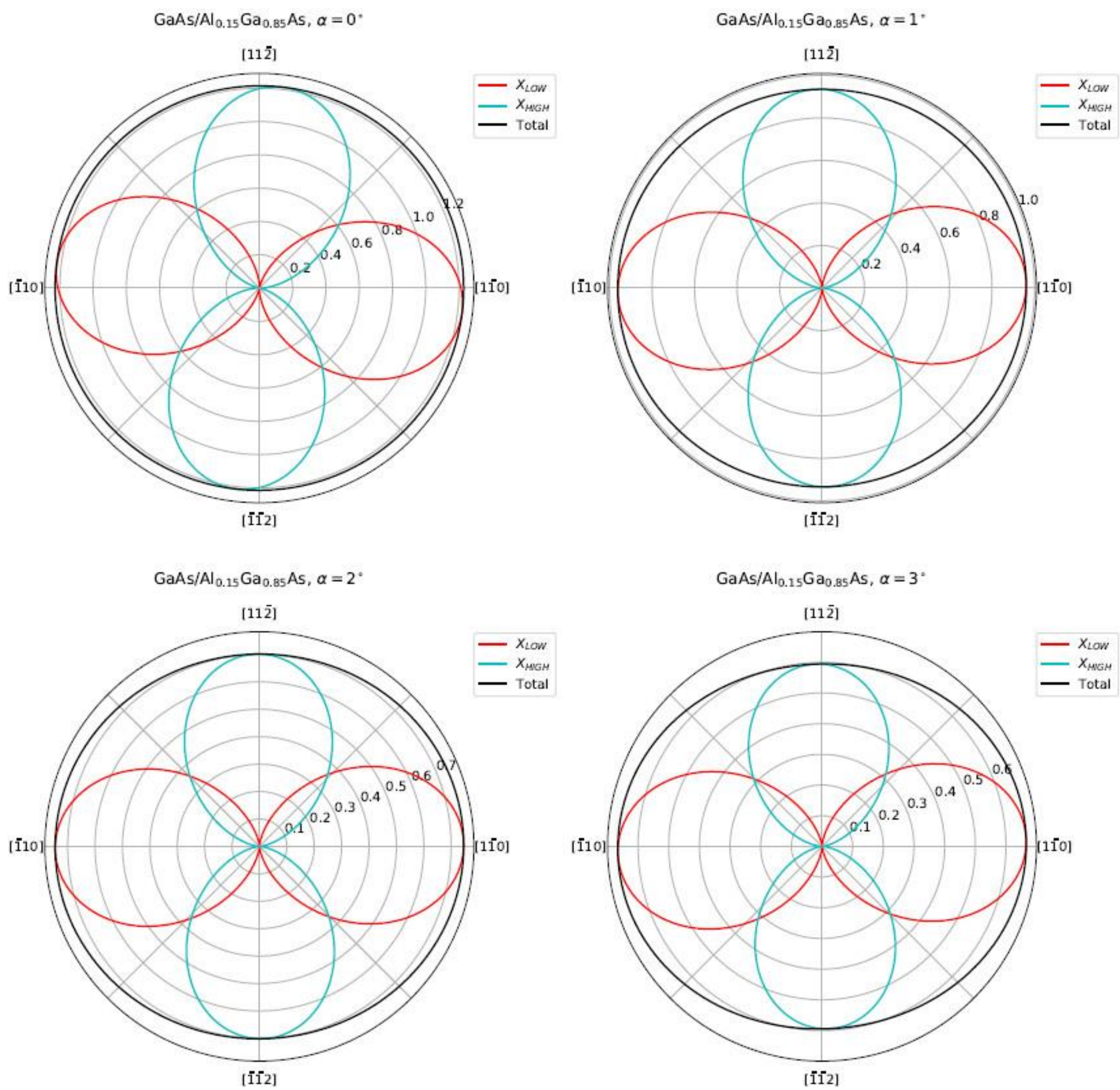

Figure 7.25. Atomistic Theory simulation of exciton polarization of GaAs/AlGaAs(111)A QD in the presence of miscut toward $\left[\bar{1}\bar{1}2\right]$ direction. The miscut angle is varied from 0 to 3°.

Another important feature of the miscut is an influence on FSS value. This effect was also calculated by Atomistic Theory method and it is presented in Figure 7.26. As expected, with increasing the miscut angle FSS increases. With increasing the miscut angle, the width of one step terrace decrease, according to ratio between angles. It means that the same planar size of QD will intersect bigger number of steps and the height difference from one side to another also increases with increasing the angle, which leads to bigger asymmetry of QD shape. Thus, such results suggest the possibility to decrease FSS of QDs grown on vicinal substrates. It is necessary to use the smallest miscut angle as possible. From our experiments, it was concluded that the DBR growth on GaAs(111)A substrate with 1° miscut is similar to 2° miscut substrates, therefore the next improvement of QD fabrication on (111) surfaces is related to use of substrates with 1° miscut, where the growth still governed by step-flow growth mode thanks to the presence of preferential nucleation sites at the step edges.

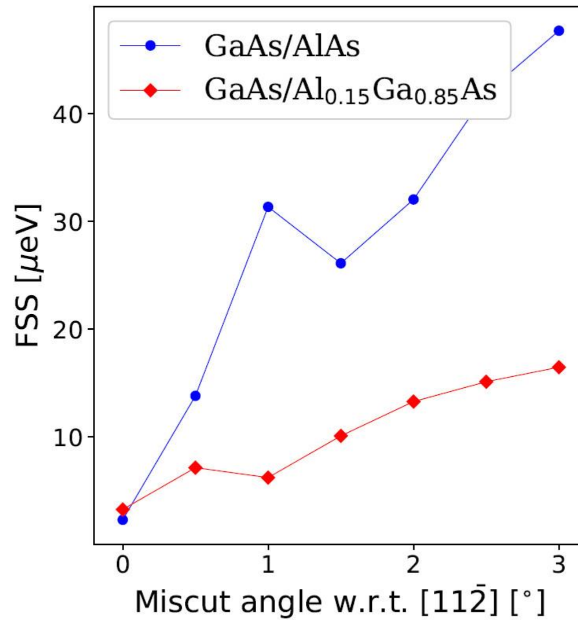

Figure 7.26. FSS dependence of GaAs/AlGaAs(111)A QD on miscut angle.

Conclusions and Outlook

In the present thesis we fabricated InAs QDs embedded in strain relaxed InAlAs layer on GaAs(111)A emitting in the telecom wavelength window at 1.3 μm, with the FSS value down to 16±6 μeV, thus demonstrating the possibility to use vicinal (111) surfaces and Droplet Epitaxy technique for QD engineering.

Several development steps were achieved:

1) A very flat and smooth MMBL surface for the deposition of the droplets. MMBL is necessary to reduce the strain between QD and barrier layer and to shift an emission of InAs QDs to telecom range. InAlAs MMBL with RMS roughness of about 1 ML have been grown directly on GaAs surface. XRD measurements demonstrate almost fully relaxed behavior of that layer. EPD calculation shows the presence of threading dislocations with the density of about 1×10^{7} cm^{-2}.

2) The control with high precision of the DE QD density and shape. We performed fundamental studies on the nucleation of Ga and In droplets on singular and miscut substrates, highlighting the role of the ES barriers at the step edges controlling the adatom diffusion and the strain relaxation in already formed In islands in determining the density at low deposition temperatures. DE allow to obtain InAs nanoislands with the low density of about 1×10^{8} cm^{-2} to study PL characterization of individual QDs. Two types of island shape were observed, depending on the initial size of droplets. Small In droplets are crystallized in InAs islands with triangular pyramidal shape. On the other hand, the deposition of 2 ML In and subsequent arsenization lead to hexagonal-like pyramidal shape of InAs QDs elongated in $\left[1\bar{1}0\right]$ direction along steps due to presence of sizeable ES barrier, which hinders an adatom diffusivity in the $\left[\bar{1}\bar{1}2\right]$ direction perpendicular to steps.

3) The increase the QD brightness. Here a study of the fabrication of QDs embedded in the cavity between DBR layers was carried out. It was shown the possibility to grow AlGaAs/GaAs DBR layers on vicinal GaAs(111)A. The brightness of dots embedded on asymmetrical cavity with the presence of cubic zirconia SIL on the top of the surface is up to ten times higher compare to InAs QDs grown without the cavity.

These developments allowed us to obtain DE InAs QDs with FSS as low as 16±6 μeV at 1.3 μm telecom O-band. It demonstrates the feasibility of the use of DE QDs on vicinal GaAs(111)A for future fabrication of entangled photon emitters based on these dots.

Some drawbacks are still hindering the adoption of this technique for the routine use in telecom applications. For both type of DE InAs QDs (with and without the cavity) rather broad PL linewidth is observed (mean linewidth value is about 300 – 350 μeV). We attribute such behavior to the presence of point defects, due to low deposition temperature for Al during InAlAs layer growth, the presence of threading dislocations in InAlAs MMBL, as well as twin defect after the capping InAs QDs. Therefore, to decrease the linewidth we propose several approaches. Since InAlAs layers, grown at the temperature above 450 °C, tend to have step bunching with high number of steps, it is possible to change MMBL composition from InAlAs to InGaAs. Additionally, to have the similar bandgap value for the barrier layer it is necessary to decrease In content in that layer, which also should decrease an amount of threading dislocations due to less lattice mismatch with GaAs substrate. To minimize twin defect appearance, we plan to fabricate the smallest InAs QDs as possible to decrease the value of local strain around the island during the capping layer formation.

Moreover, it was shown that InAs QDs grown on vicinal GaAs(111)A have specific polarization $\left[\bar{1}\bar{1}2\right]$ direction of X line due to presence of steps of miscut substrate, which is in good agreement with the atomistic theory calculation. According that calculation, to decrease FSS it is necessary to use the smallest miscut angle. From our experiments, it was concluded that the growth on GaAs(111)A substrate with 1° miscut still governed by step-flow growth mode thanks to the presence of preferential nucleation sites at the step edges, so such substrates should be used in future for the fabrication of InAs QDs on vicinal (111) surfaces.

Bibliography

1. Gurioli, M., Wang, Z., Rastelli, A., Kuroda, T. & Sanguinetti, S. Droplet epitaxy of semiconductor nanostructures for quantum photonic devices. *Nat. Mater.* **18**, 799–810 (2019).
2. Gisin, N., Ribordy, G., Tittel, W. & Zbinden, H. Quantum cryptography. *Rev. Mod. Phys.* **74**, 145–195 (2002).
3. Huber, D., Reindl, M., Aberl, J., Rastelli, A. & Trotta, R. Semiconductor quantum dots as an ideal source of polarization-entangled photon pairs on-demand: a review. *J. Opt.* **20**, 073002 (2018).
4. Kimble, H. J. The quantum internet. *Nature* **453**, 1023–1030 (2008).
5. Bennett, C. H. & Brassard, G. Quantum cryptography: Public key distribution and coin tossing. in *Proceedings of IEEE International Conference on Computers, Systems & Signal Processing* 175–179 (1984).
6. Ekert, A. K. Quantum cryptography based on Bell's theorem. *Phys. Rev. Lett.* **67**, 661–663 (1991).
7. Pomaríco, E. *et al.* Waveguide-based OPO source of entangled photon pairs. *New J. Phys.* **11**, (2009).
8. Orieux, A., Versteegh, M. A. M., Jöns, K. D. & Ducci, S. Semiconductor devices for entangled photon pair generation: a review. *Reports Prog. Phys.* **80**, 076001 (2017).
9. Thompson, J. K., Simon, J., Loh, H. & Vuletić, V. A High-brightness source of narrowband, identical-photon pairs. *Science* **313**, 74–77 (2006).
10. Reimer, M. E. & Cher, C. The quest for a perfect single-photon source. *Nat. Photonics* **13**, 734–736 (2019).
11. Akopian, N., Wang, L., Rastelli, A., Schmidt, O. G. & Zwiller, V. Hybrid semiconductor-atomic interface: Slowing down single photons from a quantum dot. *Nat. Photonics* **5**, 230–233 (2011).
12. Trotta, R. *et al.* Wavelength-tunable sources of entangled photons interfaced with atomic vapours. *Nat. Commun.* **7**, 10375 (2016).
13. Basso Basset, F. *et al.* High-Yield Fabrication of Entangled Photon Emitters for Hybrid Quantum Networking Using High-Temperature Droplet Epitaxy. *Nano Lett.* **18**, 505–512 (2018).
14. Ward, M. B. *et al.* Coherent dynamics of a telecom-wavelength entangled photon source. *Nat. Commun.* **5**, 3316 (2014).
15. Portalupi, S. L., Jetter, M. & Michler, P. InAs quantum dots grown on metamorphic buffers as non-classical light sources at telecom C-band: a review. *Semicond. Sci. Technol.* **34**, 053001 (2019).
16. Kako, S. *et al.* A gallium nitride single-photon source operating at 200 K. *Nat. Mater.* **5**, 887–892 (2006).
17. Choi, K., Arita, M., Kako, S. & Arakawa, Y. Site-controlled growth of single GaN quantum dots in nanowires by MOCVD. *J. Cryst. Growth* **370**, 328–331 (2013).
18. Bayer, M. *et al.* Fine structure of neutral and charged excitons in self-assembled In(Ga)As/(Al)GaAs quantum dots. *Phys. Rev. B* **65**, 195315 (2002).

19. Akopian, N. *et al.* Entangled Photon Pairs from Semiconductor Quantum Dots. *Phys. Rev. Lett.* **96**, 130501 (2006).

20. Stevenson, R. M. *et al.* Evolution of Entanglement Between Distinguishable Light States. *Phys. Rev. Lett.* **101**, 170501 (2008).

21. Heyn, C. Critical coverage for strain-induced formation of InAs quantum dots. *Phys. Rev. B* **64**, 165306 (2001).

22. Gong, M. *et al.* Statistical properties of exciton fine structure splitting and polarization angles in quantum dot ensembles. *Phys. Rev. B* **89**, 205312 (2014).

23. Musiał, A. *et al.* Toward weak confinement regime in epitaxial nanostructures: Interdependence of spatial character of quantum confinement and wave function extension in large and elongated quantum dots. *Phys. Rev. B* **90**, 045430 (2014).

24. Urbaszek, B. *et al.* Nuclear spin physics in quantum dots: An optical investigation. *Rev. Mod. Phys.* **85**, 79–133 (2013).

25. Welander, E., Hildmann, J. & Burkard, G. Influence of hyperfine interaction on the entanglement of photons generated by biexciton recombination. *arXiv:1409.6521v2* (2014).

26. Stevenson, R. M. *et al.* Coherent entangled light generated by quantum dots in the presence of nuclear magnetic fields. *arXiv:1103.2969* (2011).

27. Heyn, C. *et al.* Highly uniform and strain-free GaAs quantum dots fabricated by filling of self-assembled nanoholes. *Appl. Phys. Lett.* **94**, 183113 (2009).

28. Huber, D. *et al.* Highly indistinguishable and strongly entangled photons from symmetric GaAs quantum dots. *Nat. Commun.* **8**, 15506 (2017).

29. White, A. G. *et al.* Measuring two-qubit gates. *J. Opt. Soc. Am. B* **24**, 172 (2007).

30. Huo, Y. H., Rastelli, A. & Schmidt, O. G. Ultra-small excitonic fine structure splitting in highly symmetric quantum dots on GaAs (001) substrate. *Appl. Phys. Lett.* **102**, 152105 (2013).

31. Singh, R. & Bester, G. Nanowire Quantum Dots as an Ideal Source of Entangled Photon Pairs. *Phys. Rev. Lett.* **103**, 063601 (2009).

32. Mano, T. *et al.* Self-Assembly of Symmetric GaAs Quantum Dots on (111)A Substrates: Suppression of Fine-Structure Splitting. *Appl. Phys. Express* **3**, 065203 (2010).

33. Kuroda, T. *et al.* Symmetric quantum dots as efficient sources of highly entangled photons: Violation of Bell's inequality without spectral and temporal filtering. *Phys. Rev. B* **88**, 041306 (2013).

34. Yamaguchi, H. *et al.* Atomic-scale imaging of strain relaxation via misfit dislocations in highly mismatched semiconductor heteroepitaxy: InAs/GaAs(111)A. *Phys. Rev. B* **55**, 1337–1340 (1997).

35. Wen, H., Wang, Z. M., Shultz, J. L., Liang, B. L. & Salamo, G. J. Growth and characterization of InAs epitaxial layer on GaAs(111)B. *Phys. Rev. B* **70**, 205307 (2004).

36. Yerino, C. D. *et al.* Strain-driven growth of GaAs(111) quantum dots with low fine structure splitting. *Appl. Phys. Lett.* **105**, 251901 (2014).

37. Schuck, C. F. *et al.* Self-assembly of (111)-oriented tensile-strained quantum dots by molecular beam epitaxy. *J. Vac. Sci. Technol. B* **36**, 031803 (2018).

38. Schuck, C. F. *et al.* Anomalous Stranski-Krastanov growth of (111)-oriented quantum dots with tunable wetting layer thickness. *Sci. Rep.* **9**, 18179 (2019).

39. Jo, M. *et al.* Self-limiting growth of hexagonal and triangular quantum dots on (111)A. *Cryst. Growth Des.* **12**, 1411–1415 (2012).

40. Bietti, S. *et al.* High–temperature droplet epitaxy of symmetric GaAs/AlGaAs quantum dots. *Sci. Rep.* **10**, 6532 (2020).

41. Stevenson, R. M. *et al.* Indistinguishable entangled photons generated by a light-emitting diode. *Phys. Rev. Lett.* **108**, 1–5 (2012).

42. Müller, T. *et al.* A quantum light-emitting diode for the standard telecom window around 1,550 nm. *Nat. Commun.* **9**, 862 (2018).

43. Xiang, Z.-H. *et al.* A tuneable telecom wavelength entangled light emitting diode deployed in an installed fibre network. *Commun. Phys.* **3**, 121 (2020).

44. Zeuner, K. D. *et al.* A stable wavelength-tunable triggered source of single photons and cascaded photon pairs at the telecom C-band. *Appl. Phys. Lett.* **112**, 173102 (2018).

45. Trotta, R. *et al.* Universal recovery of the energy-level degeneracy of bright excitons in InGaAs quantum dots without a structure symmetry. *Phys. Rev. Lett.* **109**, 1–5 (2012).

46. Wang, J., Gong, M., Guo, G. C. & He, L. Eliminating the fine structure splitting of excitons in self-assembled InAs/GaAs quantum dots via combined stresses. *Appl. Phys. Lett.* **101**, (2012).

47. Wang, J., Gong, M., Guo, G.-C. & He, L. Towards Scalable Entangled Photon Sources with Self-Assembled InAs/GaAs Quantum Dots. *Phys. Rev. Lett.* **115**, 067401 (2015).

48. Huber, D. *et al.* Strain-tunable GaAs quantum dot: A nearly dephasing-free source of entangled photon pairs on demand. *Phys. Rev. Lett.* **121**, 033902 (2018).

49. Brown, R. H. & Twiss, R. Q. Correlation between photons in two coherent beams of light. *Nature* **177**, 27–29 (1956).

50. Hong, C. K., Ou, Z. Y. & Mandel, L. Measurement of subpicosecond time intervals between two photons by interference. *Phys. Rev. Lett.* **59**, 2044–2046 (1987).

51. Gazzano, O. & Solomon, G. S. Toward optical quantum information processing with quantum dots coupled to microstructures. *J. Opt. Soc. Am. B* **33**, C160–C175 (2016).

52. Schweickert, L. *et al.* On-demand generation of background-free single photons from a solid-state source. *Appl. Phys. Lett.* **112**, 093106 (2018).

53. Purcell, E. M. Spontaneous emission probabilities at radio frequencies. *Phys. Rev.* **69**, 681 (1946).

54. Gerard, J.-M. & Gayral, B. Strong Purcell effect for InAs quantum boxes in three-dimensional solid-state microcavities. *J. Light. Technol.* **17**, 2089–2095 (1999).

55. Sapienza, L., Davanço, M., Badolato, A. & Srinivasan, K. Nanoscale optical positioning of single quantum dots for bright and pure single-photon emission. *Nat. Commun.* **6**, 7833 (2015).

56. Munsch, M. *et al.* Dielectric GaAs antenna ensuring an efficient broadband coupling between an InAs quantum dot and a Gaussian optical beam. *Phys. Rev. Lett.* **110**, 177402 (2013).

57. Dousse, A. *et al.* Ultrabright source of entangled photon pairs. *Nature* **466**, 217–220 (2010).

58. Gazzano, O. *et al.* Bright solid-state sources of indistinguishable single photons. *Nat. Commun.* **4**, 1425 (2013).

59. Gschrey, M. *et al.* Highly indistinguishable photons from deterministic quantum-dot microlenses utilizing three-dimensional in situ electron-beam lithography. *Nat. Commun.* **6**, 7662 (2015).

60. Zwiller, V. & Björk, G. Improved light extraction from emitters in high refractive index materials using solid immersion lenses. *J. Appl. Phys.* **92**, 660–665 (2002).

61. Gschrey, M. *et al.* In situ electron-beam lithography of deterministic single-quantum-dot mesa-structures using low-temperature cathodoluminescence spectroscopy. *Appl. Phys. Lett.* **102**, 251113 (2013).

62. Gazzano, O. *et al.* Evidence for confined Tamm plasmon modes under metallic microdisks and application to the control of spontaneous optical emission. *Phys. Rev. Lett.* **107**, 4–8 (2011).

63. Sortino, L. *et al.* Enhanced light-matter interaction in an atomically thin semiconductor coupled with dielectric nano-antennas. *Nat. Commun.* **10**, 5119 (2019).

64. Günther, K. G. Aufdampfschidhten aus halbleitenden III-V-Verbindungen. *Zeitschrift für Naturforsch. A* **13**, 1081–1089 (1958).

65. Freller, H. & Günther, K. G. Three-temperature method as an origin of molecular beam epitaxy. *Thin Solid Films* **88**, 291–307 (1982).

66. Davey, J. E. & Pankey, T. Epitaxial GaAs films deposited by vacuum evaporation. *J. Appl. Phys.* **39**, 1941–1948 (1968).

67. Arthur, J. R. Interaction of Ga and As_2 molecular beams with GaAs Surfaces. *J. Appl. Phys.* **39**, 4032–4034 (1968).

68. Arthur, J. R. & LePore, J. J. GaAs, GaP, and $GaAs_xP_{1-x}$ Epitaxial Films Grown by molecular beam deposition. *J. Vac. Sci. Technol.* **6**, 545–548 (1969).

69. Cho, A. Y. Epitaxy by periodic annealing. *Surf. Sci.* **17**, 494–503 (1969).

70. Cho, A. Y. Morphology of epitaxial growth of GaAs by a molecular beam method: The observation of surface structures. *J. Appl. Phys.* **41**, 2780–2786 (1970).

71. Cho, A. Y. GaAs Epitaxy by a molecular beam method: Observations of surface structure on the (001) face. *J. Appl. Phys.* **42**, 2074–2081 (1971).

72. Cho, A. Y. & Arthur, J. R. Molecular beam epitaxy. *Prog. Solid State Chem.* **10**, 157–191 (1975).

73. Dingle, R., Störmer, H. L., Gossard, A. C. & Wiegmann, W. Electron mobilities in modulation-doped semiconductor heterojunction superlattices. *Appl. Phys. Lett.* **33**, 665–667 (1978).

74. Störmer, H. L. Electron mobilities in modulation-doped GaAs-(AlGa)As heterostructures. *Surf. Sci.* **132**, 519–526 (1983).

75. Mimura, T., Hiyamizu, S., Fujii, T. & Nanbu, K. A New Field-effect transistor with selectively doped GaAs/n-$Al_xGa_{1-x}As$ heterojunctions. *Jpn. J. Appl. Phys.* **19**, L225–L227 (1980).

76. Tsui, D. C., Stormer, H. L. & Gossard, A. C. Two-dimensional magnetotransport in the extreme quantum limit. *Phys. Rev. Lett.* **48**, 1559–1562 (1982).

77. Panish, M. B. Molecular beam epitaxy of GaAs and InP with gas sources for As and P. *J. Electrochem. Soc.* **127**, 2729–2733 (1980).

78. Panish, M. B. & Temkin, H. GaInAsP/InP heterostructure lasers emitting at 1.5 μm and grown by gas source molecular beam epitaxy. *Appl. Phys. Lett.* **44**, 785–787 (1984).

79. Neave, J. H., Joyce, B. A., Dobson, P. J. & Norton, N. Dynamics of film growth of GaAs by MBE from RHEED observations. *Appl. Phys. A* **31**, 1–8 (1983).

80. Van Hove, J. M. Damped oscillations in reflection high energy electron diffraction during GaAs MBE. *J. Vac. Sci. Technol. B* **1**, 741 (1983).

81. Goldstein, L., Glas, F., Marzin, J. Y., Charasse, M. N. & Le Roux, G. Growth by molecular beam epitaxy and characterization of InAs/GaAs strained-layer superlattices. *Appl. Phys. Lett.* **47**, 1099–1101 (1985).

82. Ramachandran, T. R. Nature of Stranski–Krastanow growth of InAs on GaAs(001). *J. Vac. Sci. Technol. B* **16**, 1330 (1998).

83. Horikoshi, Y., Kawashima, M. & Yamaguchi, H. Low-temperature growth of GaAs and AlAs-GaAs quantum-well layers by modified molecular beam epitaxy. *Jpn. J. Appl. Phys.* **25**, L868–L870 (1986).

84. Koguchi, N., Takahashi, S. & Chikyow, T. New MBE growth method for InSb quantum well boxes. *J. Cryst. Growth* **111**, 688–692 (1991).

85. Venables, J. A. Atomic processes in crystal growth. *Surf. Sci.* **299–300**, 798–817 (1994).

86. Michely, T. & Krug, J. *Islands, Mounds and Atoms*. *Springer series in surface sciences*, (Springer Berlin Heidelberg, 2004).

87. Bauer, E. Phänomenologische theorie der kristallabscheidung an oberflächen. I. *Zeitschrift für Krist.* **110**, 372–394 (1958).

88. Ichimiya, A. & Cohen, P. I. *Reflection High-Energy Electron Diffraction*. (Cambridge University Press, 2004).

89. Neave, J. H., Dobson, P. J., Joyce, B. A. & Zhang, J. Reflection high-energy electron diffraction oscillations from vicinal surfaces—a new approach to surface diffusion measurements. *Appl. Phys. Lett.* **47**, 100–102 (1985).

90. SpringThorpe, A. J., Ingrey, S. J., Emmerstorfer, B., Mandeville, P. & Moore, W. T. Measurement of GaAs surface oxide desorption temperatures. *Appl. Phys. Lett.* **50**, 77–79 (1987).

91. Markov, V. A., Nikiforov, A. I. & Pchelyakov, O. P. In situ RHEED control of direct MBE growth of Ge quantum dots on Si (001). *J. Cryst. Growth* **175–176**, 736–740 (1997).

92. Tuktamyshev, A. R., Mashanov, V. I., Timofeev, V. A., Nikiforov, A. I. & Teys, S. A. Initial growth stages of Si–Ge–Sn ternary alloys grown on Si (100) by low-temperature molecular-beam epitaxy. *Semiconductors* **49**, 1582–1586 (2015).

93. Tuktamyshev, A. R. *et al.* Sn influence on MBE growth of GeSiSn/Si MQW. *J. Phys. Conf. Ser.* **816**, 012020 (2017).

94. Goldfarb, I. & Briggs, G. A. D. Comparative STM and RHEED studies of Ge/Si(001) and Si/Ge/Si(001) surfaces. *Surf. Sci.* **433–435**, 449–454 (1999).

95. Ohtake, A. Surface reconstructions on GaAs(001). *Surf. Sci. Rep.* **63**, 295–327 (2008).

96. Horikoshi, Y. Migration-Enhanced Epitaxy and its Application. in *Molecular Beam Epitaxy*, 41–56 (John Wiley & Sons Ltd, 2019).

97. Chikyow, T. & Koguchi, N. MBE Growth method for pyramid-shaped GaAs micro crystals on ZnSe(001) surface using Ga droplets. *Jpn. J. Appl. Phys.* **29**, L2093–L2095 (1990).

98. Koguchi, N. & Ishige, K. Growth of GaAs epitaxial microcrystals on an S-terminated GaAs substrate by successive irradiation of Ga and As molecular beams. *Jpn. J. Appl. Phys.* **32**, 2052–2058 (1993).

99. Sanguinetti, S., Bietti, S. & Koguchi, N. Droplet Epitaxy of Nanostructures. in *Molecular Beam Epitaxy* 293–314 (Elsevier, 2018).

100. Carrier, O. & Bonn, D. Contact Angles and the Surface Free Energy of Solids. in *Droplet Wetting and Evaporation* 15–23 (Elsevier, 2015).

101. Jo, M., Mano, T., Sakuma, Y. & Sakoda, K. Size-dependent contact angle of Ga droplets on GaAs. *J. Cryst. Growth* **378**, 5–7 (2013).

102. Venables, J. A., Spiller, G. D. T. & Hanbucken, M. Nucleation and growth of thin films. *Reports Prog. Phys.* **47**, 399–459 (1984).

103. Pimpinelli, A. & Einstein, T. L. Capture-zone scaling in island nucleation: Universal fluctuation behavior. *Phys. Rev. Lett.* **99**, 226102 (2007).

104. Pimpinelli, A., Tumbek, L. & Winkler, A. Scaling and exponent equalities in island nucleation: Novel results and application to organic films. *J. Phys. Chem. Lett.* **5**, 995–998 (2014).

105. Okabe, A., Boots, B., Sugihara, K., Chiu, S. N. & Kendall, D. G. *Spatial Tessellations*. (John Wiley & Sons, Inc., 2000).

106. Guhr, T., Müller–Groeling, A. & Weidenmüller, H. A. Random-matrix theories in quantum physics: common concepts. *Phys. Rep.* **299**, 189–425 (1998).

107. Sanguinetti, S. *et al.* Carrier thermal escape and retrapping in self-assembled quantum dots. *Phys. Rev. B* **60**, 8276–8283 (1999).

108. Zhang, H., Chen, Y., Zhou, G., Tang, C. & Wang, Z. Wetting layer evolution and its temperature dependence during self-assembly of InAs/GaAs quantum dots. *Nanoscale Res. Lett.* **7**, 600 (2012).

109. Kumar, R., Maidaniuk, Y., Saha, S. K., Mazur, Y. I. & Salamo, G. J. Evolution of InAs quantum dots and wetting layer on GaAs(001): Peculiar photoluminescence near onset of quantum dot formation. *J. Appl. Phys.* **127**, 065306 (2020).

110. Bietti, S., Somaschini, C. & Sanguinetti, S. Crystallization kinetics of Ga metallic nano-droplets under As flux. *Nanotechnology* **24**, 205603 (2013).

111. Somaschini, C., Bietti, S., Koguchi, N. & Sanguinetti, S. Fabrication of multiple concentric nanoring structures. *Nano Lett.* **9**, 3419–3424 (2009).

112. Zhou, Z. Y., Zheng, C. X., Tang, W. X., Tersoff, J. & Jesson, D. E. Origin of quantum ring formation during droplet epitaxy. *Phys. Rev. Lett.* **111**, 036102 (2013).

113. Bietti, S., Somaschini, C., Esposito, L., Fedorov, A. & Sanguinetti, S. Gallium surface diffusion on GaAs (001) surfaces measured by crystallization dynamics of Ga droplets. *J. Appl. Phys.* **116**, 114311 (2014).

114. Fuster, D. *et al.* InAs nanostructures grown by droplet epitaxy directly on InP(001) substrates. *J. Cryst. Growth* **434**, 81–87 (2016).

115. Bietti, S. *et al.* Precise shape engineering of epitaxial quantum dots by growth kinetics. *Phys. Rev. B* **92**, 075425 (2015).

116. Heyn, C., Bartsch, T., Sanguinetti, S., Jesson, D. & Hansen, W. Dynamics of mass transport during nanohole drilling by local droplet etching. *Nanoscale Res. Lett.* **10**, 67 (2015).

117. Wang, Z. M., Liang, B. L., Sablon, K. A. & Salamo, G. J. Nanoholes fabricated by self-assembled gallium nanodrill on GaAs(100). *Appl. Phys. Lett.* **90**, 113120 (2007).

118. Somaschini, C., Bietti, S., Scaccabarozzi, A., Grilli, E. & Sanguinetti, S. Self-assembly of quantum dot-disk nanostructures via growth kinetics control. *Cryst. Growth Des.* **12**, 1180–1184 (2012).

119. Li, X. *et al.* Origin of nanohole formation by etching based on droplet epitaxy. *Nanoscale* **6**, 2675 (2014).

120. L-NESS: Laboratory for Epitaxial Nanostructures on Silicon and Spintronics. http://lness.como.polimi.it/.

121. Magonov, S. N. & Whangbo, M. *Surface Analysis with STM and AFM*. (Wiley, 1995).

122. Gwyddion – Free SPM data analysis software. http://gwyddion.net/.

123. ImageJ. https://imagej.net.

124. Quantum Nano Photonics Group | KTH. https://www.qnp.aphys.kth.se/.

125. Kowalik, K. *et al.* Influence of an in-plane electric field on exciton fine structure in InAs-GaAs self-assembled quantum dots. *Appl. Phys. Lett.* **86**, 041907 (2005).

126. Stevenson, R. M. *et al.* Magnetic-field-induced reduction of the exciton polarization splitting in InAs quantum dots. *Phys. Rev. B* **73**, 033306 (2006).

127. Bennett, A. J. *et al.* Electric-field-induced coherent coupling of the exciton states in a single quantum dot. *Nat. Phys.* **6**, 947–950 (2010).

128. Liu, A. Y. *et al.* High performance continuous wave 1.3 μm quantum dot lasers on silicon. *Appl. Phys. Lett.* **104**, 041104 (2014).

129. Stiff-Roberts, A. D. Quantum-dot infrared photodetectors: a review. *J. Nanophotonics* **3**, 031607 (2009).

130. Beattie, N. S. *et al.* Quantum Engineering of InAs/GaAs Quantum Dot Based Intermediate Band Solar Cells. *ACS Photonics* **4**, 2745–2750 (2017).

131. Watanabe, K., Tsukamoto, S., Gotoh, Y. & Koguchi, N. Photoluminescence studies of GaAs quantum dots grown by droplet epitaxy. *J. Cryst. Growth* **227–228**, 1073–1077 (2001).

132. Basso Basset, F. *et al.* Spectral broadening in self-assembled GaAs quantum dots with narrow size distribution. *J. Appl. Phys.* **126**, 024301 (2019).

133. Treu, J. *et al.* Substrate orientation dependent fine structure splitting of symmetric In(Ga)As/GaAs quantum dots. *Appl. Phys. Lett.* **101**, 022102 (2012).

134. Chen, J. X. *et al.* Tuning InAs/GaAs quantum dot properties under Stranski-Krastanov growth mode for 1.3 μm applications. *J. Appl. Phys.* **91**, 6710 (2002).

135. Yamaguchi, H., Fahy, M. R. & Joyce, B. A. Inhibitions of three dimensional island formation in InAs films grown on GaAs(111)A surface by molecular beam epitaxy. *Appl. Phys. Lett.* **69**, 776–778 (1996).

136. Esposito, L., Bietti, S., Fedorov, A., Nötzel, R. & Sanguinetti, S. Ehrlich-Schwöbel effect on the growth dynamics of GaAs(111)A surfaces. *Phys. Rev. Mater.* **1**, 024602 (2017).

137. Ritzmann, J. *et al.* Overcoming Ehrlich-Schwöbel barrier in (111)A GaAs molecular beam epitaxy. *J. Cryst. Growth* **481**, 7–10 (2018).

138. Horikoshi, Y., Uehara, T., Iwai, T. & Yoshiba, I. Area selective growth of GaAs by migration-enhanced epitaxy. *Phys. status solidi* **244**, 2697–2706 (2007).

139. Heyn, C. *et al.* Regimes of GaAs quantum dot self-assembly by droplet epitaxy. *Phys. Rev. B* **76**, 075317 (2007).

140. Tuktamyshev, A., Fedorov, A., Bietti, S., Tsukamoto, S. & Sanguinetti, S. Temperature Activated Dimensionality crossover in the nucleation of quantum dots by droplet epitaxy on GaAs(111)A vicinal substrates. *Sci. Rep.* **9**, 14520 (2019).

141. Ohtake, A., Ha, N. & Mano, T. Extremely high- and low-density of Ga droplets on GaAs{111}A,B: Surface-polarity dependence. *Cryst. Growth Des.* **15**, 485–488 (2015).

142. Tian, B., Xie, P., Kempa, T. J., Bell, D. C. & Lieber, C. M. Single-crystalline kinked semiconductor nanowire superstructures. *Nat. Nanotechnol.* **4**, 824–829 (2009).

143. Lenrick, F., Ek, M., Deppert, K., Samuelson, L. & Reine Wallenberg, L. Straight and kinked InAs nanowire growth observed in situ by transmission electron microscopy. *Nano Res.* **7**, 1188–1194 (2014).

144. Koivusalo, E. S. *et al.* Deterministic switching of the growth direction of self-catalyzed GaAs nanowires. *Nano Lett.* **19**, 82–89 (2019).

145. Ostwald, W. Über die vermeintliche isomerie des roten und gelben quecksilberoxyds und die oberflächenspannung fester Körper. *Zeitschrift für Phys. Chemie* **34U**, 495–503 (1900).

146. Haberern, K. W. & Pashley, M. D. GaAs(111)A-(2×2) reconstruction studied by scanning tunneling microscopy. *Phys. Rev. B* **41**, 3226–3229 (1990).

147. Shapiro, J. N., Lin, A., Huffaker, D. L. & Ratsch, C. Potential energy surface of In and Ga adatoms above the (111)A and (110) surfaces of a GaAs nanopillar. *Phys. Rev. B* **84**, 085322 (2011).

148. Brusaferri, L. *et al.* Thermally activated carrier transfer and luminescence line shape in self-organized InAs quantum dots. *Appl. Phys. Lett.* **69**, 3354–3356 (1996).

149. Kissel, H. *et al.* Size distribution in self-assembled InAs quantum dots on GaAs (001) for intermediate InAs coverage. *Phys. Rev. B* **62**, 7213–7218 (2000).

150. Lee, S., Noh, S., Choe, J. & Kim, E. Evolution of bimodal size-distribution on InAs coverage variation in as-grown InAs/GaAs quantum-dot heterostructures. *J. Cryst. Growth* **267**, 405–411 (2004).

151. Debnath, M. C. *et al.* Optical properties of bimodally distributed InAs quantum dots grown on digital $AlAs_{0.56}Sb_{0.44}$ matrix for use in intermediate band solar cells. *J. Appl. Phys.* **121**, 214304 (2017).

152. Medeiros-Ribeiro, G. Shape Transition of germanium nanocrystals on a silicon (001) surface from pyramids to domes. *Science* **279**, 353–355 (1998).

153. Daruka, I., Tersoff, J. & Barabási, A.-L. Shape transition in growth of strained islands. *Phys. Rev. Lett.* **82**, 2753–2756 (1999).

154. Sanguinetti, S. *et al.* Effects of post-growth annealing on the optical properties of self-assembled GaAs/AlGaAs quantum dots. *J. Cryst. Growth* **242**, 321–331 (2002).

155. Sanguinetti, S. *et al.* Rapid thermal annealing effects on self-assembled quantum dot and quantum ring structures. *J. Appl. Phys.* **104**, 113519 (2008).

156. Kuroda, K. *et al.* Distribution of exciton emission linewidth observed for GaAs quantum dots grown by droplet epitaxy. *J. Lumin.* **130**, 2390–2393 (2010).

157. Herzog, F. *et al.* Optimization of AlAs/AlGaAs quantum well heterostructures on on-axis and misoriented GaAs(111)B. *Appl. Phys. Lett.* **100**, 192106 (2012).

158. Trapp, A. & Reuter, D. Formation of self-assembled GaAs quantum dots via droplet epitaxy on misoriented GaAs(111)B substrates. *J. Vac. Sci. Technol. B* **36**, 02D106 (2018).

159. Kim, J. S. Ga-migration on a Ga-rich and As-stabilized surfaces: Ga-droplet and GaAs-nanostructure formation. *Mater. Sci. Semicond. Process.* **57**, 70–76 (2017).

160. Pimpinelli, A., Jensen, P., Larralde, H. & Peyla, P. Scaling and crossovers in models for thin film growth (World Scientific Publishing Co. Pte. Ltd., 1999).

161. Kim, J. S. *et al.* GaAs quantum dots with a high density on a GaAs (111)A substrate. *Appl. Phys. Lett.* **88**, 241911 (2006).

162. Jo, M., Mano, T., Sakuma, Y. & Sakoda, K. Extremely high-density GaAs quantum dots grown by droplet epitaxy. *Appl. Phys. Lett.* **100**, 212113 (2012).

163. Benlattar, M., Elkoraychy, E., Sbiaai, K., Mazroui, M. & Boughaleb, Y. Ehrlich–Schwöbel barriers and adsorption of Au, Cu and Ag stepped (100) surfaces. *Mod. Phys. Lett. B* **31**, 1750037 (2017).

164. Tsukamoto, S. & Koguchi, N. Magic numbers in Ga clusters on GaAs (001) surface. *J Cryst. Growth* **209**, 258–262 (2000).

165. Skiba-Szymanska, J. *et al.* Universal growth scheme for quantum dots with low fine-structure splitting at various emission wavelengths. *Phys. Rev. Appl.* **8**, 014013 (2017).

166. Ha, N. *et al.* Single photon emission from droplet epitaxial quantum dots in the standard telecom window around a wavelength of 1.55 μm. *Appl. Phys. Express* **13**, 025002 (2020).

167. Semenova, E. S. *et al.* Metamorphic growth for application in long-wavelength (1.3–1.55 μm) lasers and MODFET-type structures on GaAs substrates. *Nanotechnology* **15**, S283–S287 (2004).

168. Semenova, E. S. *et al.* Metamorphic approach to single quantum dot emission at 1.55 μm on GaAs substrate. *J. Appl. Phys.* **103**, 103533 (2008).

169. Zeuner, K. D. *et al.* On-demand generation of entangled photon pairs in the telecom C-band for fiber-based quantum networks. *arXiv:1912.04782* (2019).

170. Tuktamyshev, A. *et al.* Reentrant behavior of the density vs. temperature of indium islands on GaAs(111)A. *Nanomaterials* **10**, 1512 (2020).

171. Lee, J. H., Wang, Z. M. & Salamo, G. J. The control on size and density of InAs QDs by droplet epitaxy. *IEEE Trans. Nanotechnol.* **8**, 431–436 (2009).

172. Oshima, Y., Nangou, T., Hirayama, H. & Takayanagi, K. Face centered cubic indium nano-particles studied by UHV-transmission electron microscopy. *Surf. Sci.* **476**, 107–114 (2001).

173. Smith, J. & Schneider, V. Anisotropic thermal expansion of indium. *J. Less Common Met.* **7**, 17–22 (1964).

174. Balamurugan, B., Kruis, F. E., Shivaprasad, S. M., Dmitrieva, O. & Zähres, H. Size-induced stability and structural transition in monodispersed indium nanoparticles. *Appl. Phys. Lett.* **86**, 083102 (2005).

175. Chen, J. *et al.* Crystallographic phase transition and island height selection in In/Si(111) growth. *Phys. Rev. B* **77**, 233302 (2008).

176. Baraissov, Z., Panciera, F., Travers, L., Harmand, J.-C. & Mirsaidov, U. Growth Dynamics of gallium nanodroplets driven by thermally activated surface diffusion. *J. Phys. Chem. Lett.* **10**, 5082–5089 (2019).

177. Rovaris, F., Bergamaschini, R. & Montalenti, F. Modeling the competition between elastic and plastic relaxation in semiconductor heteroepitaxy: From cyclic growth to flat films. *Phys. Rev. B* **94**, 205304 (2016).

178. Vincent, R. An analysis of the residual strains in epitaxial tin films. *Philos. Mag.* **19**, 1127–1139 (1969).

179. LeGoues, F. K., Reuter, M. C., Tersoff, J., Hammar, M. & Tromp, R. M. Cyclic growth of strain-relaxed islands. *Phys. Rev. Lett.* **73**, 300–303 (1994).

180. Johnson, H. T. & Freund, L. B. Mechanics of coherent and dislocated island morphologies in strained epitaxial material systems. *J. Appl. Phys.* **81**, 6081–6090 (1997).

181. Shchukin, V. A. & Bimberg, D. Spontaneous ordering of nanostructures on crystal surfaces. *Rev. Mod. Phys.* **71**, 1125–1171 (1999).

182. Stoffel, M., Rastelli, A., Tersoff, J., Merdzhanova, T. & Schmidt, O. G. Local equilibrium and global relaxation of strained SiGe/Si(001) layers. *Phys. Rev. B* **74**, 155326 (2006).

183. Chang, W.-H., Chen, W. Y., Hsu, T. M., Yeh, N.-T. & Chyi, J.-I. Hole emission processes in InAs/GaAs self-assembled quantum dots. *Phys. Rev. B* **66**, 195337 (2002).

184. Souaf, M. *et al.* Investigation of the InAs/GaAs quantum dots' size: dependence on the strain reducing layer's position. *Materials.* **8**, 4699–4709 (2015).

185. Hakkarainen, T. V., Schramm, A., Tommila, J. & Guina, M. The effect of InGaAs strain-reducing layer on the optical properties of InAs quantum dot chains grown on patterned GaAs(100). *J. Appl. Phys.* **111**, 014306 (2012).

186. Seravalli, L. *et al.* Quantum dot strain engineering of InAs⁄InGaAs nanostructures. *J. Appl. Phys.* **101**, 024313 (2007).

187. Ha, N. *et al.* Droplet epitaxy growth of telecom InAs quantum dots on metamorphic InAlAs/GaAs(111)A. *Jpn. J. Appl. Phys.* **54**, 04DG07 (2015).

188. Zhan, W. *et al.* Emission at 1.6 μm from InAs quantum dots in metamorphic InGaAs matrix. *Phys. status solidi* **257**, 1900392 (2020).

189. Richardson, C. J. K. & Lee, M. L. Metamorphic epitaxial materials. *MRS Bull.* **41**, 193–198 (2016).

190. Mano, T. *et al.* Growth of metamorphic InGaAs on GaAs(111)A: Counteracting lattice mismatch by inserting a thin InAs interlayer. *Cryst. Growth Des.* **16**, 5412–5417 (2016).

191. Ohtake, A., Ozeki, M. & Nakamura, J. Strain Relaxation in InAs/GaAs(111)A heteroepitaxy. *Phys. Rev. Lett.* **84**, 4665–4668 (2000).

192. Ohtake, A., Mano, T. & Sakuma, Y. Strain relaxation in InAs heteroepitaxy on lattice-mismatched substrates. *Sci. Rep.* **10**, 4606 (2020).

193. Kim, K., Hart, G. L. W. & Zunger, A. Negative band gap bowing in epitaxial InAs/GaAs alloys and predicted band offsets of the strained binaries and alloys on various substrates. *Appl. Phys. Lett.* **80**, 3105–3107 (2002).

194. Shin, H., Yoon, E., Yoo, Y.-H. & Lee, W. Comparison of the strain-modified band gap energies of truncated and untruncated InAs quantum dots in GaAs matrix at varying inter-dot spacings. *J. Phys. Soc. Jpn.* **73**, 3378–3383 (2004).

195. tiberCAD. http://www.tibercad.org/.

196. Matthews, J. W. Defects associated with the accommodation of misfit between crystals. *J Vac. Sci. Technol.* **12**, 126–133 (1975).

197. Bolkhovityanov, Y. B., Pchelyakov, O. P. & Chikichev, S. I. Silicon – germanium epilayers: physical fundamentals of growing strained and fully relaxed heterostructures. *Physics-Uspekhi* **44**, 655–680 (2001).

198. Houghton, D. C., Perovic, D. D., Baribeau, J.-M. & Weatherly, G. C. Misfit strain relaxation in Ge_xSi_{1-x}/Si heterostructures: The structural stability of buried strained layers and strained-layer superlattices. *J. Appl. Phys.* **67**, 1850–1862 (1990).

199. Zhuang, D. & Edgar, J. H. Wet etching of GaN, AlN, and SiC: A review. *Mater. Sci. Eng. R Reports* **48**, 1–46 (2005).

200. Juska, G., Dimastrodonato, V., Mereni, L. O., Gocalinska, A. & Pelucchi, E. Towards quantum-dot arrays of entangled photon emitters. *Nat. Photonics* **7**, 527–531 (2013).

201. Cambridge Research Laboratory of Toshiba Europe Limited. https://www.toshiba.eu/pages/eu/Cambridge-Research-Laboratory/.

202. Nick Vamivakas, A., Zhao, Y., Lu, C. & Atatüre, M. Spin-resolved quantum-dot resonance fluorescence. *Nat. Phys.* **5**, 198–202 (2009).

203. Chen, Y., Zopf, M., Keil, R., Ding, F. & Schmidt, O. G. Highly-efficient extraction of entangled photons from quantum dots using a broadband optical antenna. *Nat. Commun.* **9**, 2994 (2018).

204. Bester, G. Electronic excitations in nanostructures: an empirical pseudopotential based approach. *J. Phys. Condens. Matter* **21**, 023202 (2009).

List of publications

[1] Francesco Basso Basset, Sergio Bietti, **Artur Tuktamyshev**, Stefano Vichi, Emiliano Bonera, and Stefano Sanguinetti. Spectral broadening in self-assembled GaAs quantum dots with narrow size distribution. *Journal of Applied Physics* **126**, 024301 (2019).

[2] **Artur Tuktamyshev**, Alexey Fedorov, Sergio Bietti, Shiro Tsukamoto, and Stefano Sanguinetti. Temperature activated dimensionality crossover in the nucleation of quantum dots by droplet epitaxy on GaAs(111)A vicinal substrates. *Scientific Reports* **9**, 14520 (2019).

[3] Sergio Bietti, Francesco Basso Basset, **Artur Tuktamyshev**, Emiliano Bonera, Alexey Fedorov, and Stefano Sanguinetti. High-temperature droplet epitaxy of symmetric GaAs/AlGaAs quantum dots. *Scientific Reports* **10**, 6532 (2020).

[4] **Artur Tuktamyshev**, Alexey Fedorov, Sergio Bietti, Shiro Tsukamoto, Roberto Bergamaschini, Francesco Montalenti, and Stefano Sanguinetti. Reentrant behavior of the density vs. temperature of indium islands on GaAs(111)A. *Nanomaterials* **10**, 1512 (2020).

Acknowledgements

For the acknowledgments I would like to use Russian language in which great authors Fyodor Mikhailovich Dostoevsky, Lev Nikolayevich Tolstoy, and many others wrote their novels, because only with the help of my mother tongue I can express my feelings and a gratitude. All the names are presented in the original language and in Russian, so forgive me in advance, if I misspelled your name or it seems bizarre to you in the Cyrillic script.

Данная диссертация завершает трехлетний PhD проект, который я начал не просто в новой для себя лаборатории и исследовательской группе, а также вдали от своего дома, родных и друзей, в другой стране, культуре и обществе. На протяжении всей моей работы я получил безграничный опыт, огромную поддержку и помощь.

В первую очередь я хотел бы поблагодарить своего научного руководителя профессора Стефано Сангуинетти (Stefano Sanguinetti) за то, что дал возможность присоединиться к замечательной группе ученых и поделился своим бесценным опытом в формулировании вопросов и методологии. Спасибо за поддержку и поощрение свободы исследования!

Далее хочу поблагодарить Алексея Федорова (неожиданно имя на русском совпадает с оригиналом) и Серджио Биетти (Sergio Bietti), двух блестящих экспертов технологии молекулярно-лучевой эпитаксии, с которыми я провел большую часть времени, вырастив сотни образцов и обсуждая не только научные вопросы. Спасибо за Ваши знания и опыт, которые я перенял с большим удовольствием!

Конечно же необходимо отменить еще одного человека, профессора Широ Цукамото (ツカモト シロウ, надеюсь я нашел верное написание). Спасибо за Ваши интересные семинары, которые очень помогли при структурировании и написании данной диссертации, а также за разговоры о жизни, семье и будущем! Надеюсь, что в скором времени я снова смогу посетить замечательную страну Японию и отведать вкуснейшие суши.

Большую часть времени я провел в исследовательском центре L-NESS, который расположен в изумительном городке Комо на берегу одноименного озера. Хотелось бы поблагодарить всех людей, окружавших меня здесь, за создание и поддержание дружественной обстановки, за добрые и веселые разговоры в обеденной комнате, а также во время лабораторных и Рождественских ужинов!

Особенно хочу поблагодарить моего верного друга и товарища Демостениса Толиопоулоса (Δημοσθένης Τολιόπουλος). Спасибо тебе за прекрасное время, которое мы провели не только совместно проживая, но и разделяя хлеб да соль, и напитки (в основном алкогольные). И, конечно же, огромное спасибо за приглашение в твой дом в Афинах. Это было незабываемое путешествие!

Хотелось бы упомянуть всех студентов из нашего проекта “4-Photon”. Демостенис (Δημοσθένης), Йонахан (Jonathan), Андреа (Andrea), Леонардо (Leonardo), Джоффри (Geoffrey), Раджа (राजा), Адонай (Adonai), Панайот (кажется по-болгарски будет также), Шиванги (शिवांगी), Йоргос (Γιώργος), Льянг (梁), Пётр (Piotr), Антонио (Antonio) и Мэрьем (مريم), спасибо Вам за те памятные часы, которые мы провели во время наших совместных занятий. В моей памяти надолго отложатся наши посиделки в барах и разговоры о науке. Огромное спасибо всем людям, принимавших участие в этом проекте за ту невероятную работу, которую мы проделали все вместе. Отдельные слова благодарности для Сандрин Соубс (Sandrine Soubes) за ее энергетику и новые идеи, с которыми она с радостью делилась, а также для Антонеллы Сгамбато (Antonella Sgambato) и Анны Пизано (Anna Pisano) за то, что сделали учебу и работу намного проще.

Огромное спасибо всем людям из Миланского университета (University of Milano-Bicocca) с кем я знаком. Особенно выделю Стефано Вики (Stefano Vichi) за квантовые расчеты выращенных структур и помощь в дебрях университетской бюрократии.

Слова благодарности хочется выразить исследовательской группе в области нанофотоники из Королевского технологического института (KTH) в Стокгольме под руководством профессора Вала Звиллера (Val Zwiller) за то, что приютили меня в своей лаборатории. В особенности спасибо Катарине (Katharina Zeuner) за экскурс в мир передовой фотолюминесцентной спектроскопии и за проявленное терпение при ответах на сотни моих глупых вопросов.

Хочется поблагодарить всех моих друзей и родных, которые все это время оказывали мне огромную поддержку. Быть вдалеке от Вас оказалось очень сложной задачей, и я очень рад, что некоторым из Вас удалось посетить меня и насладиться итальянской едой и вином.

И в конце, хочу сказать огромное спасибо моей любимой Камиллочке за ее любовь, заботу и поддержку. Без тебя и твоей веры в меня это захватывающее путешествие никогда бы не состоялось. Спасибо, что делаешь меня счастливым, и я надеюсь отплатить тебе тем же!